EXPERIMENTAL DETERMINATION OF THE RELATIVISTIC FINE-STRUCTURE SPLITTING IN A PIONIC ATOM
and
DEPENDENCE OF K X-RAY ENERGY UPON THE MODE OF EXCITATION

Thesis by
Keh-Chung Wang

In Partial Fulfillment of the Requirements

for the Degree of

Doctor of Philosophy

California Institute of Technology

Pasadena, California

1979

(Submitted April 20, 1979)

ACKNOWLEDGMENTS

I would like to thank Professor Felix Boehm for his essential contributions to this work and his guidance and encouragement throughout my graduate study at Caltech.

Let me express my deep gratitude to Drs. Richard Powers and Petr Vogel for invaluable advice and enlightening discussions, and to Dr. Alan Hahn for his many contributions to these experiments. I am indebted to Mr. Herbert Henrikson for designing, constructing, and installing the Caltech-LAMPF spectrometer which was indispensable for this research. The collaboration with Drs. Eric Bovet, Paul Lee, James Miller, and Jean-Luc Vuilleumier was fruitful and greatly appreciated. Special thanks go to Mrs. Elsa Garcia who skillfully typed this thesis. I would also like to thank Mr. Ed Redden for his technical assistance. Working in the Physics 34 group has been a pleasant and rewarding experience.

Professor Valentine Telegdi's inspiring and clarifying comments on the relativistic equations are gratefully acknowledged.

Professor Ray Kunselman and Mr. Mark Manley participated in the first experiment reported in this thesis and offered great help. The cooperation of Dr. Louis Rosen and his staff at Los Alamos Meson Physics Facility is also deeply appreciated.

The financial support provided by the California Institute of Technology and the U.S. Department of Energy is gratefully acknowledged.

Finally, I would like to thank my wife Jenn-hwang for her continuing help and encouragement.

ABSTRACT

Part I. Using a high-resolution crystal spectrometer we have measured the energy splitting of the pionic 5g-4f and 5f-4d transitions in Ti. The observed fine structure splitting of 85.2 ± 3.0 eV agrees with the calculated splitting of 88.1 eV, arising from the relativistic fine-structure correction term of the Klein-Gordon equation or the Relativistic Schrödinger equation and from small corrections due to vacuum polarization, strong interaction, and electron screening.

Part II. We have observed that the energies of K x rays in Ta, Eu, Lu, and W depend on the method of excitation of the atoms. For example, the energy of the Ta $K\alpha_1$ x ray emitted after electron capture of ^{181}W has been found to be lower by 0.78 ± 0.04 eV compared to the fluorescent Ta $K\alpha_1$ x ray. Similarly, we have observed that the Ta $K\alpha_1$ x ray emitted after internal conversion following β-decay of ^{181}Hf is higher by 0.7 ± 0.1 eV in energy compared to the same fluorescent Ta x ray. The observed shift in Ta cannot be explained by such known mechanisms as the chemical, magnetic hyperfine, isotope, isomer, and shake-off effects alone. However, these mechanisms seem to explain most of the observed shift in Eu, Lu, and W.

To my father

TABLE OF CONTENTS

PART I

EXPERIMENTAL DETERMINATION OF THE RELATIVISTIC FINE-STRUCTURE SPLITTING IN A PIONIC ATOM

PART II

DEPENDENCE OF K X-RAY ENERGY UPON THE MODE OF EXCITATION

PART I

EXPERIMENTAL DETERMINATION OF THE RELATIVISTIC FINE-STRUCTURE SPLITTING IN A PIONIC ATOM

CHAPTER 1

INTRODUCTION

The motivation of this work is to provide a test of the equation of motion for a spinless particle in a Coulomb field. For spin $\frac{1}{2}$ fermions tests of the Dirac equation were implemented to great accuracy. For example, the latest measurement of the electron g-factor anomaly agrees with the QED calculations to better than one part per million.(1) No such tests have been done for spin 0 bosons.

More specifically one would ask: Do the relativistic equations such as the Relativistic Schrödinger equation(2) and the Klein-Gordon equation(3) correctly describe spinless particles? It is well known(3,4) that for a charged spinless particle in a Coulomb field these two equations predict a removal of the degeneracy between states of different angular momenta ℓ, belonging to the same principal quantum number n. To leading order, i.e. $(\frac{Z\alpha}{n})^4$, both the Relativistic Schrödinger equation and the Klein-Gordon equation predict identical relativistic "fine-structure" corrections (Sec. 2.1), given by

$$\delta E = -mc^2 \left[\frac{1}{2}\left(\frac{Z\alpha}{n}\right)^4 \left(\frac{n}{\ell+\frac{1}{2}} - \frac{3}{4}\right)\right]. \tag{1.1}$$

An example of the splitting of levels is shown in Fig. 1. The predictions of the two equations differ in the terms of order $(\frac{Z\alpha}{n})^6$ and higher.

It is the purpose of this thesis to report on a precision measurement of the fine structure splitting to order $(\frac{Z\alpha}{n})^4$, and discuss

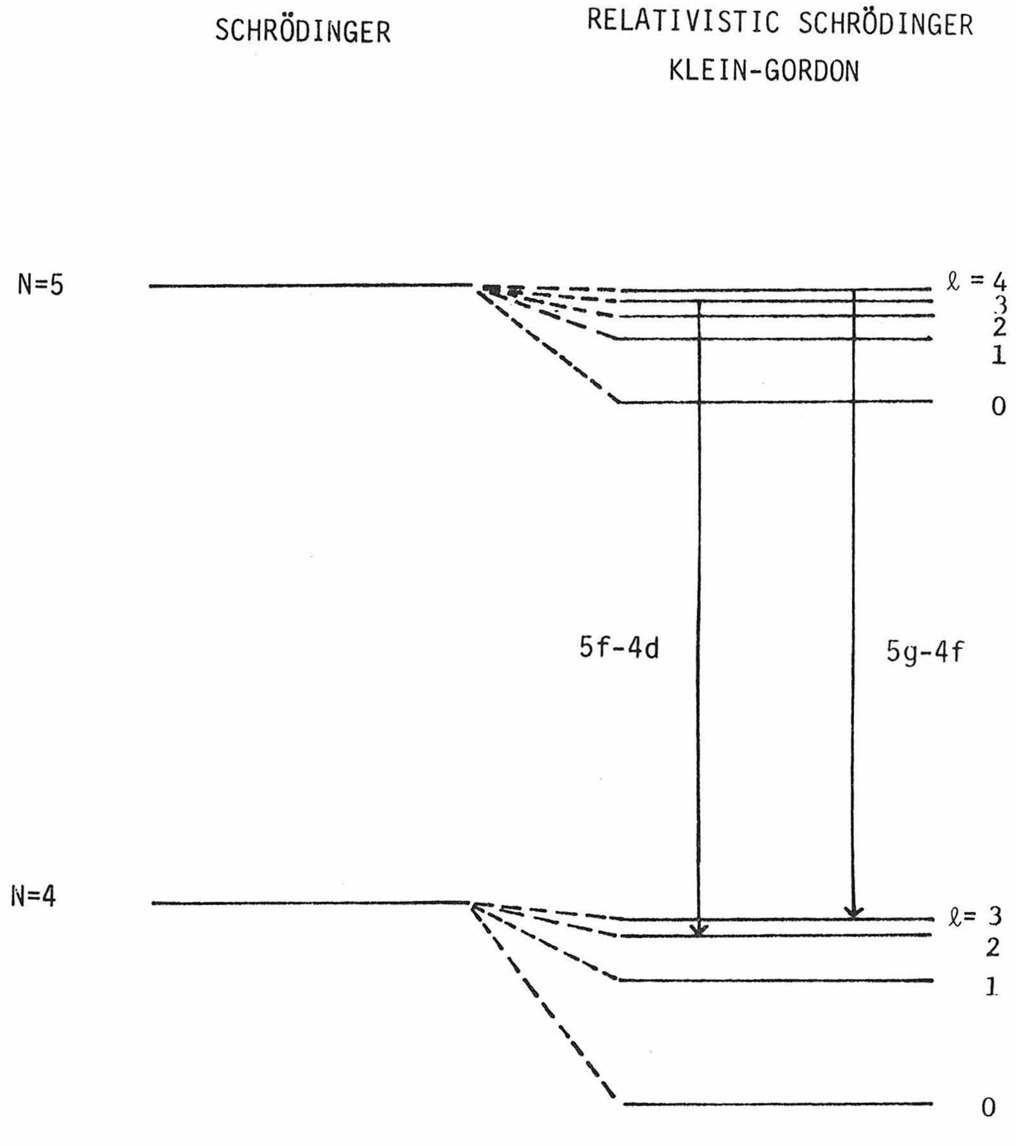

FIG. 1. An example of the relativistic fine-structure splitting of n=4 and 5 levels for a spinless particle in a Coulomb field.

the feasibility of further measurements of the splitting to order $(\frac{Z\alpha}{n})^6$ in order to answer the above question.

In this chapter we discuss the general aspects of the measurement of the fine-structure splitting. Theoretical considerations are given in Chapter 2. The experimental methods are described in detail in Chapter 3. We draw a conclusion of our experiment and discuss further measurements in Chapter 4.

1.1 Pionic Atom and the Measurement of the Relativistic Fine-Structure Splitting

One of the few systems that have a spinless boson in a Coulomb field is the pionic atom, consisting of a π^- and a nucleus. It is produced by stopping a π^- beam in matter. After the capture of a π^- by an atom, the π^- cascades toward the nucleus and pionic x rays are emitted. Since the mass of a pion is about 273 times larger than that of an electron, the pion is much closer to the nucleus in a pionic atom than the electron in a hydrogen-like atom (for the same quantum numbers). As a consequence, vacuum polarization plays an important role in a pionic atom. Fortunately, the vacuum polarization effect can be calculated very accurately. The strong interaction between the pion and the nucleus shifts and broadens the energy levels. This correction can be calculated to about 10% accuracy. Pionic atoms (except pionic H atom) are always surrounded by electrons. The screening effect of the electrons should also be taken into consideration in calculating the energy levels of the pionic atom. Details of the above effects are discussed in Chapter 2.

Complete discussions of pionic atoms can be found in review articles.(5,6)

One way to test the correction (1.1) is to measure precisely the energy splitting, which we called the relativistic fine-structure splitting, of pionic x rays emitted during the transition of the π^- between two energy levels with different principal quantum numbers. No such measurement has been reported until recently. In a recent experiment designed to measure the mass of the π^- by measuring the pionic x-ray energy, Carter *et al.*(7) have observed the fine-structure splitting for the 6-5 and 7-6 transitions in Au, Tl, and Pb. The 6-5 transitions have large strong interaction corrections and are not well suited for precise evaluations of the splitting. The 7-6 transitions, on the other hand, have negligible strong interactions. The 7i-6h and 7h-6g peaks, however, are not fully resolved by the Ge detector used in the experiment. The aim of our experiment was to determine the energy splitting to an accuracy of 1% for transitions where the corrections of the strong interaction effect and the electron screening effect are small, using a high resolution bent-crystal spectrometer.(8)

For the present experiment we have chosen the 5g - 4f and 5f - 4d transitions in π^- - Ti ($Z = 22$). These transitions are particularly suited to our crystal spectrometer technique, and the various corrections to be applied to the observed transition energies are well understood, as will be explained in the following chapter.

CHAPTER 2

THEORETICAL CONSIDERATIONS

In this chapter we discuss the various contributions to the binding energy of a pion in its orbits. The principal contribution to the binding energy comes from the point Coulomb interaction. Smaller contributions arise from vacuum polarization, strong interaction, electron screening, and nuclear finite size. Numerical calculations of the energy levels in a pionic atom are also discussed. The calculated splitting of the π^--Ti 5-4 transitions is presented in Sec. 2.5. The reasons to choose these particular transitions are given in Sec. 2.6.

2.1 Coulomb Interaction

The unscreened Coulomb potential is given by

$$V_C = e\phi = -\frac{Z\alpha}{r} . \tag{2.1}$$

According to the (non-relativistic) Schrödinger equation

$$i\frac{\partial}{\partial t}\psi = (-\frac{\vec{\nabla}^2}{2m} + e\phi)\psi \tag{2.2}$$

(in units of $c = \hbar = 1$) the energy eigenvalues are(9)

$$E_{n\ell} = -\frac{m}{2}(\frac{Z\alpha}{n})^2 . \tag{2.3}$$

The eigenstates with the same n but different ℓ's are degenerate. Since the velocity of the π^- at low n levels in a pionic atom is not negligible compared to the velocity of light, e.g. $v_\pi \cong 0.04c$ at n=4 for Z=22, a relativistic generalization of Eq. (2.2) is needed.[†]

One procedure as discussed in Goldberger and Watson(2) is to replace the kinetic energy operator in Eq. (2.2) by its relativistic generalization $\sqrt{-\vec{\nabla}^2 + m^2}$. One obtains the Relativistic Schrödinger equation

$$i \frac{\partial}{\partial t} \psi = \left(\sqrt{-\vec{\nabla}^2 + m^2} + e\phi\right) \psi. \tag{2.4}$$

Expanding the square root in Eq. (2.4)

$$m\left(1 - \frac{\vec{\nabla}^2}{2m^2} + \frac{\vec{\nabla}^4}{8m^4} - \dots\right)$$

and treating the terms of order $\left(\frac{\vec{\nabla}}{m}\right)^4$ or higher as a perturbation, one obtains(4) for the energy levels to order $\left(\frac{Z\alpha}{n}\right)^4$

$$E_{n\ell} = m - \frac{m}{2}\left(\frac{Z\alpha}{n}\right)^2 \left[1 + \left(\frac{Z\alpha}{n}\right)^2 \left(\frac{n}{\ell + \frac{1}{2}} - \frac{3}{4}\right)\right]. \tag{2.5}$$

Another relativistic generalization of Eq. (2.2) is the well known Klein-Gordon equation(3)

$$\left(i \frac{\partial}{\partial t} - e\phi\right)^2 \psi = \left(-\vec{\nabla}^2 + m^2\right) \psi . \tag{2.6}$$

[†] In general, this is true for any atom.

It predicts(3) for the energy levels

$$E_{n\ell} = \frac{m}{\sqrt{1+\lambda_{n\ell}}} , \qquad (2.7)$$

with

$$\lambda_{n\ell} = \left(\frac{Z\alpha}{n - \ell - \frac{1}{2} + \sqrt{(\ell + \frac{1}{2})^2 - (Z\alpha)^2}} \right)^2 .$$

The expansion of Eq. (2.7) to order $(\frac{Z\alpha}{n})^4$ gives

$$E_{n\ell} = m - \frac{m}{2} (\frac{Z\alpha}{n})^2 \left[1 + (\frac{Z\alpha}{n})^2 (\frac{n}{\ell + \frac{1}{2}} - \frac{3}{4}) \right] . \qquad (2.8)$$

Eqs. (2.5) and (2.8) are identical.

The difference of solutions of Eqs. (2.4) and (2.6) to order $(\frac{Z\alpha}{n})^6$ will be discussed in Sec. 4.3 and Appendix C.

2.2 Vacuum Polarization

The electronic vacuum polarization effect arises from the emission and reabsorption of virtual electron-position pairs. The Feynman diagrams that illustrate the lowest order corrections of this effect are shown in Fig. 2. The range of this effect is approximately equal to the Compton wavelength of the electron $\lambda\!\!\!^{-}_e = \frac{1}{m_e}$ = 386 fm. At the n = 4 and 5 states in a pionic Ti atom, the distance between the pion and the nucleus is smaller than $\lambda\!\!\!^{-}_e$. Therefore, vacuum polarization

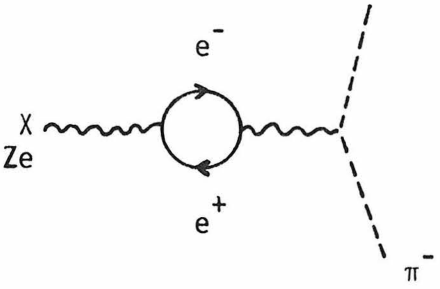

(a) Of order $\alpha Z\alpha$.

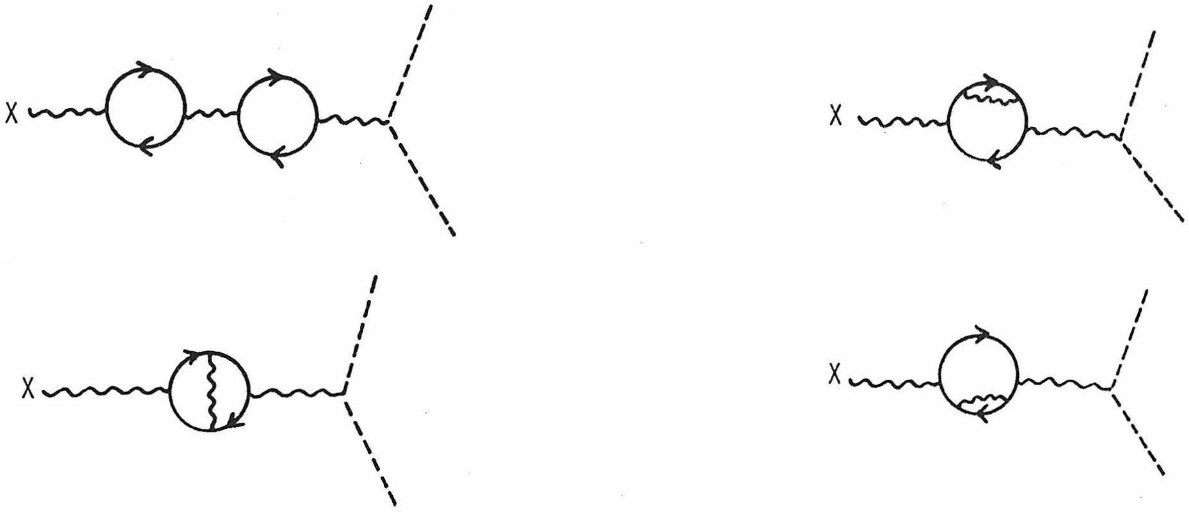

(b) Of order $\alpha^2(Z\alpha)$.

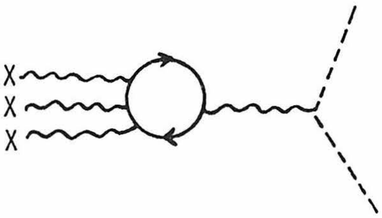

(c) Of order $\alpha(Z\alpha)^3$.

FIG. 2. Feynman diagrams of the lowest order corrections of vacuum polarization.

affects the energies of these states.

To order $\alpha Z\alpha$ (Fig. 2(a)) and for a spherically symmetric nuclear charge distribution $\rho(r)$ the vacuum polarization potential V_{VP} can be written as$^{(10)}$

$$V_{VP}(r) = \frac{2\alpha^2}{3r} \bar{\lambda}_e \int_0^\infty r' \rho(r') \left[\chi\left(\frac{r+r'}{\bar{\lambda}_e}\right) - \chi\left(\frac{|r-r'|}{\bar{\lambda}_e}\right)\right] dr', \qquad (2.9)$$

with

$$\chi(\xi) = \int_1^\infty \frac{1}{z^2}\left(1+\frac{1}{2z^2}\right)\left(1-\frac{1}{z^2}\right)^{\frac{1}{2}} \exp(-2\xi z)\,dz.$$

McKee$^{(11)}$ has expanded $\chi(\xi)$ into a series, with the results

$$\chi(\xi) = \sum_{k=0}^{\infty} \left[a_k (2\xi)^k \exp(-2\xi) + b_k (2\xi)^{2k+1} E_i(2\xi)\right], \qquad (2.10)$$

where $E_i(2\xi)$ is the exponential integral

$$\int_1^\infty \frac{\exp(-2\xi z)}{z}\,dz,$$

and found that cutting off the expansion at a_4 and b_2 introduced an error no larger than about 0.01%. The remaining coefficients are:

$a_0 = 0.88358$

$a_1 = 0.02376$

$a_2 = -0.00708$

$a_3 = 0.00331$

$a_4 = -0.00318$

$b_0 = -1$

$b_1 = 0$

$b_2 = 1/320$

We followed the work of McKee to calculate $V_{VP}(r)$ numerically in order to calculate the corrected energy levels.

Vogel$^{(12)}$ has evaluated numerically the higher-order vacuum polarization potentials, $\alpha^2(Z\alpha)$ (Fig. 2(b)) and $\alpha(Z\alpha)^3$ (Fig. 2(c)). The corrections due to these potentials are small. So we treated them as a perturbation in our calculation.

2.3 Strong Interaction

The strong interaction between a π^- and the nucleons affects the energy levels of a pionic atom. Two parts play a role. (1) The elastic scattering

$$\pi^- + N \rightarrow \pi^- + N \tag{2.11}$$

shifts the energy levels. (2) The absorption

$$\pi^- + N + N \rightarrow N + N \tag{2.12}$$

broadens the energy levels. Owing to the conservation of energy and momentum, the absorption of a π^- by one nucleon N in a nucleus, i.e.

$$\pi^- + N \rightarrow N, \tag{2.13}$$

is not possible.

The strong interaction potential V_{SI} between a π^- and the nucleus in a pionic atom can be derived from the two basic mechanisms (2.11) and (2.12). Under the assumptions that (1) the incident π^- wave undergoes multiple scattering with the nucleons, (2) the interaction between the π^- and nucleons is of very short range ($\delta(\vec{r}_\pi - \vec{r}_N)$ type), and (3) the correlations of two nucleons have zero range, Ericson and Ericson(13) have shown that the wavefunction ψ of the pion obeys the equation

$$(\vec{\nabla}^2 + k^2)\,\psi = V_{SI}\,\psi, \tag{2.14}$$

with $k^2 = (E - V)^2 - m^2$. V is the potential describing the electromagnetic interaction and V_{SI} describes the strong interaction as

$$V_{SI} = \frac{1}{2\mu}\left(V_L(\vec{r}) - \vec{\nabla}\cdot\frac{\alpha_0(\vec{r})}{1 - \frac{1}{3}\alpha_0(\vec{r})}\vec{\nabla}\right),$$

where $V_L(\vec{r})$ and $\alpha_0(\vec{r})$ are functions of the nucleon densities and the π-N scattering amplitudes, and μ is the reduced mass of the pion-nucleus system. The potential V_{SI} has a local term V_L, as well as a velocity dependent term.

Practically, in order to calculate the effect of V_{SI} on the energy levels in a pionic atom, an additional parameter ξ was introduced to take into account the finite range of the nucleon-nucleon correlations(14) so that

$$V_{SI} = \frac{1}{2\mu}\left(V_L(\vec{r}) + \vec{\nabla}\cdot\zeta(\vec{r})\vec{\nabla}\right), \tag{2.15}$$

where

$$\zeta(\vec{r}) = \frac{\alpha_0(\vec{r})}{1 - \frac{\xi}{3}\alpha_0(\vec{r})} ,$$

and V_L and α_0 can be expressed as$^{(15)}$

$$V_L = -4\pi\Big[b_0(\rho_n + \rho_p)\, t_1 + b_1(\rho_n - \rho_p)\, t_1 + i B_0 \rho_p (\rho_n + \rho_p)\, t_2 + i B_1 \rho_p (\rho_n - \rho_p)\, t_2\Big] \qquad (2.16)$$

$$\alpha_0 = -4\pi\Big[c_0(\rho_n + \rho_p)\, t_1 + c_1(\rho_n - \rho_p)\, t_1 + i C_0 \rho_p (\rho_n + \rho_p) t_2 + i C_1 \rho_p (\rho_n - \rho_p) t_2\Big] .$$

Here $t_1 = (1 + \frac{m_\pi}{m_N})$, $t_2 = (1 + \frac{m_\pi}{2m_N})$, ρ_n and ρ_p are densities of neutrons and protons, and the quantities b_0, b_1, B_0, B_1, c_0, c_1, C_0, C_1 and ξ are empirical parameters that can be determined from the measured level shifts and broadenings due to the strong interaction effect.

For pionic atoms of atomic numbers $Z = 6$ to 22, the above parameters have been determined, by a least-squares fit to the existing data, to be:$^{(16)}$

$b_0 = -0.02845(56)\ m_\pi^{-1}$ $\qquad c_0 = 0.255(52)\ m_\pi^{-3}$

$b_1 = -0.0672(76)\ m_\pi^{-1}$ $\qquad c_1 = 0.081(67)\ m_\pi^{-3}$

$B_0 = 0.0899(45)\ m_\pi^{-4}$ $\qquad C_0 = 0.34(22)\ m_\pi^{-6}$

$B_1 = 0.56(18)\ m_\pi^{-4}$ $\qquad C_1 = -2.6(1.4)\ m_\pi^{-6}$

$\xi = 1.99(74)$

The numerical method to solve Eq. (2.14) with the potential (2.15) will be discussed in Sec. 2.5.

2.4 Electron Screening

A pionic atom is formed when a π^- is captured in the Coulomb field of an atom. Most of the atomic electrons originally associated with the atom are still around the nucleus. Some of them, especially the ns electrons, have a non-negligible probability of being inside the π^- orbit and thus screen the Coulomb field, changing the energy levels of the pionic atom. It has been shown(17,18) that, in a pionic atom of atomic number Z, when the π^- orbit is inside the electronic K-shell the electron density is practically equal to the electron density of a normal atom of atomic number Z-1, since the π^- screens one unit of charge from the nucleus.

For a spherically symmetric electron density $\rho_e(r)$, the electron screening potential in a pionic atom is

$$\begin{aligned} V_{ES}(r) &= \frac{4\pi\alpha}{r} \int_0^r \rho_e(t) t^2 \, dt + 4\pi\alpha \int_r^\infty \rho_e(t)\, t \, dt \\ &= 4\pi\alpha \int_0^\infty \rho_e(t) t \, dt - 4\pi\alpha \int_0^r \rho_e(t)\, (t - \frac{t^2}{r}) dt \\ &\equiv V_0 - V_1(r) \, . \end{aligned} \tag{2.17}$$

V_0 is the electron potential at the origin and does not contribute to the screening correction. Vogel(12) has evaluated V_{ES} numerically to about 3% accuracy, using the relativistic Hartree-Fock-Slater method for the $\rho_e(r)$ calculation. We followed his results, assuming that the pionic atom is not ionized, in particular, that both K-electrons are present, to evaluate the screening corrections in the pionic Ti 5-4 transitions.

While the π^- cascades down toward the inner levels, Auger electrons may be ejected so that the electron shells around a pionic atom may be partially ionized. Since $\frac{m_e}{m_{\pi^-}} < (\frac{1}{7^2} - \frac{1}{8^2})$, it turns out that the energies of pionic 8-7 transitions in an atom (given by Eq. (2.3)) are higher than the electronic K-absorption edge of that atom. The K-electrons which contribute most to the electron screening may thus be ejected during the 8-7 transitions or the following transitions. The validity of the assumption of two K-electron screening in our calculation depends on the refilling rate of the K-holes. It does not affect the result of this experiment, since the screening correction to the total splitting of the π^--Ti 5-4 transitions is only -1.4 eV which is smaller than the experimental error of 3.0 eV. Other experiments, e.g. the measurement of π^- mass to 5 ppm(19) or the experiment we discuss in Sec. 4.3, essentially depend on the refilling rate. An experimental study of this refilling rate by measuring the electron screening corrections of pionic transitions in several pionic atoms has been proposed.(20)

2.5 Numerical Calculation

Numerically the Klein-Gordon equation was solved with the potentials V_C, V_{VP} and V_{SI} as given in (2.1), (2.9) and (2.15). The electron screening potential V_{ES} in (2.17) was treated as a perturbation term. This means that we solved the Eq. (2.14) with $V = V_C + V_{VP}$, and calculated the contribution of electron screening as

$$\Delta E_{ES} = < \psi | V_{ES} | \psi > . \tag{2.18}$$

Let $E = m + \varepsilon$ and consider the finite mass of nuclei, Eq. (2.14) becomes$^{(15)}$

$$\frac{\vec{\nabla}^2}{2\mu}\psi + \left[\varepsilon - V_{SI} + \frac{(\varepsilon - V_C - V_{VP})^2}{2\,m}\right] \psi = 0 . \tag{2.19}$$

It is useful to rewrite Eq. (2.19) in the following form:

$$\frac{1}{2\,\mu}\vec{\nabla}\cdot(1+\zeta)\,\vec{\nabla}\psi + \left\{(\varepsilon - V_C - V_{VP})\left[1 + \frac{(\varepsilon - V_C - V_{VP})}{2m}\right] - V_L\right\}\psi = 0 . \tag{2.20}$$

Let $f \equiv r\,\psi$ and

$$g \equiv (1+\zeta)\,\left(\frac{df}{dr} - \frac{f}{r}\right), \tag{2.21}$$

then we have

$$\frac{dg}{dr} = -\frac{g}{r} + (1+\zeta)\,\frac{\ell(\ell+1)f}{r^2} - (\varepsilon - V_C - V_{VP} - V_L)2\mu f - \frac{(\varepsilon - V_C - V_{VP})^2}{m}\,\mu f . \tag{2.22}$$

Then the coupled first order Eqs. (2.21), (2.22) are solved numerically, with the normalization condition

$$\int \psi^2 r^2 \, dr = \int f^2 \, dr = 1. \tag{2.23}$$

By turning off the V_{VP} and V_{SI} individually, we can get the correction to the energy levels due to each of them. The effect of nuclear motion beyond the reduced mass correction, pointed out by Seki(21), was calculated and turned out to be negligible in the pionic Ti 5-4 transitions. So does the effect of finite size nuclear charge distribution, since in the states we consider the overlap of the π^- orbit and the nucleus is almost zero.

The calculated fine-structure splitting of the pionic 5-4 transitions, and the corrections due to the effects discussed above are shown in Table 1.

2.6 Choice of the Pionic Transitions for this Experiment

The pionic transitions for this experiment were chosen by considering the information contained in Figs. 3-5. In Fig. 3 the (non-relativistic) transition energy to order $(\frac{Z\alpha}{n})^2$ as a function of the atomic number Z is plotted. Fig. 4 shows the energy splitting, due to a point Coulomb interaction to order $(\frac{Z\alpha}{n})^4$, of the circular transitions, $(n_i, \ell_i = n_i - 1) \rightarrow (n_f, \ell_f = n_f - 1)$, and the noncircular transitions, $(n_i, \ell'_i = n_i - 2) \rightarrow (n_f, \ell'_f = n_f - 2)$, between two consecutive principal quantum numbers n_i and n_f as a function of Z, as predicted by

TABLE 1. Calculated fine structure splitting of the pionic Ti 5-4 transitions (in eV).

	5g-4f	5f-4d	Difference
Point Coulomb Interaction	40386.9	40446.1	59.2
Vac. Pol. $\alpha Z\alpha$ (exact)	82.7	108.8	26.1
Higher Order Vac. Pol.	0.7	1.0	0.3
Strong Interactions[a]	0.0	3.9	3.9
Electron Screening[b]	-4.4	-5.8	-1.4
Total	40465.9	40554.0	88.1

[a] The uncertainty is about 10%.

[b] A maximum value is given corresponding to the presence of two 1s electrons.

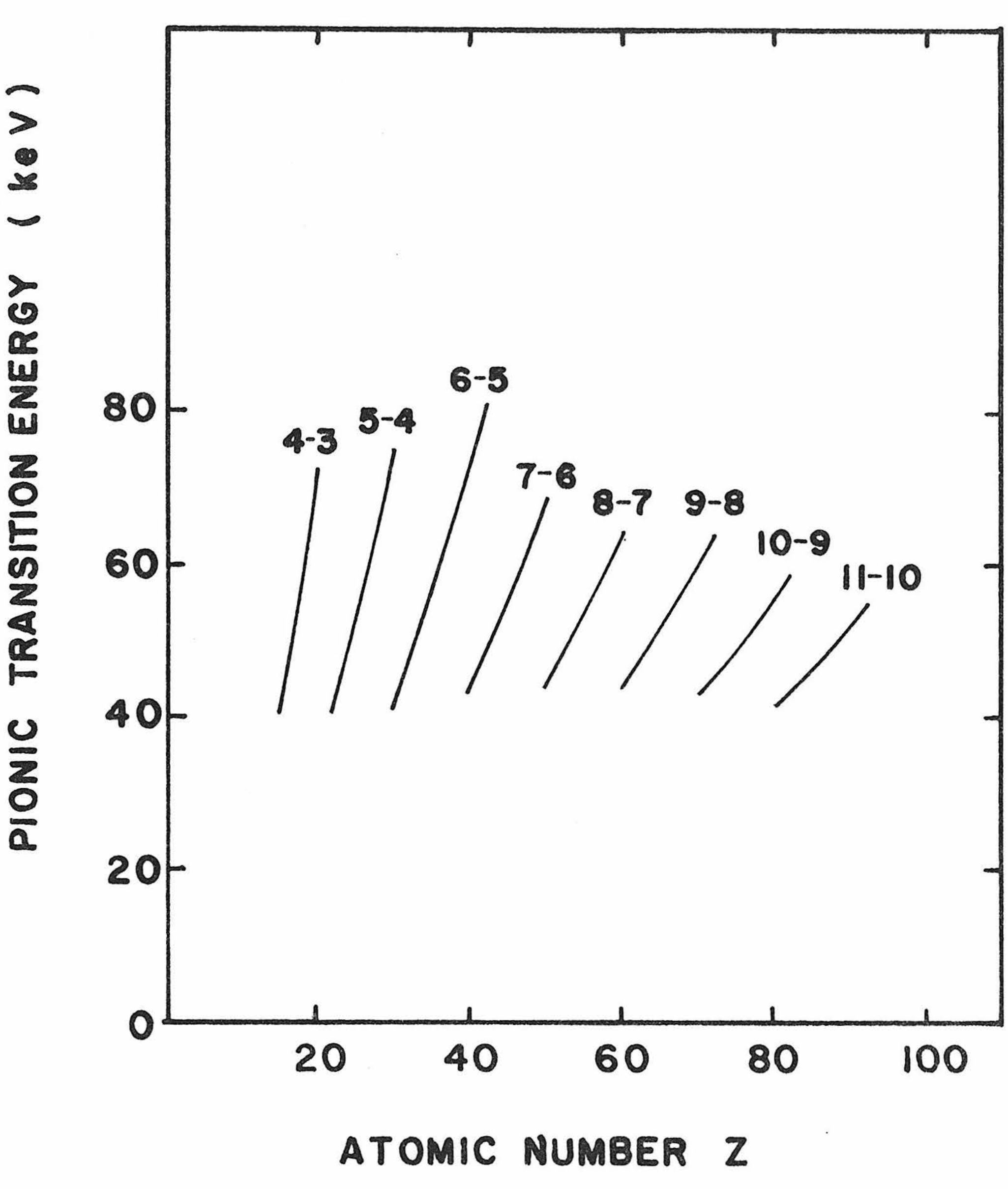

FIG. 3. Pionic transition (n_i-n_f) energy as a function of atomic number Z.

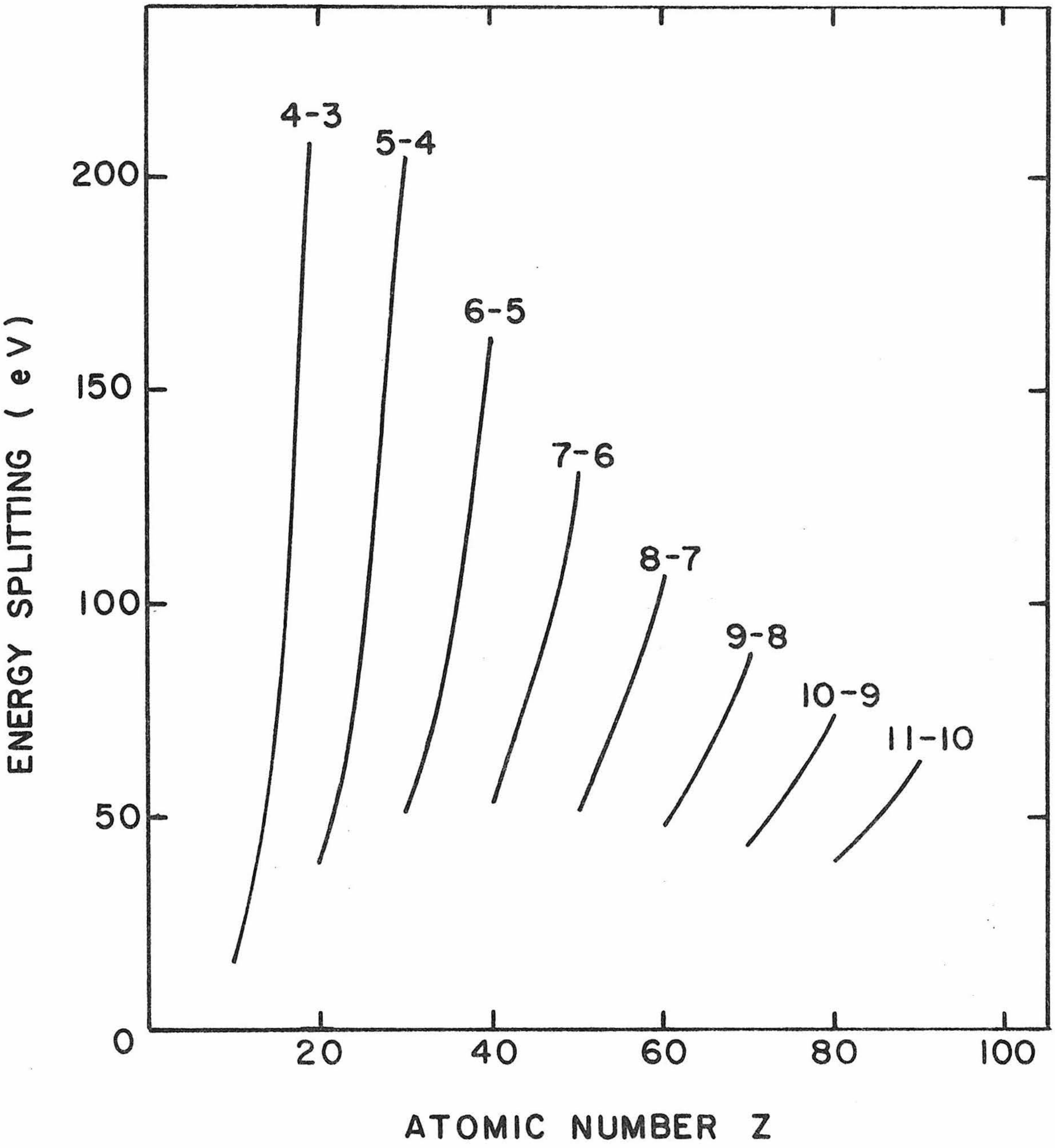

FIG. 4. Energy splitting of transitions $(n_i, \ell_i = n_i - 1) \rightarrow (n_f, \ell_f = n_f - 1)$ and $(n_i, \ell_i' = n_i - 2) \rightarrow (n_f, \ell_f' = n_f - 2)$ between two consecutive n's, to order $(\frac{Z\alpha}{n})^4$, as predicted by Eq. (1.1).

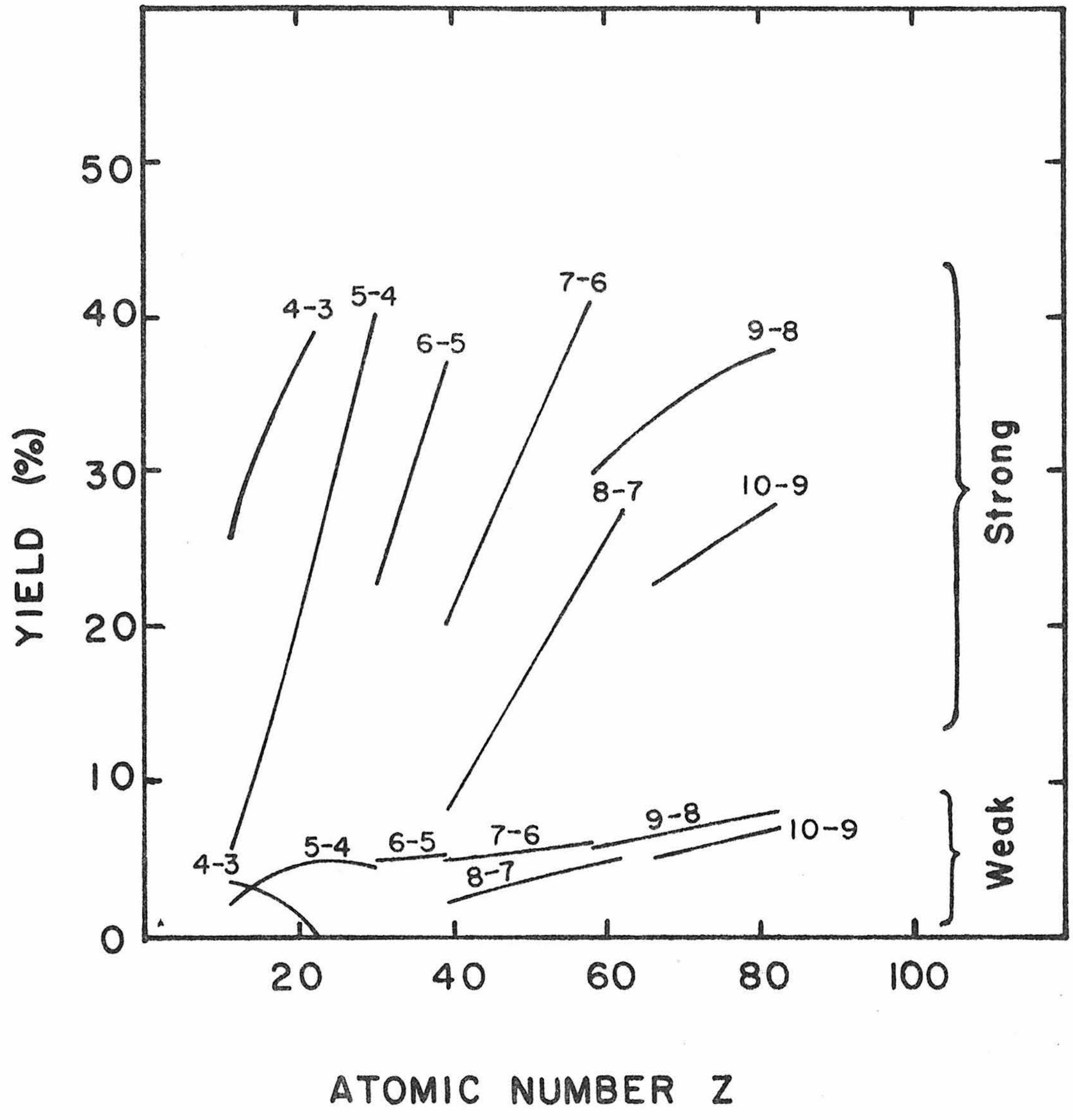

FIG. 5. Pionic x-ray yield as a function of atomic number Z. "Strong" indicates transitions between (n_i, $\ell_i = n_i - 1$) and (n_f, $\ell_f = n_f - 1$). "Weak" indicates transitions between (n_i, $\ell_i' = n_i - 2$) and (n_f, $\ell_f' = n_f - 2$).

Eq. (1.1). Fig. 5 illustrates the pionic x-ray yields, defined as the probability of emission of the x ray under consideration per π^- stop in the target, according to a cascade calculation.(22)

We have chosen the pionic Ti (Z = 22) 5g-4f and 5f-4d transitions for four reasons. (1) The transition energies are about 40.5 keV, well suited to our bent-crystal spectrometer. (2) Both transitions exhibit small strong interaction shifts and electron screening effects. The strong interaction shifts the 4d level by 3.9 eV, and the 5g, 5f, 4f levels by negligible amounts (Table 1). The electron screening affects the splitting by only -1.4 eV. (3) The pionic Ti 5g-4f and 5f-4d transitions can be well resolved by our bent-crystal spectrometer, which has a resolution of about 30 eV FWHM at 40.5 keV (Sec, 3.1). According to Eq. (1.1) the splitting has the value E(5f-4d) - E(5g-4f) = 59.2 eV. In order to compare this value with the experiment, corrections due to vacuum polarization, strong interaction and electron screening have to be included. As shown in Table 1 the total calculated splitting is 88.1 eV, with the maximum uncertainty estimated to be 1 eV. (4) The two transitions have reasonably high x-ray yields. According to the cascade calculation, the yield of π^- - Ti 5g-4f x rays is 24% and that of 5f-4d is 5% (Fig. 5). With these x-ray yields and the π^- beam intensity ($\sim 10^8$ π^-/sec) available at Los Alamos Meson Physics Facility (LAMPF) where this experiment was done, we estimated a peak counting rate of about 1/min(23) even though the efficiency, defined as the number of x rays detected at the peak of the diffraction line divided by the number of x rays emitted from the source (target), of our bent-crystal spectrometer is only 10^{-8}.

CHAPTER 3

EXPERIMENTAL METHOD AND RESULTS

In this chapter we describe the experimental part of this work in detail. The general setup, the bent-crystal spectrometer, monitor detector, background, and electronics used are discussed. We also report here the calibration of the spectrometer, data-taking procedures and analysis. The measured results are presented in the last section.

3.1 Experimental Setup

This experiment was carried out at the East Leg of the Stopped Muon Channel (SMC) at LAMPF. The lay-out of the channel and the experiment is shown in Fig. 6 and Fig. 7. Pions were produced when the 800 MeV proton beam of intensity 300 μA hit the production target A2. Negative pions of momenta 140 MeV/c were selected by two bending magnets BM01, BM02, and fourteen quadrupole magnets QM01 to QM14. The magnets were tuned to optimize the stopping rate of pions in the Ti target. The experimental area can be divided into three parts: (1) the target area which contains a polyethylene (CH_2) degrader and a metallic Ti target, (2) the crystal cave which contains a curved quartz (310) crystal, a sine-screw box and a Ge(Li) monitor detector, and (3) the slit cave which contains a 17.7 cm long curved slit and an array of high purity Ge detectors. The control and data signals are connected to an on-line PDP 11/34 computer. Details of each part are discussed below.

a) Target area. Besides the negative pions, the π^- beam contains also

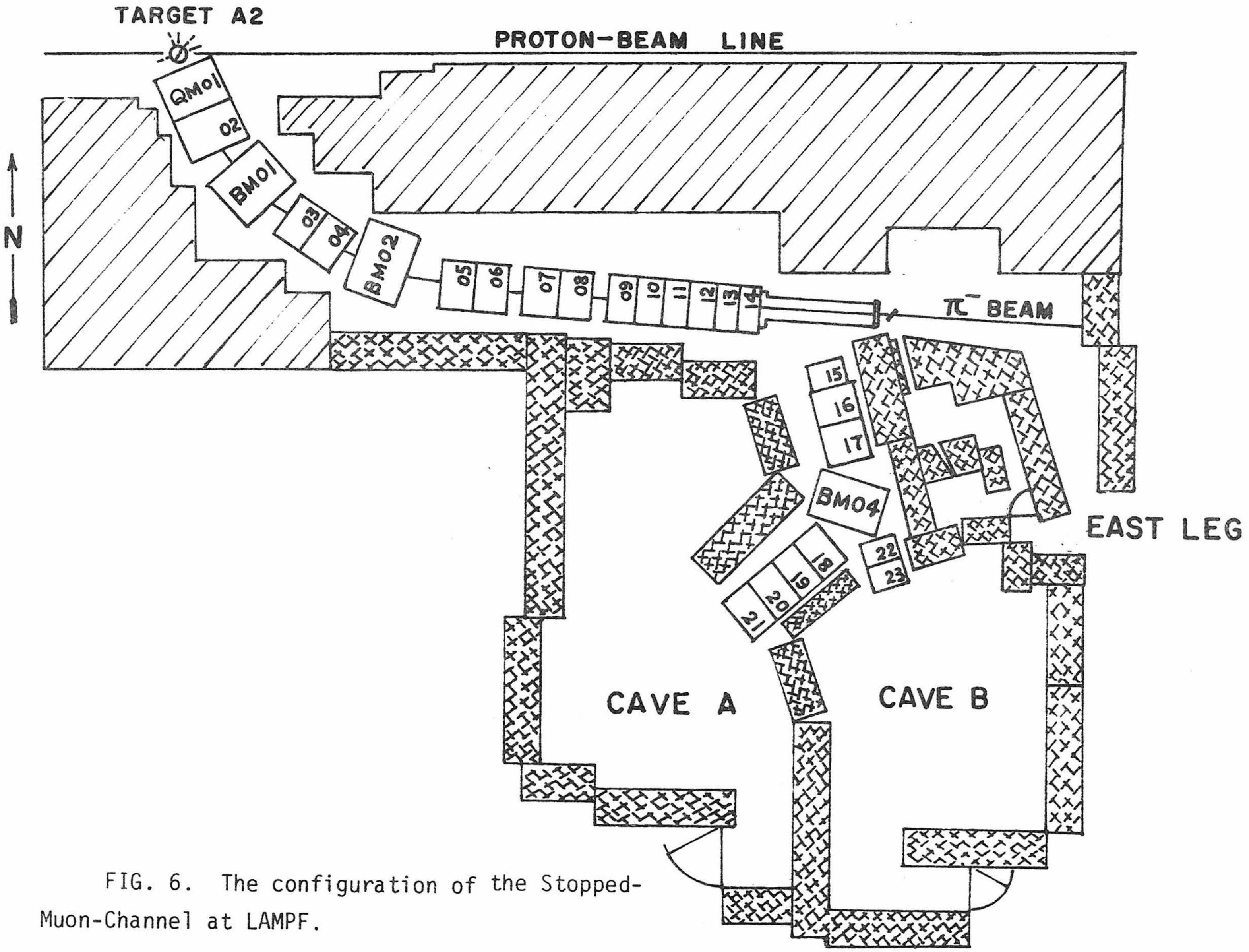

FIG. 6. The configuration of the Stopped-Muon-Channel at LAMPF.

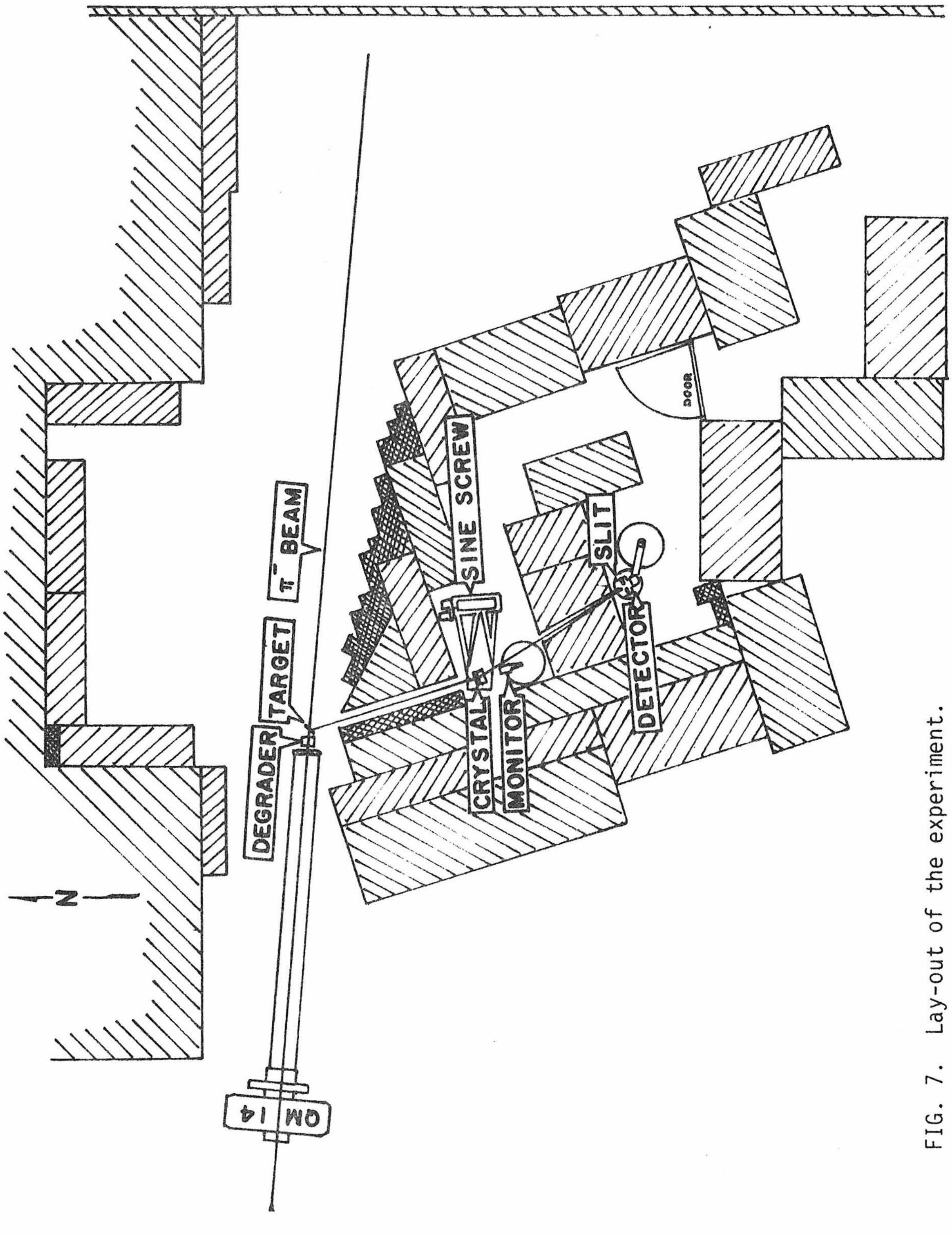

FIG. 7. Lay-out of the experiment.

muons and electrons generated from the production target A2 and the decay of the pions. The intensity ratio $\pi:\mu:e$ is about 3:2:0.5 obtained from a time of flight study. With the help of a wire chamber we found that the beam was about 25 cm wide and 15 cm high. The polyethylene degrader slowed down the π^-'s so that they could be stopped by the Ti target. A range curve that shows the counting rate of 4 - 3 and 5 - 4 pionic x rays seen by the monitor detector as a function of the degrader thickness is given in Fig. 8. The maxima of the 4 - 3 and 5 - 4 curves were at 12 cm CH_2 thickness. So we chose the thickness of degrader to be 12 cm. The Ti target had a surface density 1.3 g/cm^2 which equaled about twice the absorption length for the pionic x rays. Two different sizes of the Ti target were used. One was 10 x 10 cm^2 and the other was 14 x 10 cm^2. The angle of the Ti target with respect to the π^- beam could be controlled remotely by a Slo-Syn(24) stepping motor and was set to 40° to optimize the pionic x-ray intensity. During the experiment the π^- beam intensity was about 10^8 π^-/sec. About 10% of the pions were stopped by the Ti target and 1 x 10^6 5-4 pionic Ti x rays were emitted from the target per second.

b) Caltech-LAMPF bent-crystal spectrometer. The bent-crystal spectrometer used for this experiment has been described in detail in Ref. 8. Here we review the main parts of the spectrometer and discuss some modifications from Ref. 8. The spectrometer consists of two units, the crystal unit and the slit-detector unit. They were mounted in two independent, well shielded concrete caves, as illustrated in Fig. 7. The curved crystal at 2.3 m distance from the target consisted of an 11.5 x 9 cm^2 (310) quartz slab, 0.13 cm thick, with an aperture of 5 x 7 cm^2.

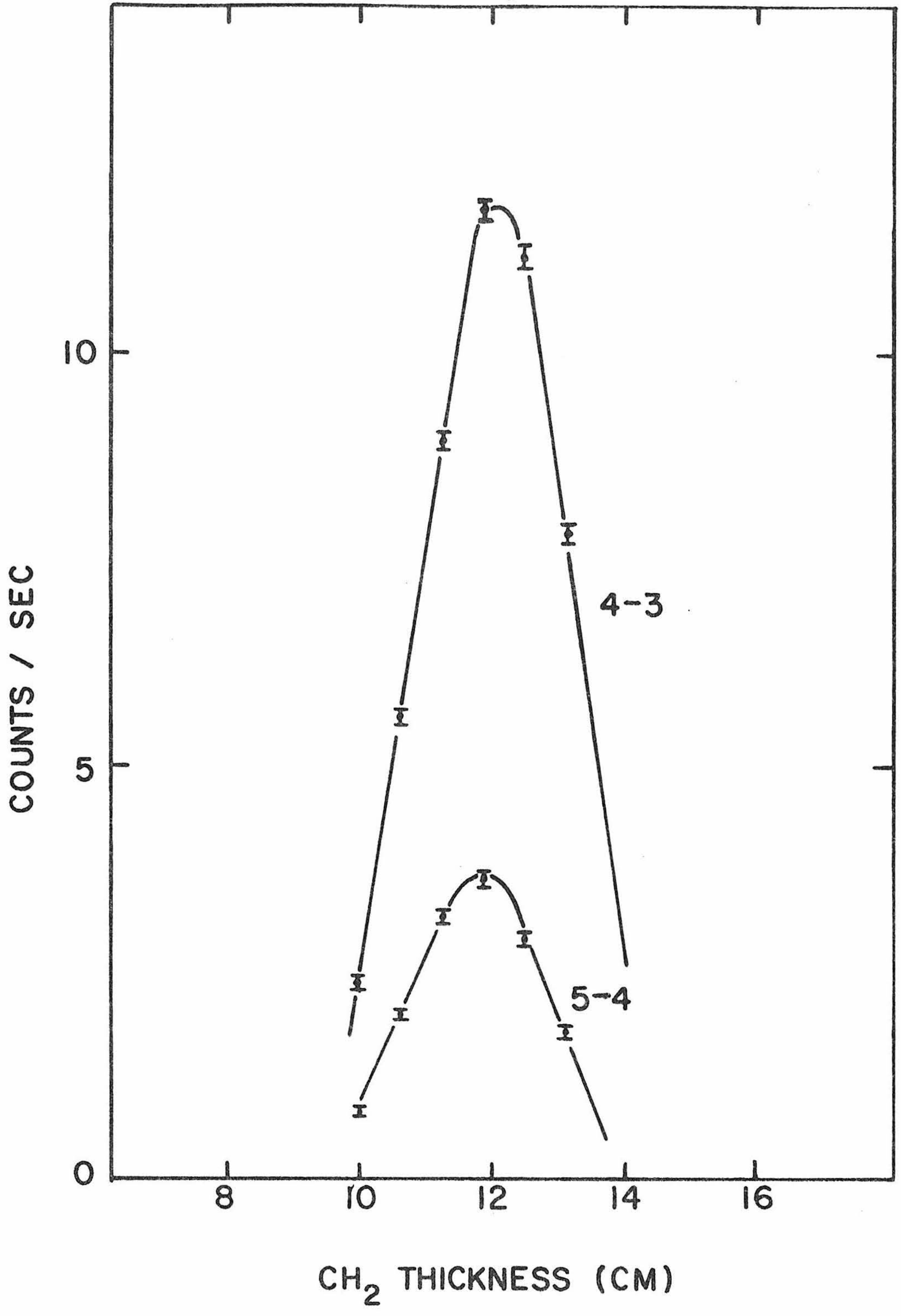

FIG. 8. Range curves of Ti 5-4 and 4-3 transitions. Solid lines are guides to the eyes only.

A Hartmann test(25) was performed to study the aberrations of the focus of the crystal (Appendix A). It showed that the bending radius R_f was 201.1 cm and the width of the aberration pattern at the best focal position was 0.12 mm, which corresponds to 18.6 eV at 40.5 keV. The lattice distance d of the (310) planes is 1180.1 mÅ at 18°C.(26) When the crystal was set at the angle that satisfies the Bragg condition

$$2d \sin\theta = n\lambda \tag{3.1}$$

where λ is the wavelength of the pionic x rays and n an integer denoting the order of diffraction, which was 1 in this measurement, the pionic x rays were diffracted and focused into a resolving slit. The slit was at $201.1 \cos\theta$ cm away from the crystal. It had a width of 0.15 mm and a length of 17.7 cm. As we use a long slit and an extended source (target) we must carefully consider the three-dimensional geometrical conditions leading to vertical divergence. The locus of the focal points is no longer a straight line, but the intersection of a cone and a cylinder with a radius of $R_f \cos^2\theta$.(8) Our slit was curved with a radius of 197.5 cm and had its azimuthal direction adjustable to fit the x-ray wavelength. The detector array behind the slit consists of four high purity Ge detectors, hence referred to as GE detectors.† Each of them is 4 cm high, 0.5 cm wide, and 0.5 cm thick and has an energy resolution of 1 keV FWHM at 40 keV.

The resolution of a bent-crystal spectrometer has contributions

---

†Manufactured by the Space Technology Products Laboratory of the General Electric Company, King of Prussia Park, Pennsylvania.

from the aberrations of the focal spot of the crystal, the slit width, the size of source, the crystal mosaic spread,(27) and the natural width of the line we want to measure. The mosaic spread of our bent quartz (310) crystal is about 10 sec (of arc), which corresponds to 15 eV at 40.5 keV. This means that 15 eV FWHM is the resolution of our spectrometer at 40.5 keV for a point γ-ray source and an infinitesimal slit. During this experiment the total resolution of our spectrometer was found to be 32 eV FWHM for the 10 x 10 cm^2 target at 40.5 keV.

c) The monitor detector. A Ge(Li) detector was used to monitor the π^- beam intensity and normalize accordingly the counting rate of the GE detectors. It has a sensitive area of a circular disk with a 2-inch diameter. The monitor detector, looking into the Ti target, was set behind the crystal and out of the way of the diffracted pionic x rays (as shown in Fig. 7). Fig. 9 shows the energy spectrum seen by this detector. The energy resolution was 0.9 keV FWHM at 40 keV. The 5g - 4f and 5f - 4d transitions could not be resolved here. For better statistics the counts under the 4-3 peak were used for normalization in the data analysis (Sec. 3.4).

d) Background. Due to the low efficiency of the bent-crystal spectrometer and the high background of neutrons and γ rays near a powerful accelerator, the background problem is very important. It is critical for the feasibility of the precision experiment under discussion, and if shown feasible, contributes to the estimate of the running time and the accuracy of our measurement of the energy splitting (Sec. 3.3 and Appendix B). The separation of the spectrometer into two parts, with a

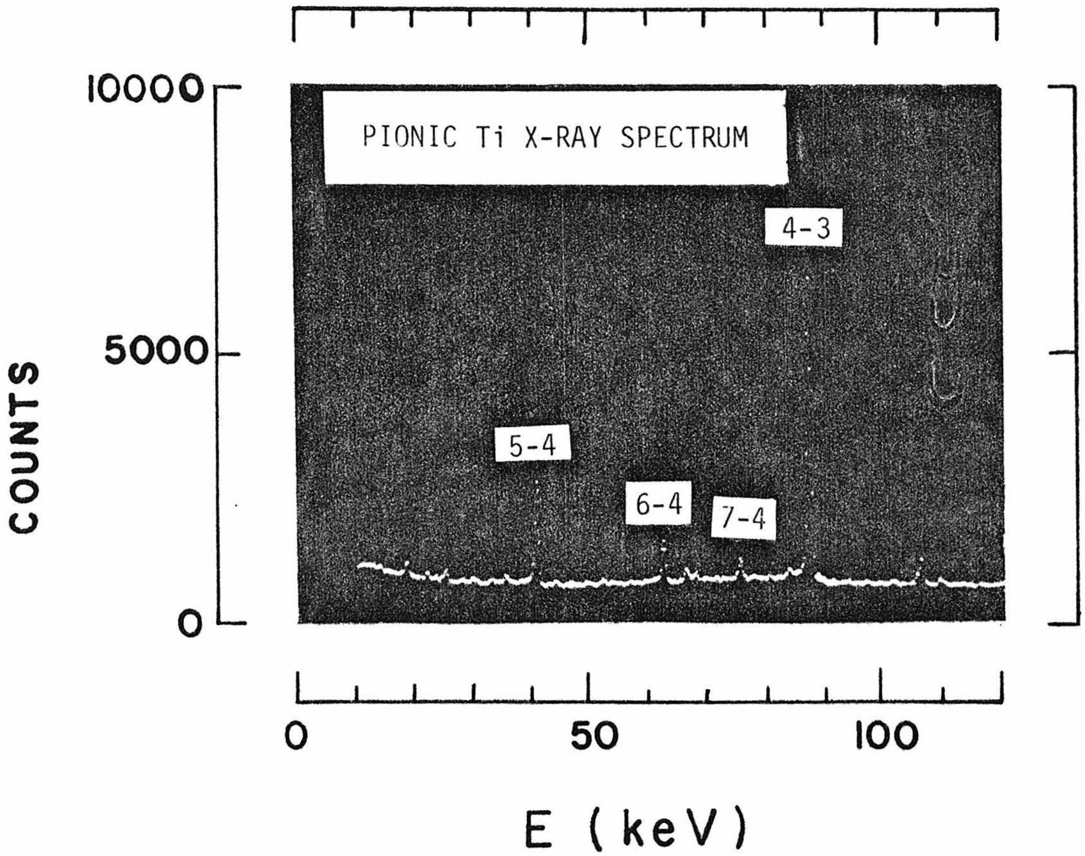

FIG. 9. Pionic Ti x-ray spectrum seen by the monitor detector.

1.2 m thick concrete wall between them, helped to reduce the background considerably. A 10 cm lead shield covered about 4/5 of the 4π solid angle around the detector array. The good energy resolution of the GE detectors also helped to reduce the background. We managed to get a background rate of 0.2 counts/min in our final pionic Ti 5-4 spectra.

Six cylindrical veto tanks, with a diameter of 15 cm, filled with NE 235H liquid scintillator were constructed and used to cover about 1/3 of the 4π solid angle, outside the lead shield of the detector array. It turned out that they did not help to reduce the background.

e) Electronics. The block diagram of the electronics we used is shown in Fig. 10. The spectrometer control and data taking were handled by a PDP 11/34 computer via a Tennecomp Hyccups-M Data Acquisition System.(28,29) The signal from each detector was divided into two parts: a linear signal and a fast timing signal. With the help of discriminators and OR gates we had an event signal. It was combined with the beam gate (7% duty cycle and 120 pulses/sec) through an AND gate. This beam-gated event signal was input to the multiplexer control before its corresponding linear signal was accepted by the multiplexers and digitized by the 8 k-channel ADC. The linear signals from the four detectors of the array went through a mixer router. The three multiplexers had a similar routing function. The mixer router and the multiplexers allowed us to use only one ADC to generate five energy spectra from the five detectors.

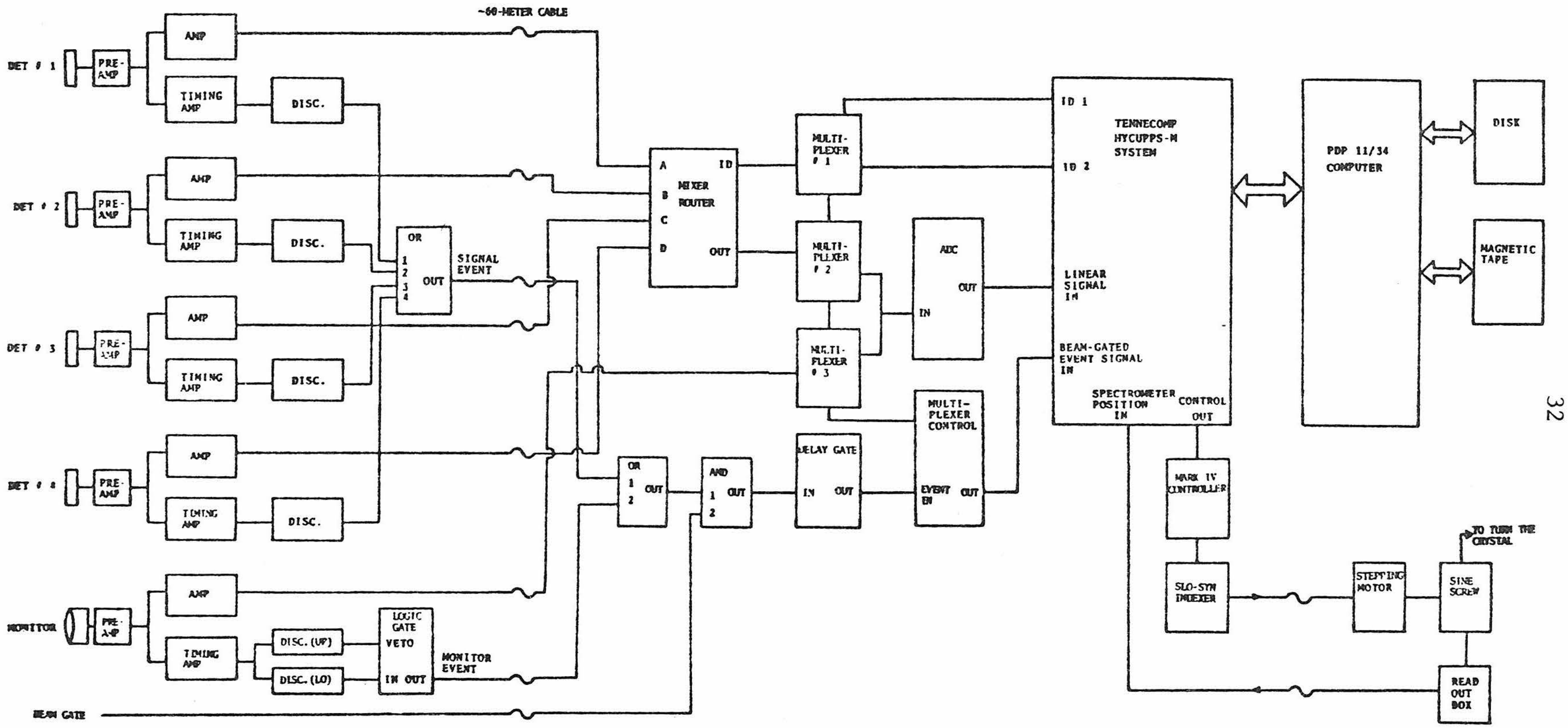

FIG. 10. The block diagram of the electronics.

The computer could set and read the angular position of the crystal with the help of a DR 11-C stepmotor interface,(29) a home-made Mark IV controller, and a read-out box. The whole system could run automatically with the help of a FOCAL-11 program.

3.2 Calibration

The angular position of the crystal was set with the help of a sine screw,(30,31) and read in units of screw divisions (S.D.). The sine screw was designed in such a way that the crystal could be turned in units proportional to sin θ, to make the relation between S.D. and wavelength linear, i.e.

$$\lambda = m(S.D.) + a. \tag{3.2}$$

After each setup of the spectrometer, a calibration with x rays or γ rays of known energies is necessary. In this measurement we used Eu $K\alpha_{1,2}$ and Sm $K\alpha_{1,2}$ x rays, since their wavelengths are very close to the pionic lines under investigation. The energies, wavelengths(32) and Bragg angles θ of the calibration lines as well as those of the π^--Ti 5-4 lines are listed in Table 2. The calibration Eu and Sm x rays were produced by fluorescent excitation of Eu_2O_3 and Sm_2O_3 targets (0.15 g/cm^2 and 0.13 g/cm^2 respectively) using a 3-Curie ^{241}Am source, which emits 59.54 keV γ rays. These targets, 8 cm x 8 cm in size, were placed in front of the ^{241}Am source substituting for the Ti target. The

TABLE 2. Comparison of the energies, wavelengths, and the Bragg angles of the calibration lines and the π^- - Ti 5-4 lines.

	E (keV)	λ ($m\mathring{A}^*$)[a]	θ (°)
Eu $K\alpha_1$	41.5422	298.446[b]	7.28
$K\alpha_2$	40.9019	303.118[b]	7.39
π^--Ti 5f-4d	40.5535	305.732	7.46
5g-4f	40.4659	306.394	7.47
Sm K_{α_1}	40.1181	309.040[b]	7.54
$K\alpha_2$	39.5224	313.698[b]	7.65

[a] $1\ \mathring{A}^* = 1.0000205(56)\ \mathring{A}$ (Ref. 32).

[b] The errors of these wavelengths are 0.002 $m\mathring{A}^*$.

observed x-ray profiles were analyzed by comparing with the convolution of Gaussian and Lorentzian functions over a linear background$^{(33)}$

$$f(i) = B_0 + B_1 i + A \int_{-\infty}^{\infty} \frac{\exp\left[-\frac{4\ell n 2(i-i')^2}{\Gamma^2}\right]}{(i'-c)^2 + \frac{\Gamma'^2}{4}} di', \tag{3.3}$$

where c is the centroid of the line. The Lorentzian widths Γ' of these x rays are well known and are listed in Table 3. In the least-squares fits the following parameters were varied: B_0, B_1, A, Γ, and c; and Γ' was fixed. A typical fit is shown in Fig. 11. The centroids, in units of S.D., of the four x-ray lines were then obtained. In Fig. 12 we plotted the wavelengths of the calibration lines as a function of their centroids. The expected positions of the pionic lines were also indicated. The errors were too small to be shown in this scale. We noted that the linearity of the sine screw assumed in Eq. (3.2) was well confirmed. A linear fit gave us the slope m and the offset a.

During the experiment two target positions were chosen. In the second position the Ti target was lower by 0.25 cm than in the first position (see Sec. 3.3). Independent calibrations were carried out for both positions. Tables 4a and 4b summarize the wavelengths, centroids of the calibration peaks and the results of the linear fits for both positions.

TABLE 3. Natural linewidths of the calibration x rays in energy and wavelength units.

	Natural Linewidth Γ' [a,b] (eV)	(mÅ)
Eu $K\alpha_1$	24.96	0.1793
$K\alpha_2$	25.22	0.1869
Sm $K\alpha_1$	23.60	0.1818
$K\alpha_2$	23.87	0.1894

[a] See Ref. 34.

[b] Errors were estimated to be 3%

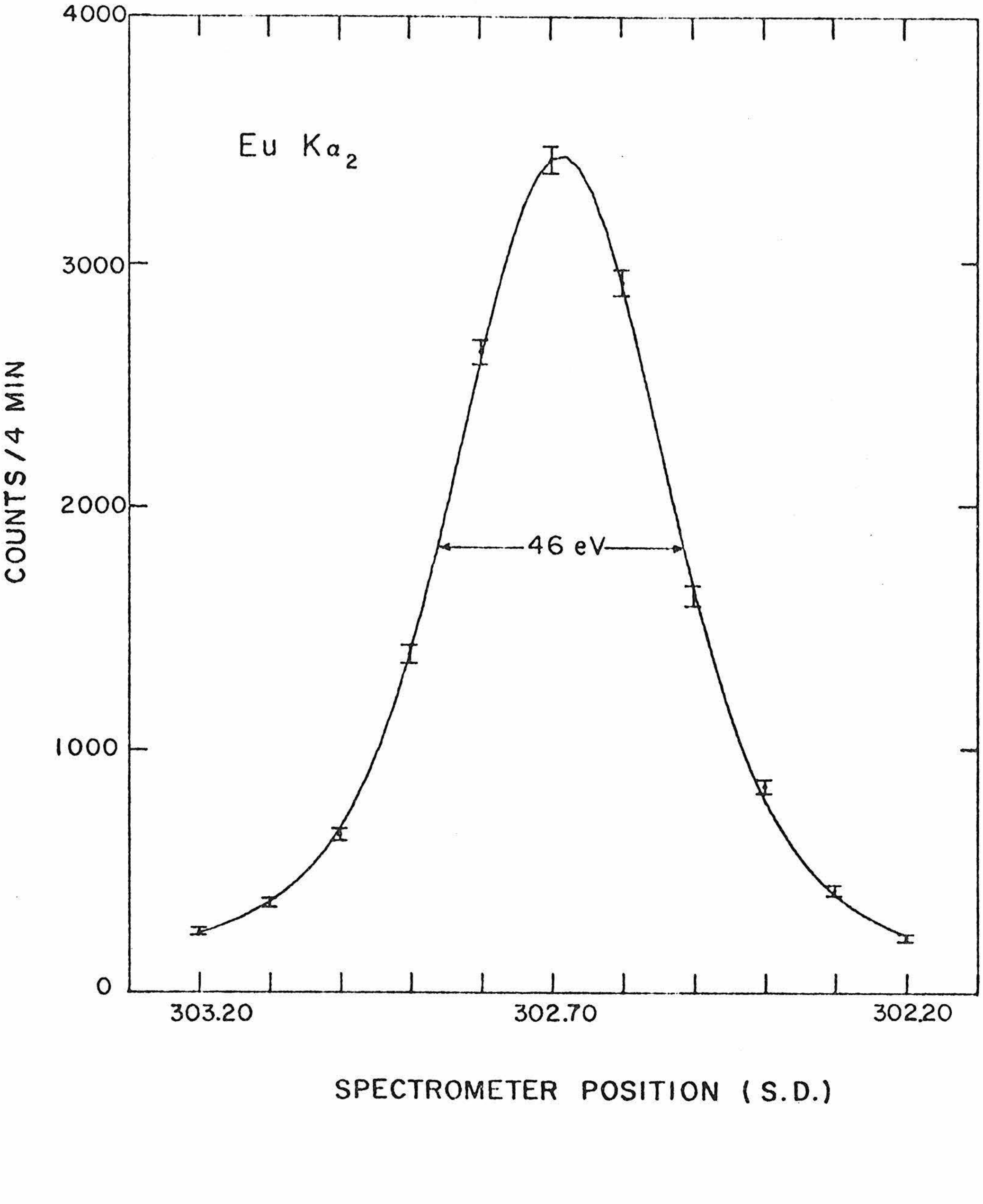

FIG. 11. Eu $K\alpha_2$ calibration line. The solid line represents the least-squares fit of the data, with a χ^2 per degree of freedom of 1.1.

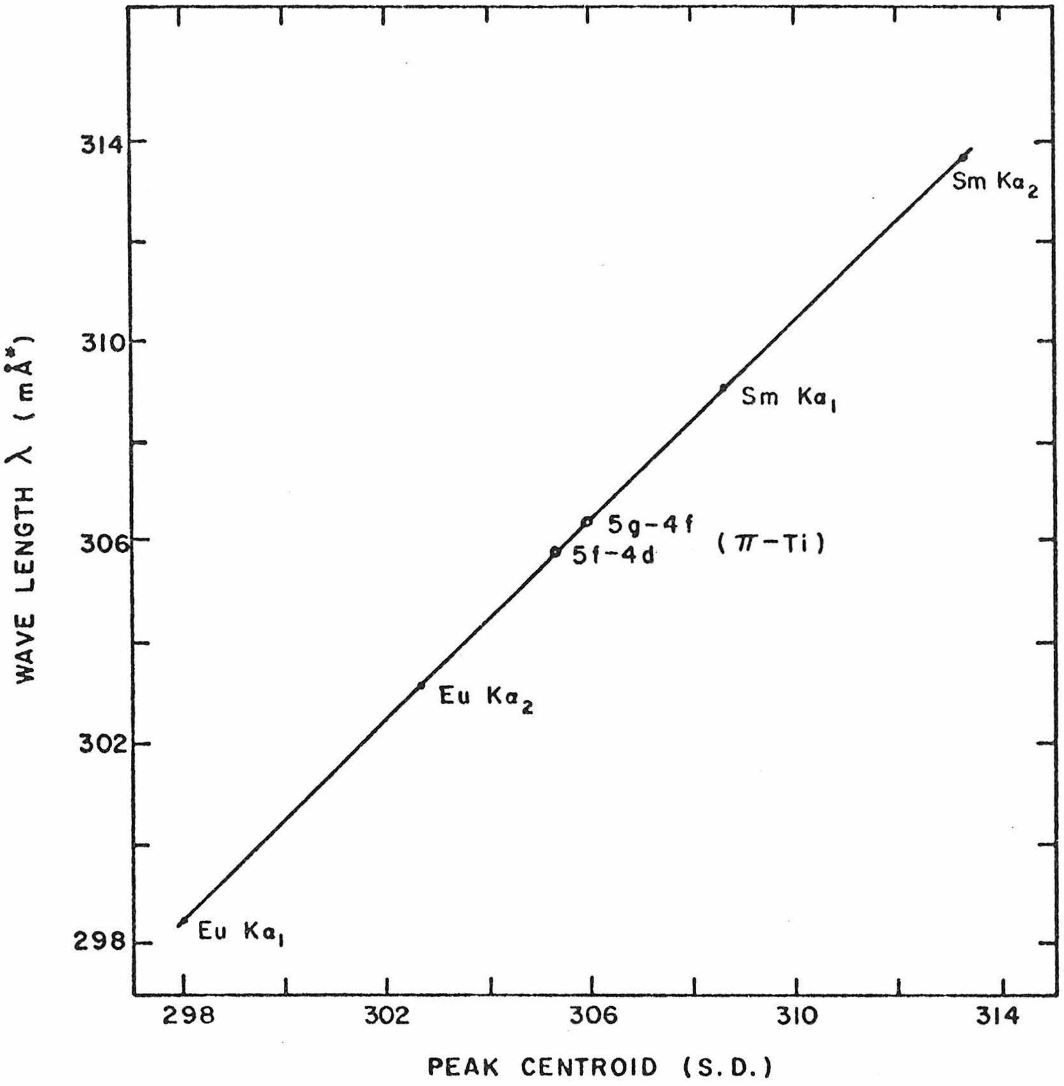

FIG. 12. The wavelengths of the calibration lines as a function of their centroids.

TABLE 4a. Summary of wavelengths and centroids of the calibration peaks.

Lines	Wavelength λ ($m\overset{0}{A}^*$)	Centroid (S.D.) 1st Position	Centroid (S.D.) 2nd Position
Eu $K\alpha_1$	298.446(2)	298.038(2)	298.033(2)
$K\alpha_2$	303.118(2)	302.686(2)	302.686(2)
Sm $K\alpha_1$	309.040(2)	308.572(2)	308.578(2)
$K\alpha_2$	313.698(2)	313.204(2)	313.221(2)

TABLE 4b. Result of the linear fit to $\lambda = m(S.D.) + a$.

	1st Position	2nd Position
Slope m ($m\overset{0}{A}^*$/S.D.)	1.0057(2)	1.0044(2)
Offset a ($m\overset{0}{A}^*$)	-1.302(72)	-0.888(81)
Correlation $<\sigma_m \sigma_a>$	-1.689×10^{-3}	-2.148×10^{-3}

3.3 Data Taking

The 5g - 4f and 5f - 4d peaks were continuously scanned in rapid succession. A scan encompassed 18 to 22 points. The interval between two points was 0.10 S.D. which corresponded to 13.3 eV. One scan lasted about three hours. 62 scans were taken. At each spectrometer position during each scan the energy spectra of the GE detectors and the monitor detector were measured for a certain amount of time and stored on magnetic tapes. The choice of the counting-time interval is discussed below. Besides controlling the spectrometer and taking data for each scan-position, our on-line system also calculated the monitor rate in the neighborhood of the 4-3 line and summed the signal counts, in the energy window of 40.5 ± 1.0 keV (for π^- - Ti 5 - 4's), seen by the GE detectors. The monitor rate was about 600/min. In case the rate dropped below 60% of this value ("beam off" periods), the measurement of the 5 spectra was repeated at the same spectrometer position. The values of the summed signal counts were printed out immediately so that we could have a preliminary spectrum of the π^- - Ti 5g-4f and 5f-4d transitions during the experiment.

To minimize the statistical error of the splitting, the measurement periods for the weak peak (5f - 4d) were longer than those for the strong peak (5g - 4f). The optimum counting periods were found by the following considerations. An empirical formula(35) which gave the error of the centroid σ_c as a function of the resolution Γ, the background to peak ratio R, and the total number of signal counts N was derived by Stephen Kellogg (Appendix B). For a large R ($\gtrsim$ 0.5), the empirical formula is

$$\frac{\sigma_c}{\Gamma} = 0.7160\sqrt{\frac{R+\frac{1}{2}}{N}} \quad . \tag{3.4}$$

Let the error of the difference in centroid of two lines 1,2 be σ_d, then

$$\sigma_d^2 = \sigma_{c_1}^2 + \sigma_{c_2}^2 = (0.7160\Gamma)^2 \left(\frac{R_1+\frac{1}{2}}{N_1} + \frac{R_2+\frac{1}{2}}{N_2}\right) . \tag{3.5}$$

Here we neglected the correlation of c_1 and c_2, since in our case the two lines were fully resolved and the correlation turned out to be negligible. Let f be the ratio of the two signal counting rates s_1 and s_2, i.e. $f = \frac{s_1}{s_2}$, and t_1, t_2 the two counting time intervals, then

$$R_2 = fR_1 \ ; \quad N_1 = t_1 s_1 \ ; \quad N_2 = t_2 s_2 = (T - t_1) s_2 \tag{3.6}$$

where $T(= t_1+t_2)$ is proportional to the total beam time. To minimize σ_d^2 in Eq.(3.5) by using Eqs. (3.6) and setting $\frac{d\sigma_d^2}{dt_1} = 0, \frac{d^2\sigma_d^2}{dt_1^2} > 0$, we obtained

$$\frac{t_2}{t_1} = \sqrt{\frac{f(fR_1+\frac{1}{2})}{(R_1+\frac{1}{2})}} \tag{3.7}$$

In our case, let 1 be the 5g-4f line and 2 be the 5f-4d line, we had $f \simeq 5$, $R_1 \simeq 0.5$, and $\frac{t_2}{t_1} \cong 4$. Therefore, the counting time interval of the points under the weak peak was, in general, chosen to be four times longer than those under the strong peak.

We divided the total scans into three groups, in the order of the time sequence, I, II, and III. In group I, which contained 50% of the total data, a Ti target of a size 10 cm x 10 cm was used. In groups II and III, which contained 10% and 40% of the total data respectively, a 10 cm x 14 cm target was used. Between groups I and II, there was accelerator maintenance for 16 hours. Between groups II and III, the target position was lowered by 0.25 cm. After the maintenance the beam density had changed. We could not see the expected 40% increase of the pionic x rays due to a larger target. The data of the three groups were analyzed separately.

The spectrometer was calibrated with good statistics during the maintenance period and once again at the end of the beam-time. The results of these calibrations were shown in Table 4.

The energy calibrations of the GE detectors were checked and the temperature in the crystal cave was measured every day. Detector channel 1 turned out to have a slight gain shift. The other channels were very stable. The temperature increased smoothly by a rate of 1^{0}C per week, following the trend of the season.

3.4 Data Analysis

A flow chart which shows the procedures of data analysis is shown in Fig. 13.

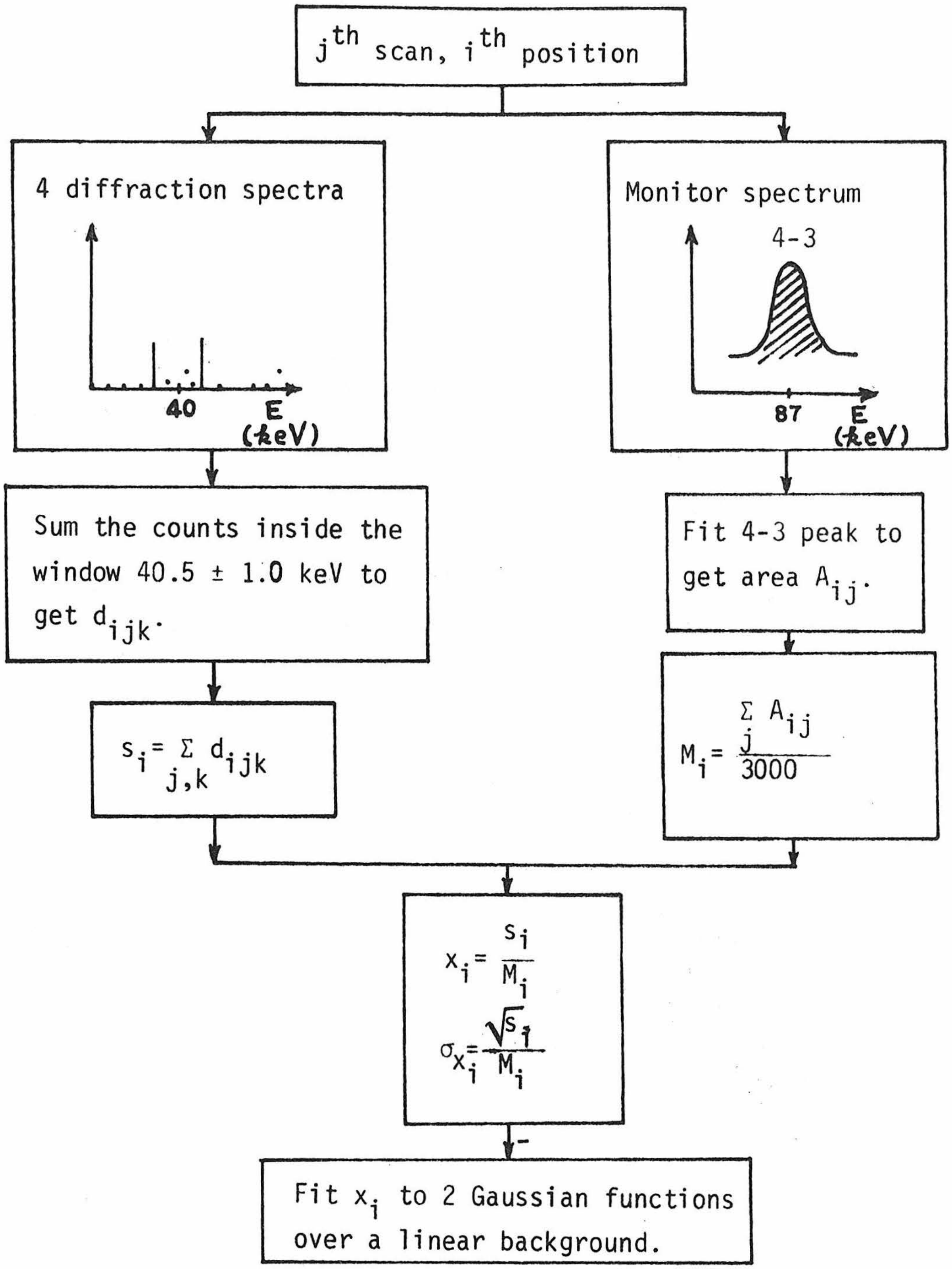

FIG. 13. Flow chart of data analysis procedures. Here i indicates the spectrometer position, j indicates the scan number, and k indicates the GE detector number.

The first part of the analysis was done by using a FOCAL-11 program on the PDP 11/34 computer. We had 5 spectra for each scan-position (j^{th} scan, i^{th} position). The monitor spectrum had a strong 4 - 3 peak. This peak was least-squares fitted to a Gaussian function over a linear background. The area A_{ij} within the fitted Gaussian function was used to normalize the signal counts of the GE detectors. The counting rate of the GE detectors was very low, a few counts per minute. The GE spectra looked flat. For each of these spectra, the sum of the number of counts inside the energy window of 40.5 ± 1.0 keV was calculated. Let us denote this sum d_{ijk}, where $K = 1$ to 4 indicates the GE detectors. The numbers A_{ij}, d_{ijk}, and the counting time interval T_{ij} were brought back to Caltech for further analysis using an IBM/370 computer.

In each group, for each spectrometer position i we summed d_{ijk} over the detectors k and the scans j to get the signal count s_i. We also summed A_{ij} over j and divided the result by 3000, an arbitrary constant introduced for convenience of calculation, to get M_i. s_i was then divided by M_i to get the normalized signal count x_i. Since the percentage error of M_i was negligible compared with that of s_i, the error of x_i is $\sqrt{s_i}/M_i$. The resulting spectra, which are the pionic Ti 5 - 4 spectra we want, are shown in Fig. 14. In Fig. 14 the vertical coordinate has been properly scaled to counts per minute.

The final three spectra were then fitted to the sum of two Gaussian functions with identical widths above a linear background

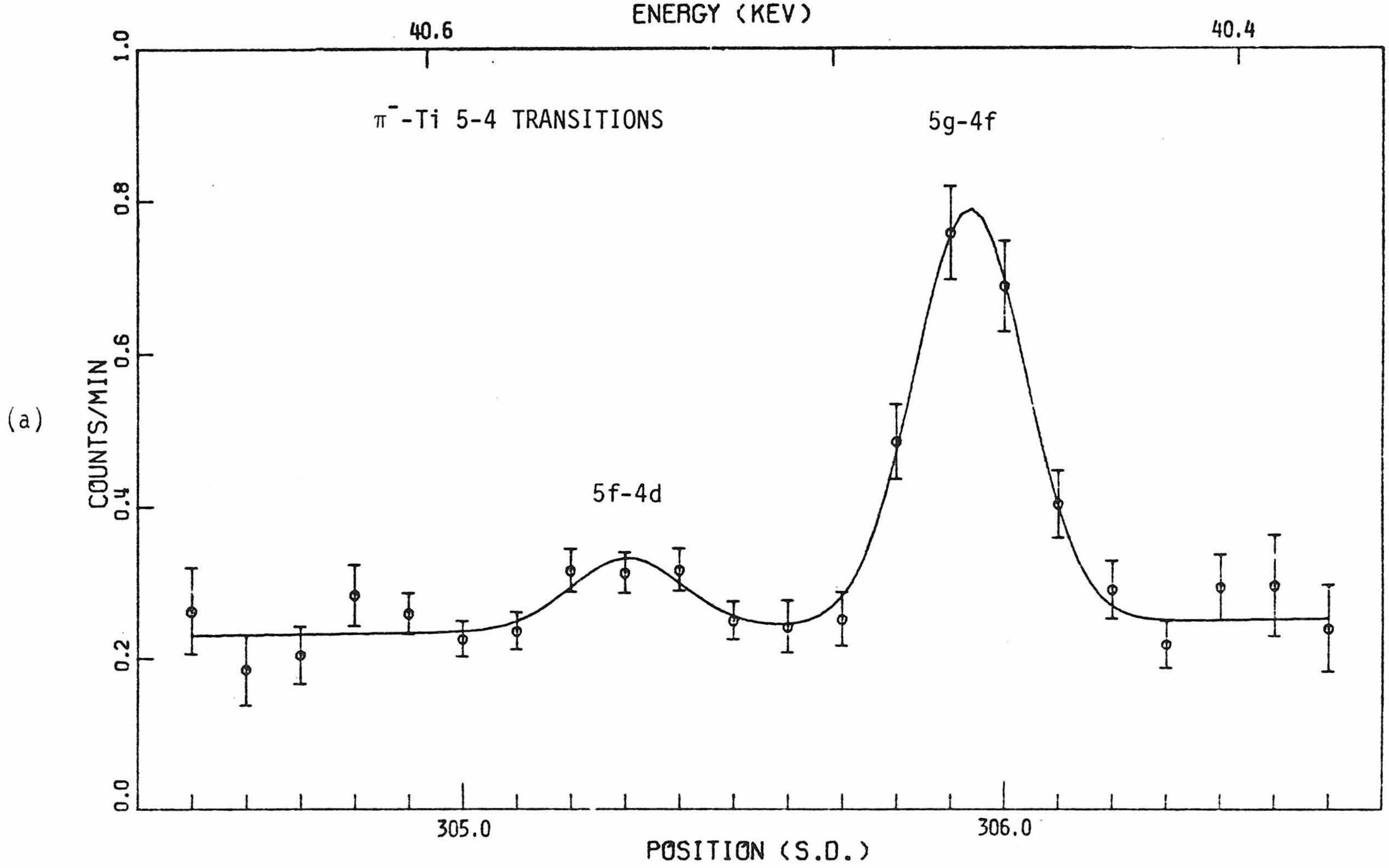

FIG. 14. Pionic Ti 5-4 transitions: data and fits of (a) group I, (b) group II, and (c) group III.

(b)

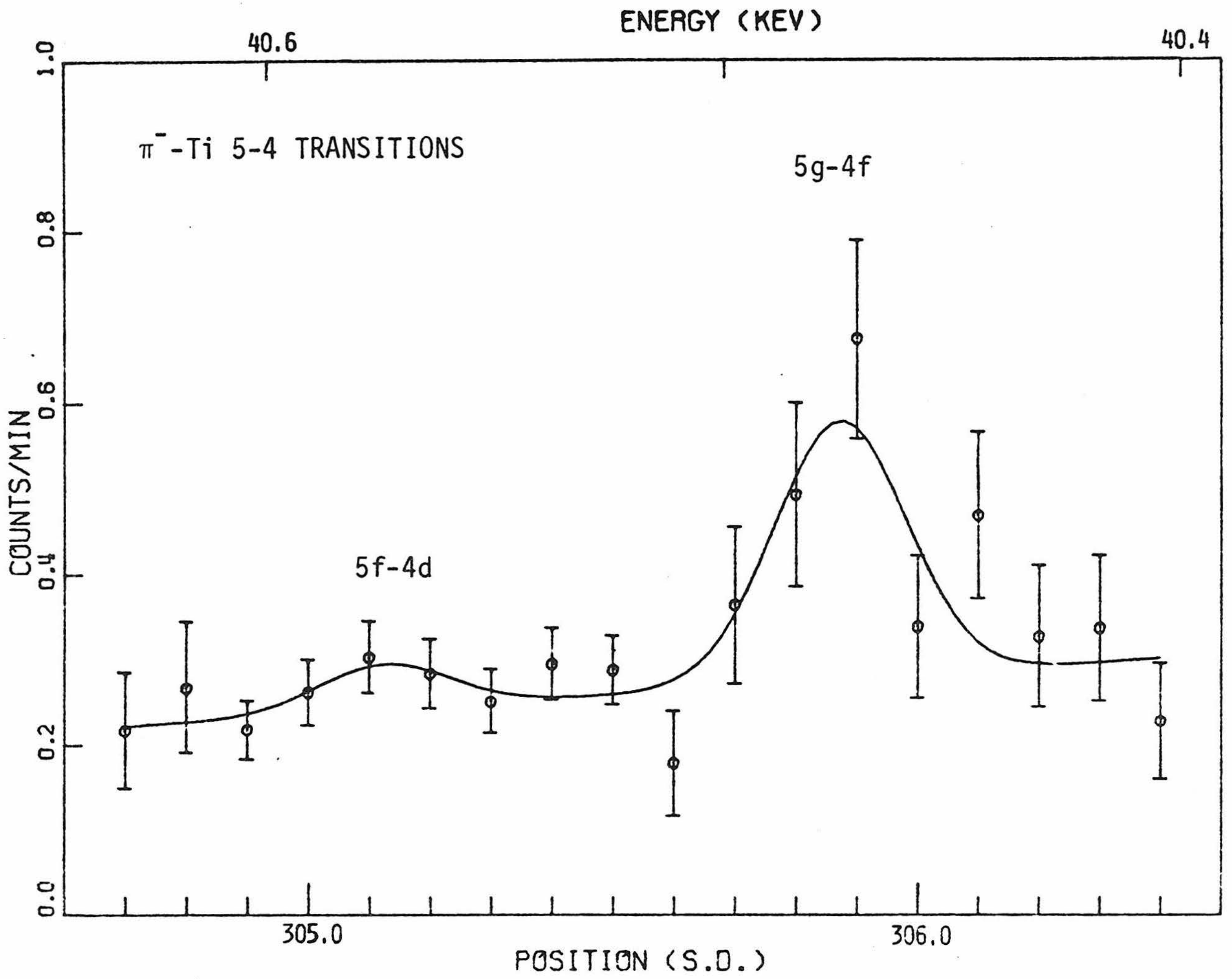
ENERGY (KEV)
40.6
40.4
π⁻-Ti 5-4 TRANSITIONS
5g-4f
5f-4d
COUNTS/MIN
1.0
0.8
0.6
0.4
0.2
0.0
305.0
306.0
POSITION (S.D.)

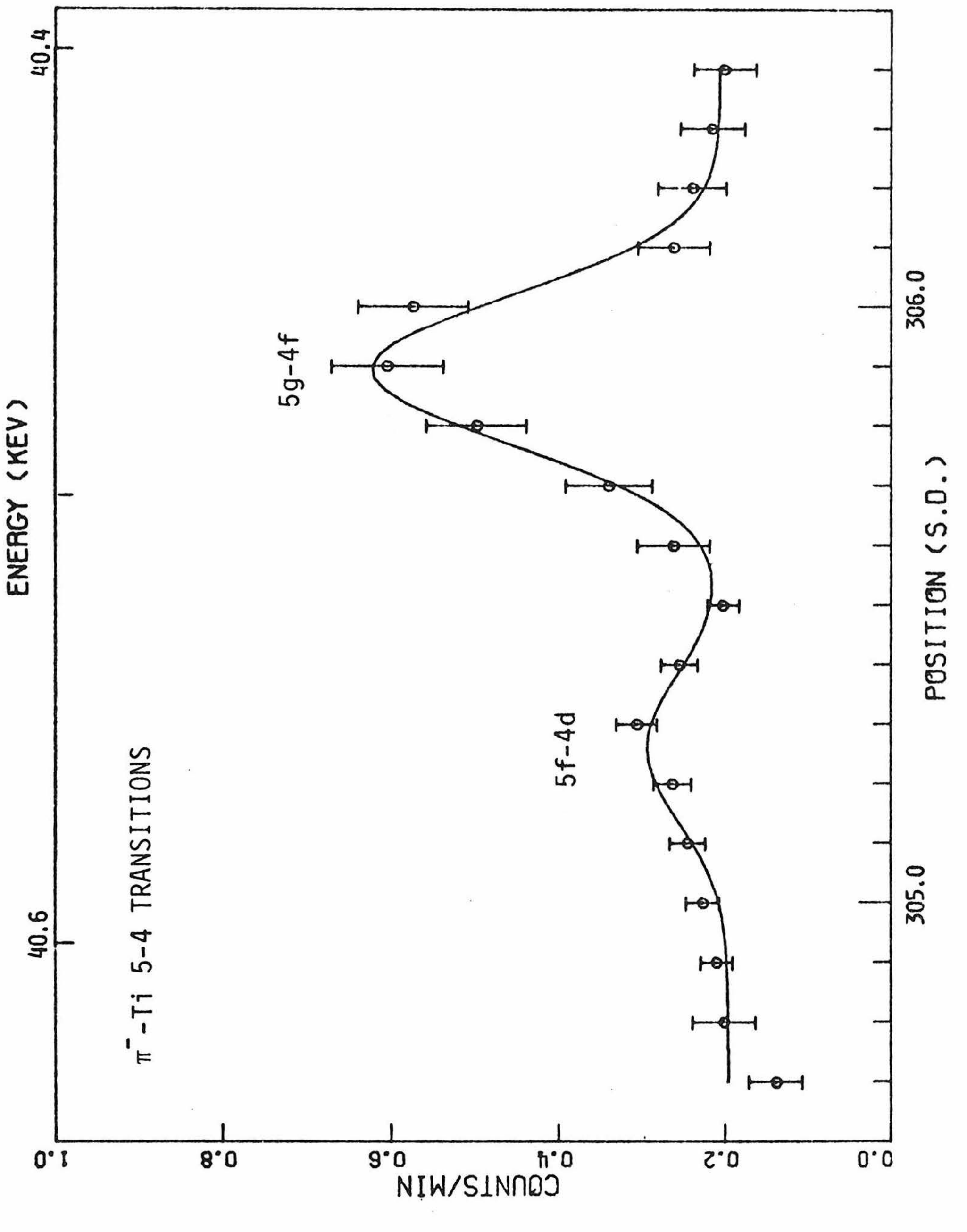
ENERGY (KEV)
40.6
40.4
π⁻-Ti 5-4 TRANSITIONS
5g-4f
5f-4d
POSITION (S.D.)
305.0
306.0
COUNTS/MIN
0.0
0.2
0.4
0.6
0.8
1.0

(c)

$$f(i) = B_0 + B_1 i + A_1 \exp\left[-\frac{4\ln 2(i-c_1)^2}{\Gamma^2}\right] + A_2 \exp\left[-\frac{4\ln 2(i-c_2)^2}{\Gamma^2}\right] \quad (3.8)$$

with A_1, A_2, c_1, c_2, B_0, B_1, and Γ (except for group II) as variable parameters. Since we had very little data in group II, we had to use a fixed Γ to get a reasonable fit. The results of the fitted centroids c_1, c_2 are shown in Table 5. Those of the fitted amplitudes A_1, A_2 are shown in Table 6. The fitted curves are also shown in Fig. 14. The χ^2's per degree of freedom of fits I, II, and III are 0.7, 0.9, and 0.9 respectively.

3.5 Results

From the measured centroid (S.D.) and the calibration shown in Table 4b, we can get the wavelength λ by Eq. (3.2), i.e.

$$\lambda = m(S.D.) + a \ .$$

Since the errors of m and a are highly correlated, we have

$$\sigma_\lambda = \sqrt{(S.D)^2\sigma_m^2 + \sigma_a^2 + 2(S.D.)\langle\sigma_m\sigma_a\rangle + m^2\,\sigma_{(S.D.)}^2}\ . \quad (3.9)$$

The calculated λ, and σ_λ are shown in Table 5. To transform λ into energy E, we used the relation $E\lambda = 2\pi\hbar c$ and the values of $\hbar$ and c given in Ref. 36. Taking into account that $1\overset{\circ}{A}{}^* = 1.0000205(56)\,\overset{\circ}{A}$ (32) we got

$$E\lambda = 12398.26(8)\ \text{eV}\ \overset{\circ}{A}{}^* . \quad (3.10)$$

TABLE 5. Measured centroids, wavelengths, energies, and the fine-structure splitting of the pionic Ti 5g-4f and 5f-4d transitions.

Group	Measured[a,b] Quantities	5g-4f	5f-4d	Splitting (eV)
I	S.D.	305.937(10)	305.304(32)	
	λ	306.389(10)	305.753(32)	
	E	40465.7(1.3)	40549.9(4.2)	84.2(4.4)
II	S.D.	305.873(34)	305.125(83)	
	λ	306.325(34)	305.573(83)	
	E	40474.2(4.5)	40573.8(11.0)	99.6(11.9)
III	S.D.	305.894(16)	305.260(28)	
	λ	306.341(16)	305.705(28)	
	E	40472.1(2.1)	40556.3(3.7)	84.2(4.3)
Weighted mean of the splitting				85.2(3.0)

[a] λ's are in units of m$\mathring{A}^*$. E's are in units of eV.

[b] $E\lambda$ = 12398.26(8) eV $\mathring{A}^*$.

TABLE 6. Measured peak intensity ratio of the pionic Ti 5g-4f and 5f-4d transitions.

Group	Peak height of[a] 5g-4f A_1	Peak height of[a] 5f-4d A_2	Ratio A_2/A_1 (%)
I	2.77(0.27)	0.48(0.12)	17.3(4.6)
II	1.55(0.44)	0.27(0.21)	17.4(14.4)
III	2.14(0.26)	0.49(0.11)	22.9(5.8)
Mean of Ratio			19.3(3.5)

[a] Peak heights A_1 and A_2 are in units of signal counts per 3000 monitor counts.

Also shown in Table 5 are the energies calculated according to Eq. (3.10). We then have the measured energy splitting by taking the difference of the energies of the 5g-4f amd 5f-4d transitions. The results of the three groups are consistent with each other. The weighted mean of them is our final result of the energy splitting, 85.2(3.0) eV.

In Table 6, it is shown that the measured peak intensity ratio A_2/A_1 is $(19.3 \pm 3.5)\%$. This is in agreement with the yield ratio 0.05/0.24 ($\cong 21\%$) (see Fig. 5) according to a cascade calculation.

CHAPTER 4

DISCUSSION

The systematic errors in this experiment are discussed in the first section. We draw a conclusion of the present work in the second section. At the end a possible extension of this experiment is discussed.

4.1 Systematic Errors

As we compare the measured energies of the π^--Ti 5g-4f and 5f-4d transitions with the calculated ones in Table 1, we have to consider the systematic errors associated with our experiment. There are two sources of systematic error. (1) The distribution of pions stopped in the Ti target and the distribution of ^{241}Am powder in the fluorescense source for calibration x rays were not identical. The stopped pions were about uniformly distributed over the Ti target. But the ^{241}Am powder was distributed more in the lower part than in the upper part of the source. So the pionic x rays and the calibration x rays illuminated the crystal differently. A systematic error as large as 0.03 S.D.(equivalent to 4 eV at 40 keV) could be generated. (2) Another source of systematic error is the temperature change. It affects the interplanar distance d of the crystal. Our spectrometer has a temperature correction 0.005 $m\overset{0}{A}^*/^0C$ (Ref. 8). Since the temperature in the crystal cave increased by a rate of 1^0C/week, a systematic error of less than 0.6 eV could be generated. However, these mentioned systematic errors have a negligible effect on the result of our measured energy splitting, since we took the difference of the two pionic transition energies and their systematic errors cancelled each other.

4.2 Conclusion

The observed energy difference of the pionic Ti 5g-4f and 5f-4d transitions is 85.2 ± 3.0 eV. The calculated splitting is 88.1 eV. In comparing the two values we note that there is good agreement between experiment and calculation. The present results thus constitute a test of the relativistic equations of motion (Relativistic Schrödinger and Klein-Gordon) for a charged spinless particle in a Coulomb field.

4.3 Outlook

To order $(\frac{Z\alpha}{n})^4$ the relativistic Schrödinger (RS) and Klein-Gordon (KG) equations predict the same energy levels, Eqs. (2.5) or (2.8), for a charged spinless particle in a Coulomb field. The predictions differ in the terms of order $(\frac{Z\alpha}{n})^6$ and higher. It can be shown (Appendix C) that to order $(\frac{Z\alpha}{n})^6$ the difference in energy eigenvalues predicted by these two equations is

$$\Delta_{n\ell} \equiv (E_{n\ell})_{KG} - (E_{n\ell})_{RS} = \left\langle \psi_{n\ell} \right| \frac{1}{32m^4} \left[\vec{p}^{\,2}, \left[\vec{p}^{\,2}, e\phi\right]\right] \left| \psi_{n\ell} \right\rangle , \qquad (4.1)$$

here the $\psi_{n\ell}$ is the eigenfunction of the non-relativistic Schrödinger equation (2.2). It is also shown in Appendix C that

$$\Delta_{n\ell} = -\frac{m}{16}\left(\frac{Z\alpha}{n}\right)^6 \frac{3n^3 - n\ell(\ell+1)}{(\ell+3/2)(\ell+1)(\ell+\frac{1}{2})\,\ell\,(\ell-\frac{1}{2})}\,. \tag{4.2}$$

The difference in energy splittings, predicted by the Klein-Gordon and Relativistic Schrödinger equations, of the transitions $(n_i, \ell_i = n_i - 1) \rightarrow (n_f, \ell_f = n_f - 1)$ and $(n_i, \ell_i' = n_i - 2) \rightarrow (n_f, \ell_f' = n_f - 2)$ is

$$D^6_{n_i - n_f} = (\Delta_{n_f\ell_f} - \Delta_{n_i\ell_i}) - (\Delta_{n_f\ell_f'} - \Delta_{n_i\ell_i'})\,. \tag{4.3}$$

$D^6_{n_i - n_f}$ for transitions of energy 40 - 60 keV as a function of the atomic number Z is plotted in Fig. 15.

The double commutator term in Eq. (4.1), called the Darwin term, is analogous to the zitterbewegung correction of the Dirac theory. Experimental verification of this term is as important as the observation of the Lamb shift(37) in an electronic atom. One way to verify this term is to measure the energy difference of the transitions $(n_i, \ell_i) \rightarrow (n_f, \ell_f)$ and $(n_i, \ell_i') \rightarrow (n_f, \ell_f')$ to sufficient accuracy to tell the difference between the predictions of the Klein-Gordon and Relativistic Schrödinger equations. Before this measurement becomes feasible great improvements in both theoretical calculation and experimental technique have to be achieved.

Let us choose the pionic Fe(Z = 26) 5-4 transitions as an example to discuss the improvements. The Darwin term contributes to the energy splitting by 0.17 eV. In order to verify the existence of this term

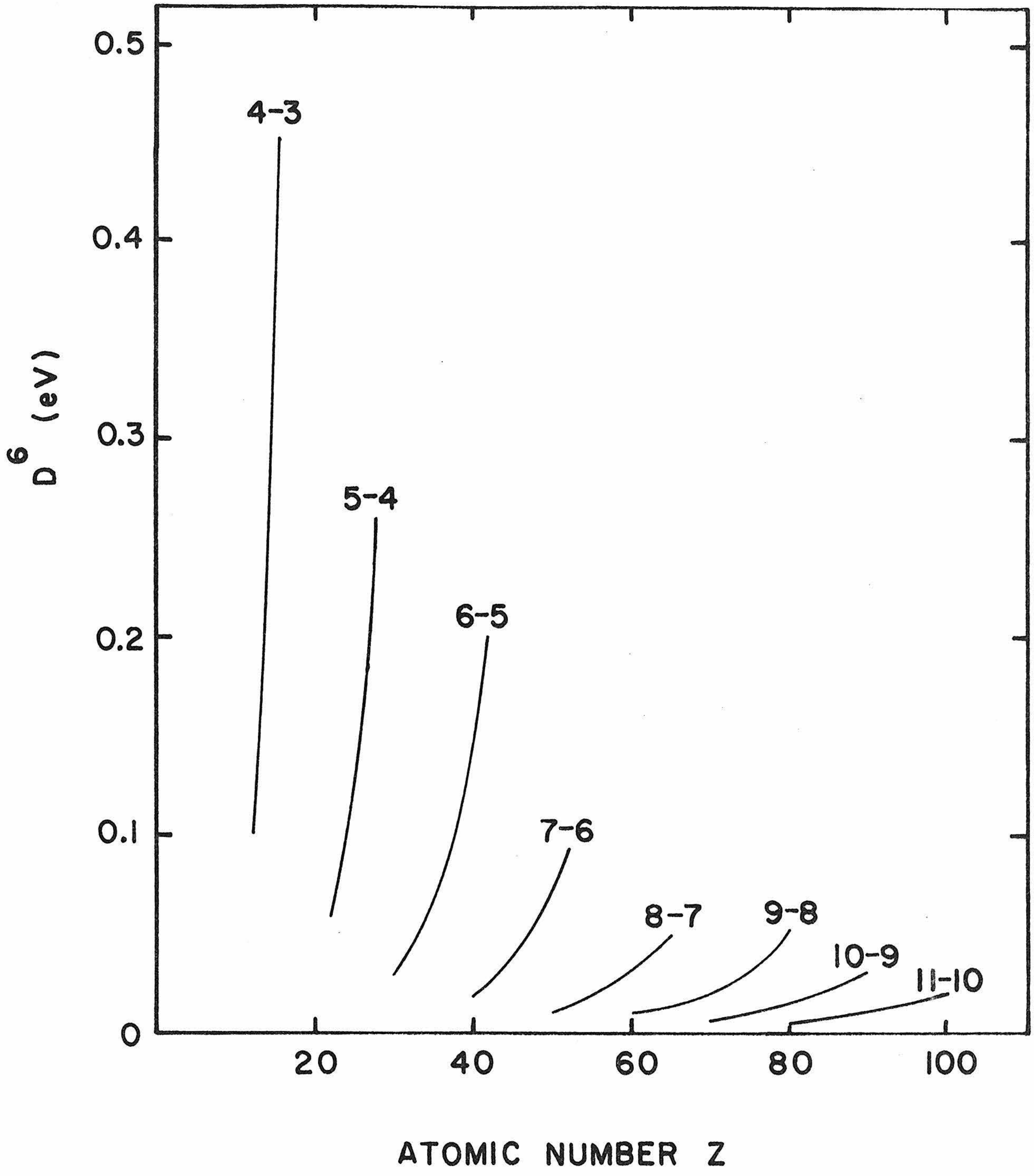

FIG. 15. Difference D^6 of energy splittings predicted by the Klein-Gordon equation and the Relativistic Schrödinger equation, to order $(\frac{Z\alpha}{n})^6$.

the uncertainties of the calculated and measured values of the energy splitting must be smaller than about 1/3 of the Darwin term contribution, say 0.05 eV, so that we will have a three-standard-deviation verification. Table 7 shows the calculated difference in energy of the pionic Fe 5g - 4f and 5f - 4d transitions according to the Klein-Gordon equation. The calculated energy splitting is 164.2 eV with an uncertainty of 1.3 eV which comes mainly from the uncertainty of the strong interaction correction. Our knowledge of the strong-interaction effect in pionic atoms is improving through new experimental data of the level shifts and broadenings.(38-40) We hope that someday one will be able to calculate the strong interaction correction in the energy splitting of the π^--Fe 5-4 transitions with accuracy better than 0.05 eV. There are three possible improvements in the experimental technique. (1) Increase the pion beam intensity. When the LAMPF accelerator runs with the full proton beam intensity 1 mA, it will provide 3 times more pions than it does now. (2) Improve the resolution of the crystal. It was shown by Sumbaev(27) that, by selecting a special direction to cut the quartz (310) crystal slab, the elastic quasi-mosaic spread could be minimized to 1.9 sec (of arc). The resolving power of the crystal, compared to that in the present experiment, can be increased by 5-6 times (with some sacrifice in efficiency). (3) Develop a position sensitive detector for x rays. The goal is to have a position resolution better than 0.15 mm. Then one does not need a slit. In this way one can measure the whole spectrum simultaneously, instead of measuring it step by step. This improvement will increase the counting time interval for each

TABLE 7. Calculated energy difference in the pionic Fe 5g-4f and 5f-4d transitions according to the Klein-Gordon equation.

	Difference in Energy (eV)
Coulomb	116.3
Vacuum Polarization	36.9
Strong Interaction	12.7[a]
Electron Screening	-1.7[b]
Total Splitting	164.2

[a] Calculated according to the optical-potential parameters given in Ref. 15. Uncertainty is about 10%.

[b] Assume screening of two 1s electrons.

position by a factor of about 20, compared with the present technique using a slit.

If the above mentioned improvements materialize, one will be able to verify experimentally the existence of the Darwin term of the Klein-Gordon equation for a spinless particle in a Coulomb field.

PART II

DEPENDENCE OF K X-RAY ENERGY UPON THE MODE OF EXCITATION

CHAPTER 5

INTRODUCTION

Atomic K x rays serve as an important and widely used energy-calibration standard as they are easily available and conveniently span the energy region up to 100 keV. The high resolution of a curved crystal spectrometer makes it possible to study a number of relatively small effects which, nevertheless, have to be taken into account when using atomic K x-ray standards. For example, the energy of a K x ray depends on the nuclear finite size and mass (isotope shift) and on the chemical composition of the source (chemical shift).(41) Besides these well studied and understood effects, the energy of a K x ray may also depend on the method of excitation. We have investigated(42-44) this problem for the commonly used excitation modes: fluorescence, electron capture, and internal conversion, for K x rays in Ta, Eu, Lu, Tm, and W. Several mechanisms contributing to the difference in K x-ray energy between these modes of excitation were established. We also found unexpectedly that the energies of the K x rays in Ta vary by as much as 1 eV. This large shift is not yet theoretically understood.

Similar work on W $K\alpha_1$ x ray was done earlier by Beer and Kern,(45) and by Borchert.(46) Recently, systematic studies of the K x-ray shifts have been carried out by us and by Borchert *et al.*(47-49) The results show that the energies of K x rays indeed depend, to a certain degree, on the mode of excitation.

It should be stressed that the use of K x rays as an energy standard is only part of the motivation of our study. Indeed, the quantal description of inner atomic shells is very accurate. The small effects in K x-ray energies are manifestations of important physical phenomena. Thus, for example, the measurement of the isotope shift is a useful tool for determining nuclear sizes; the measurement of the chemical shift helps to determine which of the valence electrons participate in chemical bonds. The study of x-ray energy shifts will help, in the end, not only to provide a better energy standard but also to understand the interplay of nuclear, atomic, chemical, and solid state phenomena.

In this thesis we present a complete description of our experimental procedure (Chapter 6) and the results (Chapter 7). The known effects contributing to the x-ray shifts and further planned experimental work are discussed in Chapter 8.

CHAPTER 6

EXPERIMENTAL METHOD

The experimental setup, the x-ray sources, data acquisition and analysis are discussed in this chapter.

6.1 Experimental Setup

The experimental setup is shown schematically in Fig. 16. The Caltech-LAMPF bent-crystal spectrometer, used for this measurement, has been described in Ref. 8. Here a smaller quartz (310) crystal than that of Part I was used. It is 1.5 mm thick and has an aperture 5 cm wide x 4 cm high. The bending radius of the crystal is 198.5 cm. The width of the 17 cm long curved slit was chosen to be 0.2 mm. The spectrometer has a total resolution of 93 eV FWHM at 60 keV, and 41 eV at 40 keV.

The x-ray sources were mounted on a wheel and could be turned into position in a sequential manner with the help of a stepping motor. The wheel could hold four sources at one time. Each source was continuously rotated about its own axis to smooth out the azimuthal variation of the source distribution. The collimator had an aperture of 0.95 cm, which is smaller than the size of the x-ray sources (see Sec. 6.2). The collimator thus precisely defines the active source position for different sources. The spectrometer control and data acquisition system will be discussed in Sec. 6.3.

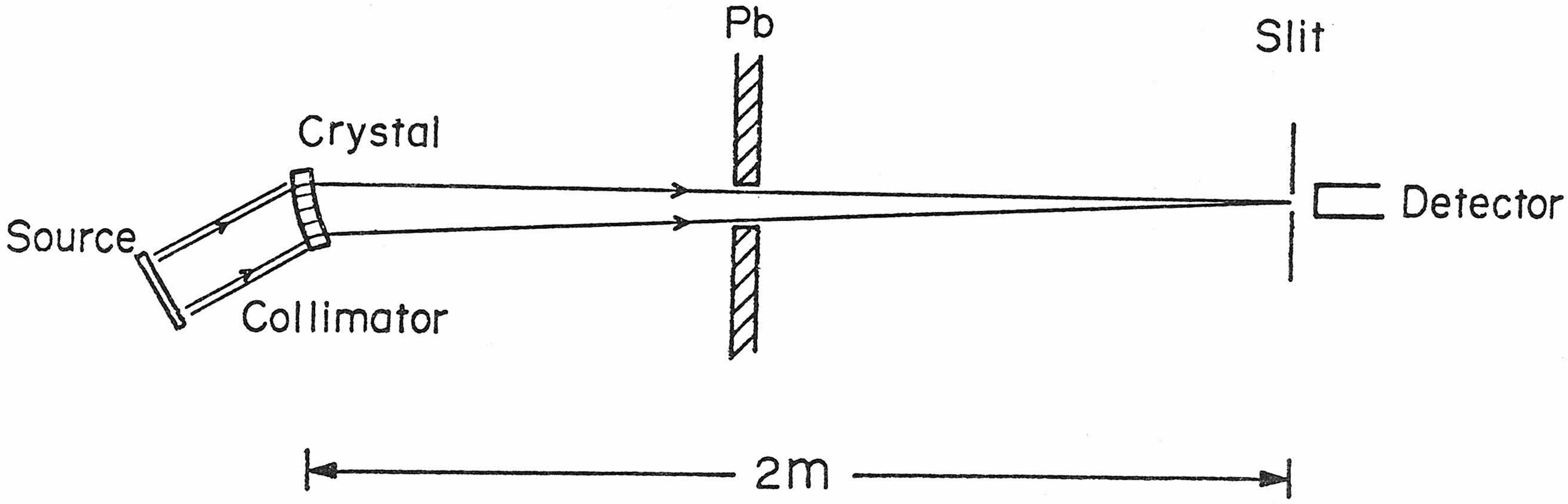

FIG. 16. Diagram of setup. (The drawing is not to scale.)

6.2 X-Ray Sources

The radioactive sources used in this experiment were prepared by thermal neutron irradiation. To make a source ^{A}Z, the enriched isotope ^{A-1}Z was distributed uniformly in a capsule made of 99.99% pure aluminum. The two parts of the capsule were then press-fitted and welded together (see Fig. 17). The loaded capsule was irradiated by thermal neutrons, with a flux of 2.5×10^{14} n/cm^{2}sec, for 75-300 hours. The preparation and usage of the sources are listed in Table 8. The dimensions of the sources and fluorescence targets are shown in Fig. 17. The fluorescence (fℓ) x rays in Ta, Lu, Tm, and W were emitted from targets irradiated by $^{153}Gd_2O_3$ sources,(except in run 1, discussed in Sec. 7.1, where the radioactivity of $^{182}Ta_2O_5$ excites the Ta atoms in the source to generate Ta fℓ x rays), and those in Eu were emitted from targets irradiated by $^{169}Yb_2O_3$. The electron-capture (EC) or internal conversion (IC) x rays were emitted from the sources themselves. The partial decay schemes, deduced from information given in Refs. 50 and 51, of these sources are shown in Figs. 18-22 and are discussed below.

The EC x rays of Ta are emitted from ^{181}W and $^{181}WO_3$ sources, due to the refilling of K vacancies generated after electron capture. The IC x rays of Ta are emitted from a $^{181}HfO_2$ source. The radioactive nucleus ^{181}Hf β-decays to the excited states of ^{181}Ta. Several γ-transitions in the final nucleus ^{181}Ta have a large probability for K-electron internal conversion. Those transitions are shown by thick arrows in the partial decay scheme of ^{181}Hf (Fig. 19). The transition energy, the transition mode, and the relative yield of the ejected K electrons are

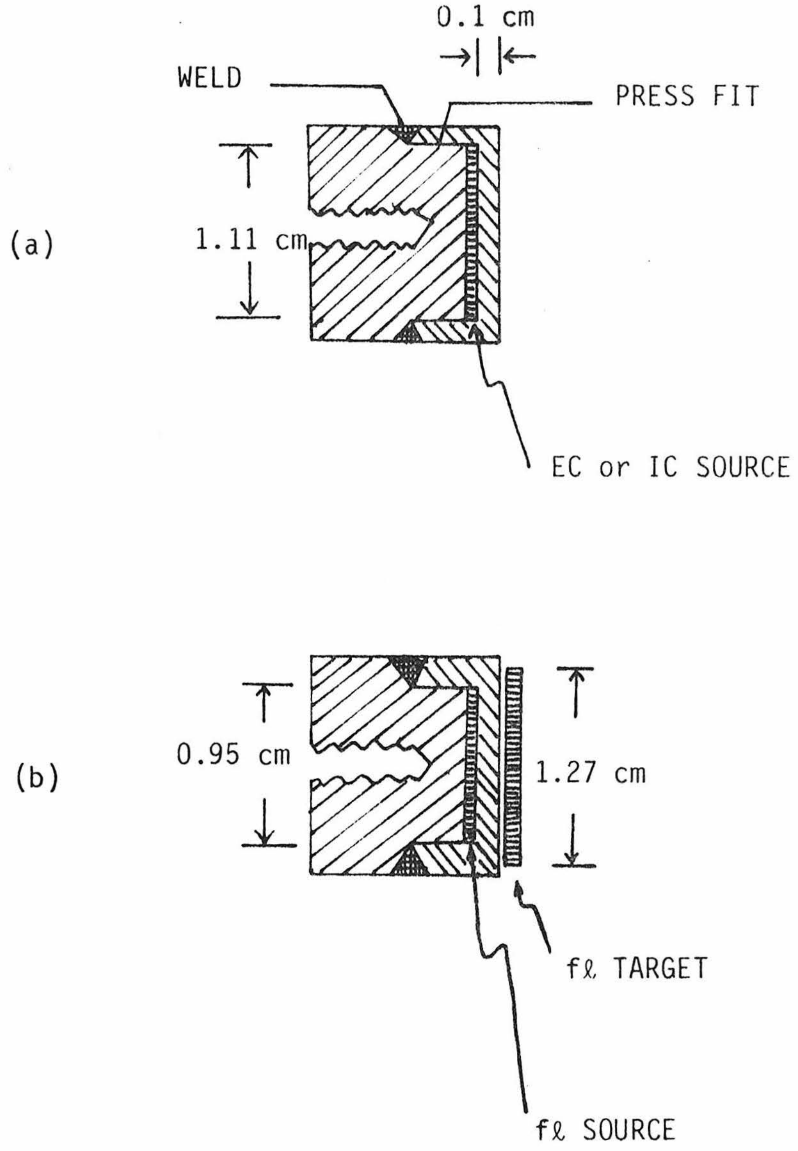

FIG. 17. Configurations of the x-ray sources for (a) electron capture or internal conversion, and (b) fluorescence.

TABLE 8. The preparation and usage of the radioactive sources used in this experiment.

Source	Preparation				Usage
	mass (mg)	enrichment (%)	material	irradiation time[a] (hr)	
^{181}W	50	6.93	^{180}W	293	Ta(EC) x rays
$^{181}WO_3$	63	6.93	$^{180}WO_3$	293	Ta(EC) x rays
$^{153}Gd_2O_3$	92	13.26	$^{152}Gd_2O_3$	293	(1) To fluoresce Ta,Lu,Tm, and W targets. (2) Eu(EC+IC) x rays.
$^{181}HfO_2$	50	94	$^{180}HfO_2$	218	Ta(IC) x rays
$^{169}Yb_2O_3$	4	13.4	$^{168}Yb_2O_3$	96	To fluoresce Eu targets.
$^{175}HfO_2$	6.7	6.7	$^{174}HfO_2$	96	Lu(EC+IC) x rays
^{182}Ta	20	100	^{181}Ta	260	W(IC) x rays
$^{182}Ta_2O_5$	20	100	$^{181}Ta_2O_5$	260	W(IC) x rays

[a] The flux was 2.5×10^{14} n/cm^{2}sec.

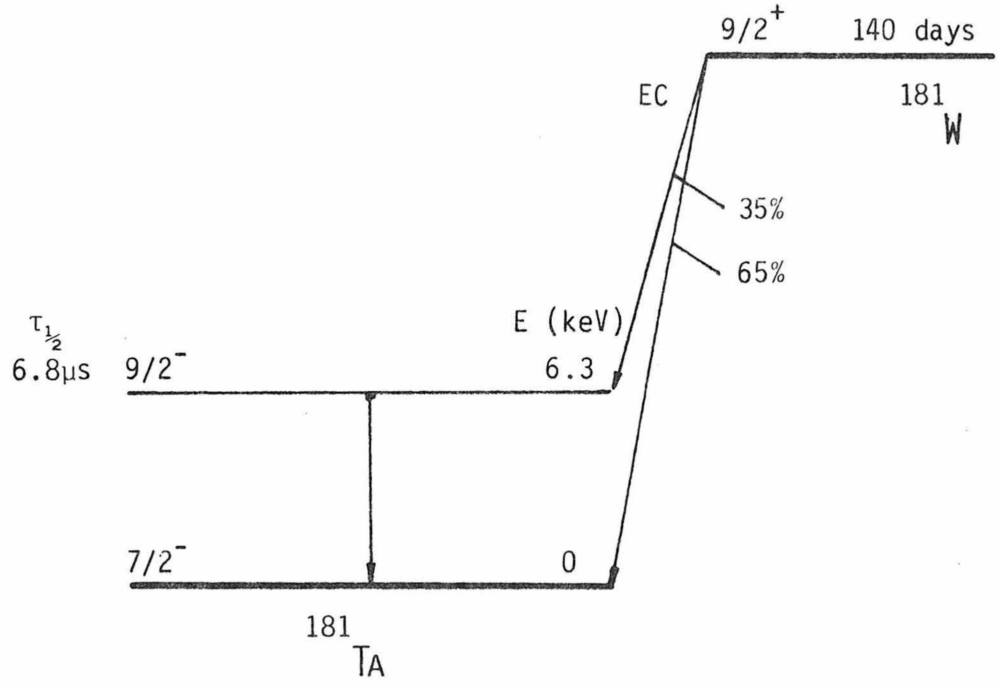

FIG. 18. Partial decay scheme of ^{181}W.

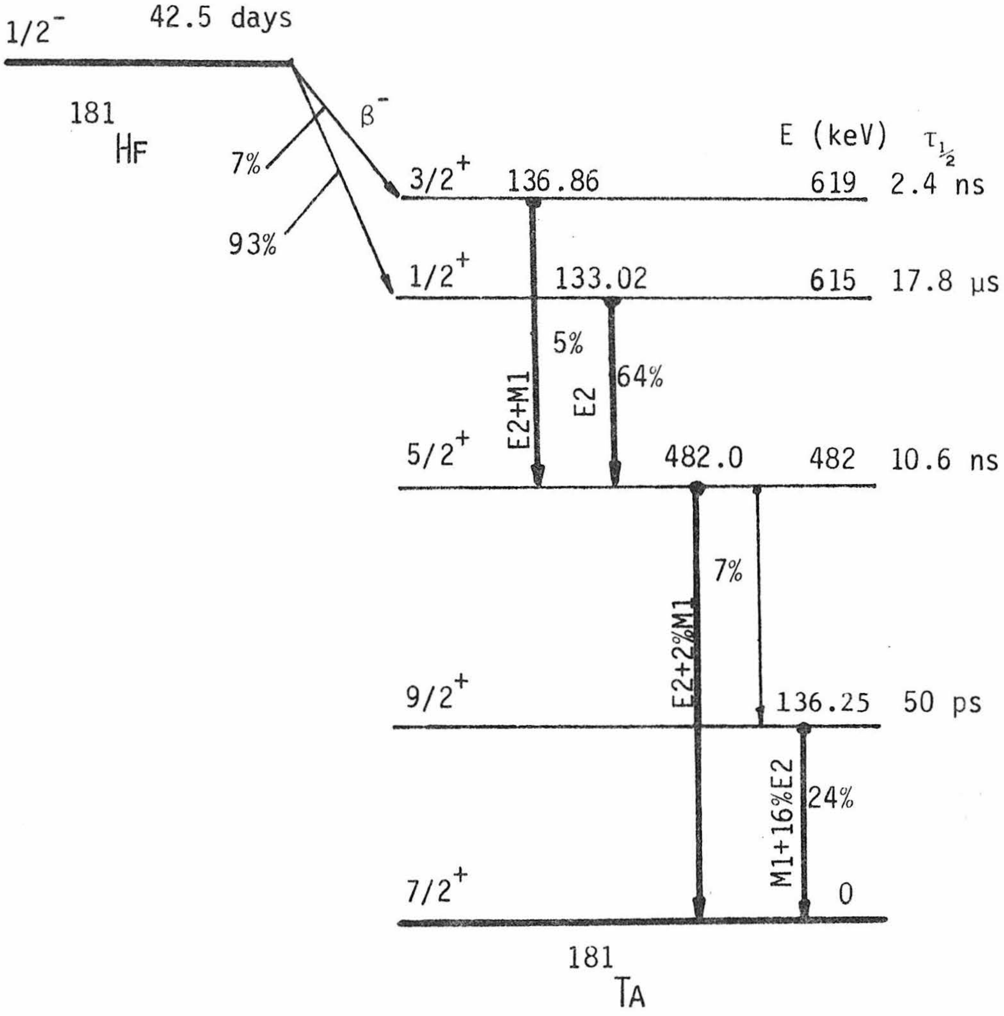

FIG. 19. Partial decay scheme of ^{181}Hf.

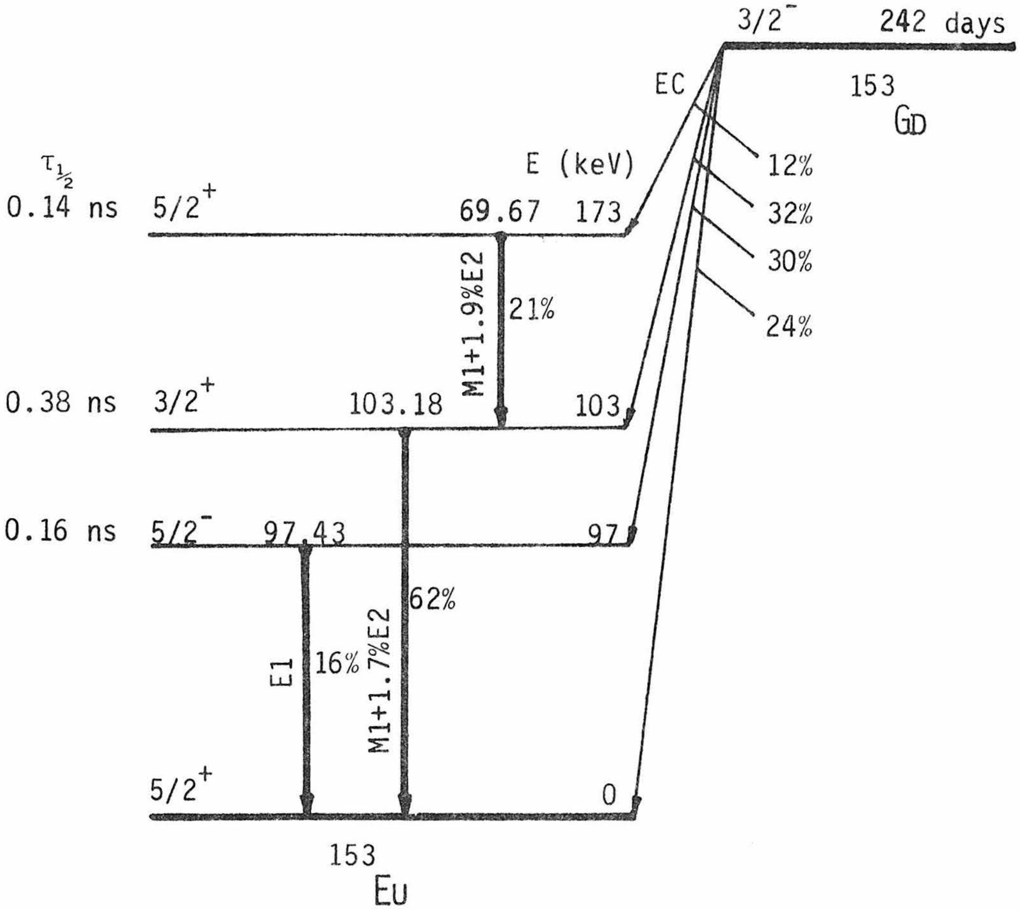

FIG. 20. Partial decay scheme of ^{153}Gd.

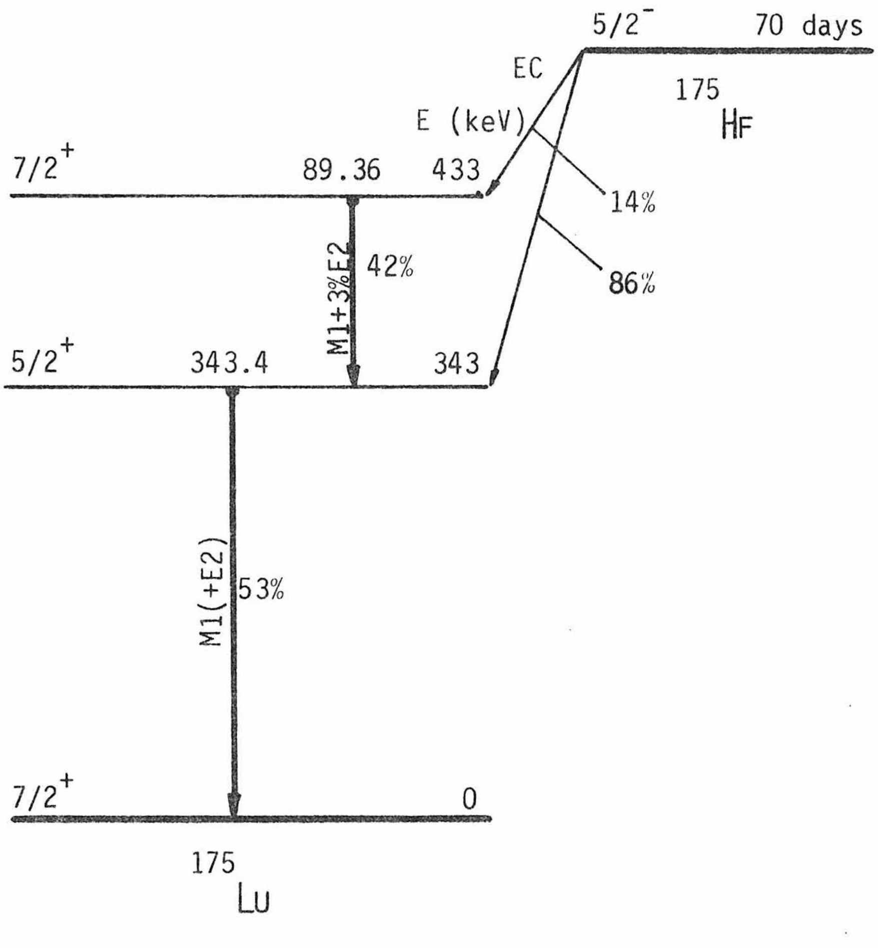

FIG. 21. Partial decay scheme of ^{175}Hf.

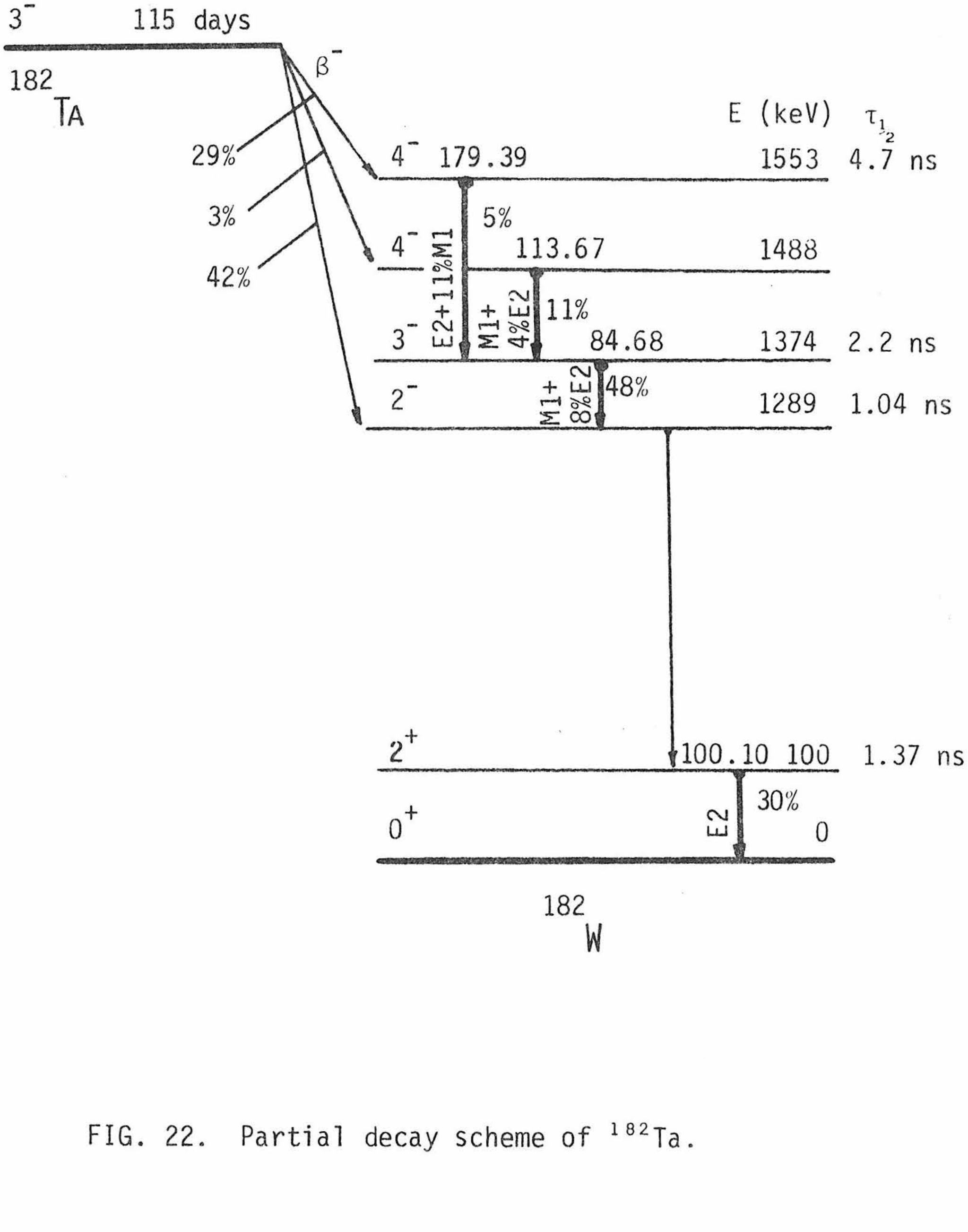

FIG. 22. Partial decay scheme of ^{182}Ta.

given on the top, left, and right sides of each thick arrow respectively. After each internal conversion the IC x rays are emitted in about 10^{-17} sec, much before the next γ-transition takes place, since the life time of the related excited state in ^{181}Ta is longer than 10^{-11}sec.

The $^{153}Gd_2O_3$ source emits both EC and IC x rays of Eu. The EC x rays are emitted immediately following each electron capture (in $\sim 10^{-17}$ sec). After about 10^{-10} sec the internal conversion may occur and IC x rays may be emitted. From the information provided in Ref. 50 we deduced that 68% of the Eu x rays out of a ^{153}Gd source were related to EC and 32% were related to IC.

The EC and IC x rays of Lu are emitted from a $^{175}HfO_2$ source in a similar way as Eu x rays from $^{153}Gd_2O_3$. One has 86% EC x rays and 14% IC x rays.

The IC x rays of W are emitted from a $^{182}Ta_2O_5$(or ^{182}Ta) source similar to the Ta x rays emitted from a $^{181}HfO_2$ source. The partial decay scheme of ^{182}Ta is shown in Fig. 22. The four transitions indicated by thick arrows have non-negligible probabilities of internal conversion.

6.3 Data Acquisition

In the pionic fine-structure splitting experiment reported in Part I, we measured the energy difference of two x rays emitted from the same source (the Ti target). The splitting we measured is about three times larger than the spectrometer resolution. In the present experiment we were measuring the energy difference of x rays emitted from different sources and the shift we were looking for was only about

1/100 of the spectrometer resolution. Therefore, systematics errors had to be eliminated with great care. Instead of scanning one x-ray line from one source at a time, we undertook the following data acquisition procedure.

The x rays emitted from the four sources A, B, C, and D were compared almost simultaneously. The x-ray line was scanned in steps of 0.05 mÅ. One scan consisted of 25 steps for $K\alpha_1$ or $K\alpha_2$ lines, and 41 steps for $K\beta_{1,3}$ lines. Since $K\beta_1$ and $K\beta_3$ lines are close to each other, they were measured in the same scan. In the beginning (the first spectrometer position of the first scan) the x rays from source A were detected by the GE detectors and were counted for a counting period (which depends on the source strength). Then the sample wheel was turned to bring source B into position. After all the sources had been measured, we returned to the source A for another measurement before we moved the spectrometer to the next position. At the second position we measured sources B, C, D, A, and B. This went on until we measured A, B, C, D, and A at the last position of the scan. Then the spectrometer was moved to position 1 for scan 2 starting with source B. After four scans we completed one cycle, which we called a "data unit".

The spectrometer control and data acquisition system is shown in Fig. 23. Detectors #1 and #2 were coupled together as the top channel and detectors #3 and #4 were coupled as the bottom channel. Each channel had an energy resolution of 2 keV FWHM at 40-60 keV. The window

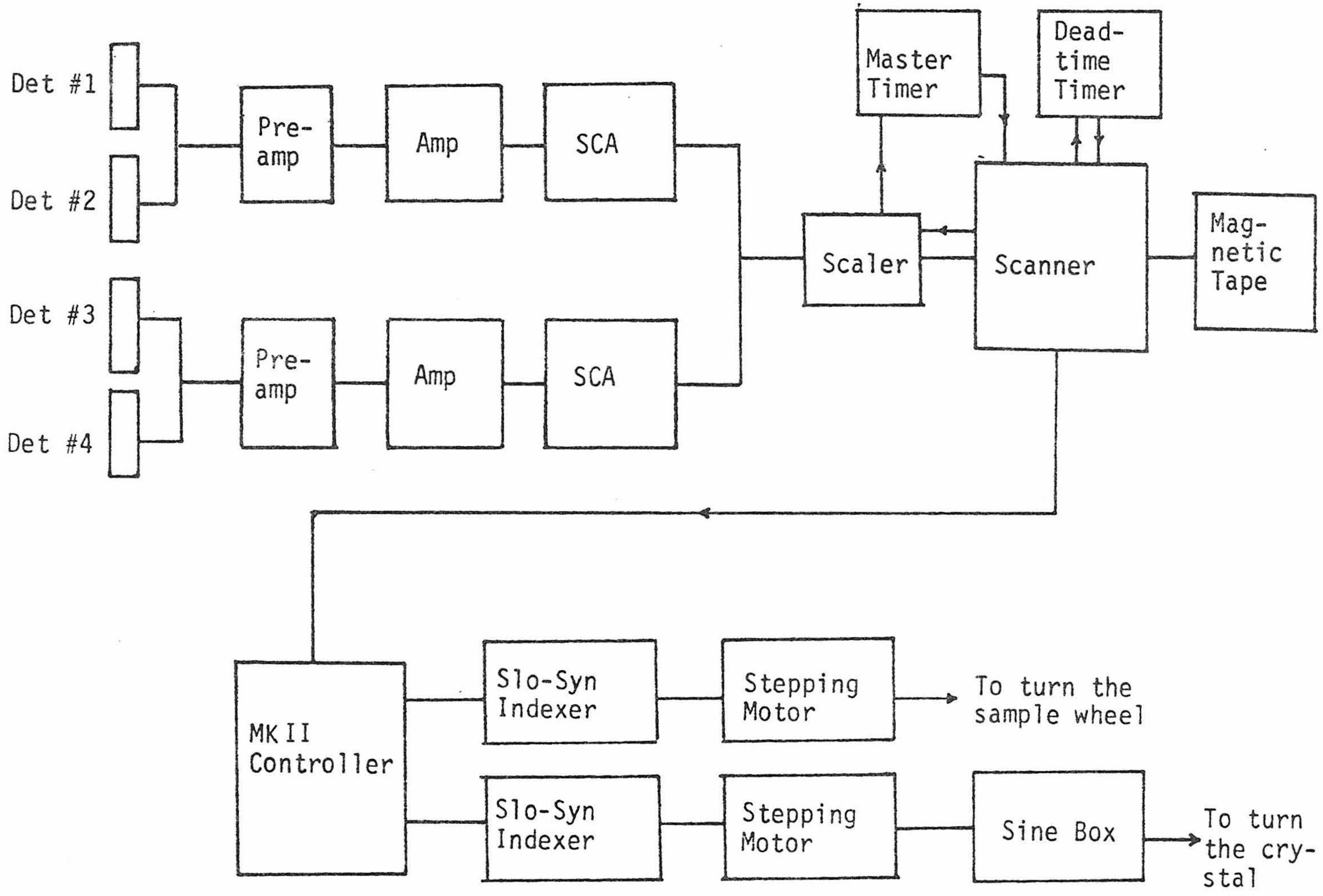

FIG. 23. Spectrometer control and data acquisition system.

of the single channel analyzer (SCA) was set to be ± 2 keV around the energy of the x rays under investigation. At the end of each counting period, the number of counts in the scaler was recorded on a magnetic tape through the scanner. The scanner then sent a signal to the home-made MKII controller which controlled the crystal and the sample wheel with the help of two stepping motors.

6.4 Data Analysis

The raw data, stored on the magnetic tape, were computer analyzed every three to four days. For each data unit, the computer summed the counts belonging to each source at the same position to form an x-ray profile. For Kα x-ray lines, this profile was fitted to a Gaussian function above a linear background,

$$f(i) = B_0 + B_1 i + A \exp\left[- \frac{4 \ln 2 (i - c)^2}{\Gamma^2} \right] , \qquad (6.1)$$

by a least-squares program. The variable parameters were the elevation B_0 and the slope B_1 of the background, the amplitude A, the centroid c, and the width Γ. Fig. 24 shows two typical profiles from one data unit of a Ta Kα_1 measurement and their least-squares fits. The profile of the K$\beta_{1,3}$ lines was fitted to the sum of two Gaussian functions above a linear background.

The line shifts s_j between any two samples and its error σ_{s_j} were computed from the differences of the fitted centroids and errors in the j^{th} data unit. The weighed mean $\bar{s}$ of the shifts from all the data

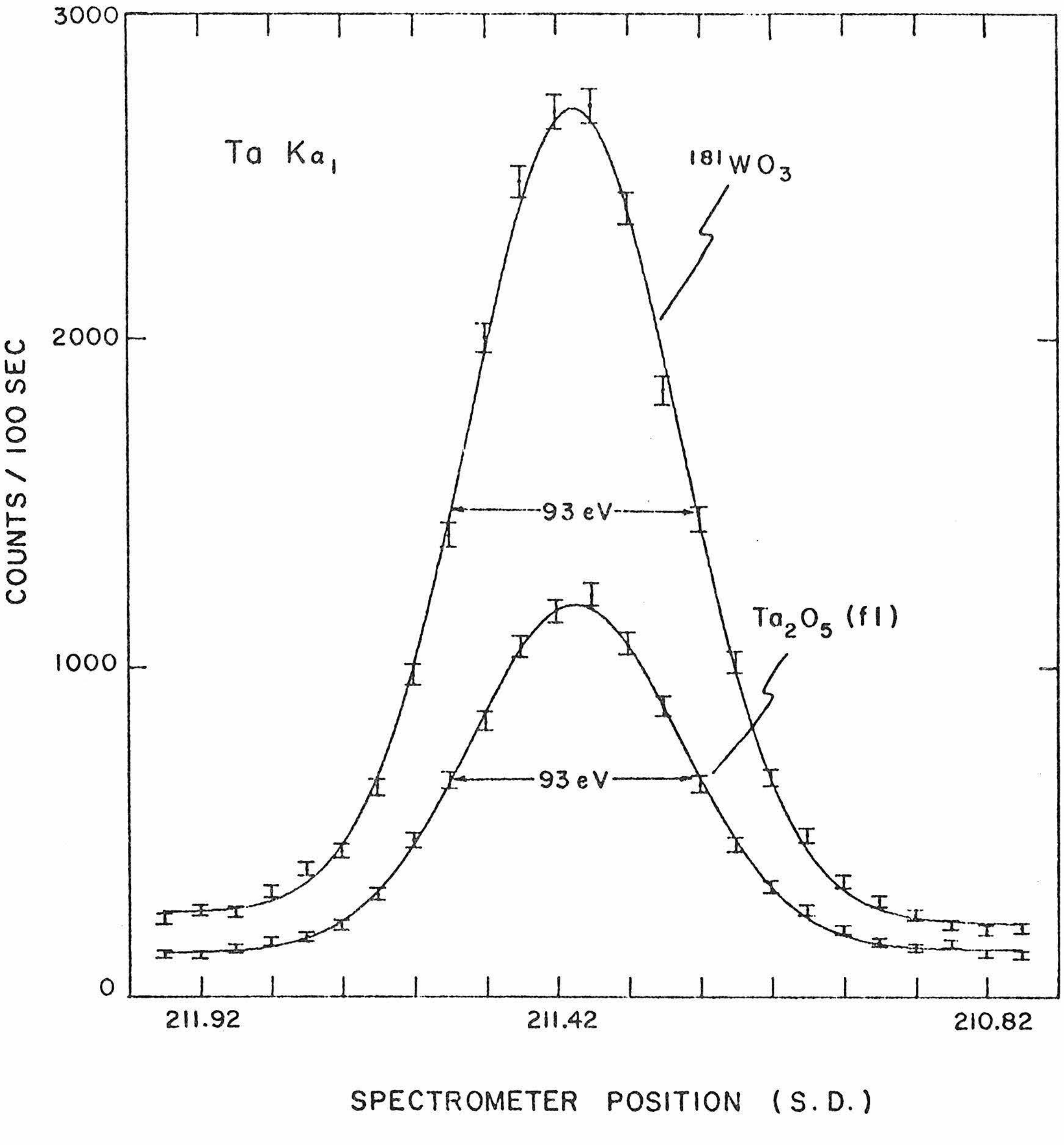

FIG. 24. The spectra of Ta Kα_1 x rays from $^{181}WO_3$ and Ta_2O_5(fℓ). Solid lines represent least-squares fits, with χ^2's per degree of freedom 1.5 and 0.7 for $^{181}WO_3$ and Ta_2O_5(fℓ) lines respectively.

units were calculated. The internal error

$$\sigma_{\bar{s}} = \frac{1}{\sqrt{\sum_j \frac{1}{(\sigma_{s_j})^2}}} \qquad (6.2)$$

and the external error

$$\sigma'_{\bar{s}} = \sqrt{\frac{1}{N(N-1)} \sum_j (s_j - \bar{s})^2} \qquad (6.3)$$

were also calculated and compared. The comparison of these two errors provided a check of the statistical consistency of our data. The larger one of them was assigned as the error of $\bar{s}$.

CHAPTER 7

RESULTS

The experimentally determined K x-ray energy shifts in Ta, Eu, Lu, Tm, and W are reported in this chapter. Comparisons with other available results are presented.

7.1 Ta X Rays

Five different runs were undertaken to measure the Ta $K\alpha_1$ x-ray shift between $^{181}WO_3$ and $Ta_2O_5(f\ell)$ samples. The results are shown in Table 9. Run 1 is our first measurement of the x-ray energy shift for different excitation modes.(42) The tantalum oxide $^{182}Ta_2O_5$ was used as a fluorescence source. Ta atoms in the source were excited by the radioactivity of their neighboring unstable nuclei ^{182}Ta. In runs 2-5 the Ta_2O_5 target (300 mg/m^2) was irradiated by the strong γ rays of 97 and 103 keV from a $^{153}Gd_2O_3$ source. Runs 2-5 were separated in time by several months while x-ray shifts of other lines were studied. In run 5 a NaI detector was used instead of the GE detectors. We plotted the results of these five runs in Fig. 25 to show that the large shift in Ta $K\alpha_1$ x rays emitted from $^{181}WO_3$ compared to those produced by fluorescence was well confirmed.

Besides the oxide samples mentioned above, the EC and $f\ell$ K x rays of Ta from four sources, ^{181}W, ^{181}WO , Ta metal (300 mg/cm^2), and Ta_2O_5 (300 mg/cm^2) were compared. A summary of the results is presented in Table 10, lines 1-4. Lines 3 and 4 represent the chemical

TABLE 9. Experimental results of Ta $K\alpha_1$ x-ray shift between $^{181}WO_3$ and $Ta_2O_5(f\ell)$ from different runs.

Run No.	$E_{^{181}WO_3} - E_{Ta_2O_5(f\ell)}$
1	-0.67(0.13)
2	-0.78(0.07)
3	-0.81(0.14)
4	-1.04(0.24)
5	-0.59(0.25)
Mean	-0.77(0.05)

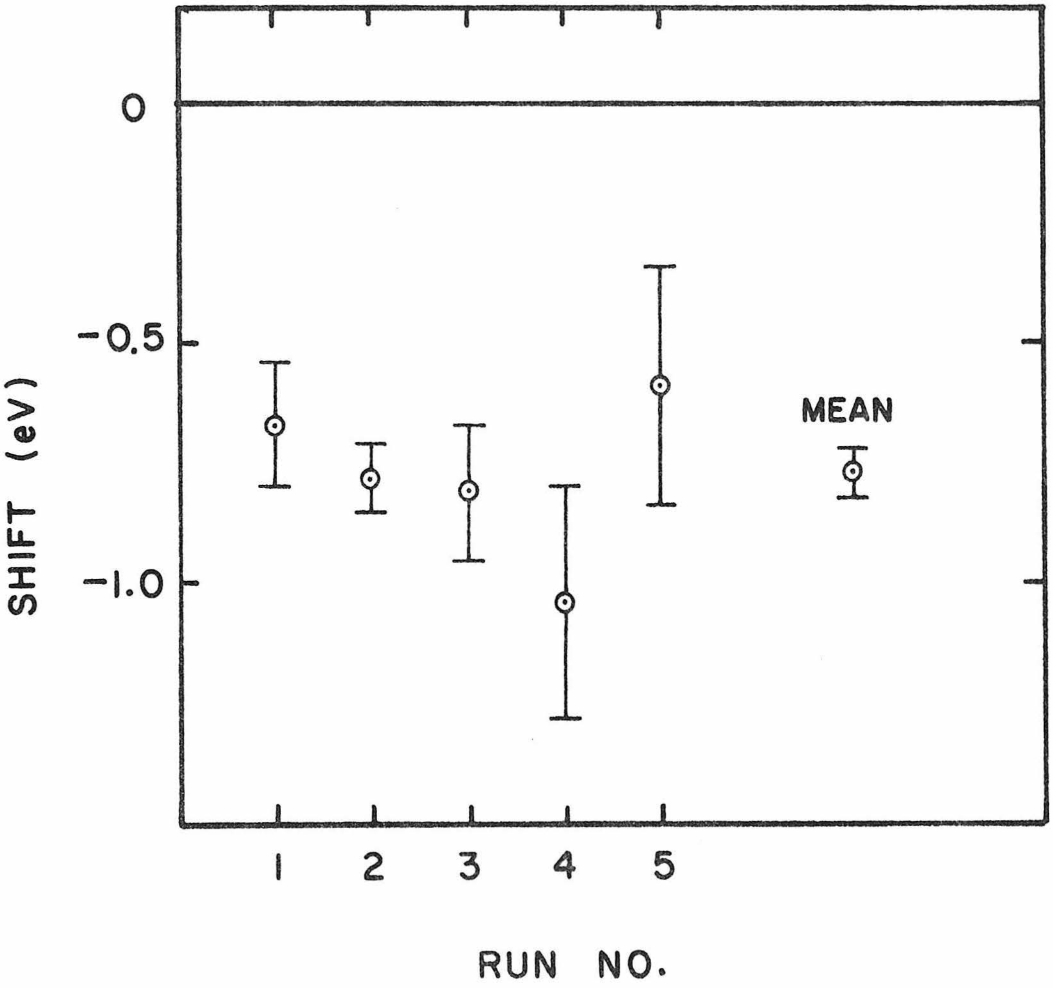

FIG. 25. Experimental results of Ta Kα_1 shift $^{181}WO_3$-Ta_2O_5(fℓ) from different runs.

TABLE 10. Experimental results of the K x-ray energy shifts.

	X Ray Emitting Source		$E_A - E_B$(eV)			
	A	B	$K\alpha_1$	$K\alpha_2$	$K\beta_1$	$K\beta_3$
Ta K X Rays	^{181}WO	$Ta_2O_5{}^a$	-0.77(0.05)	-0.81(0.07)	-1.13(0.14)	-0.56(0.24)
	^{181}W	Ta^a	-0.81(0.08)	-0.94(0.30)	-1.03(0.22)	-0.53(0.39)
	^{181}W	$^{181}WO_3$	0.07(0.06)	-0.02(0.24)	0.10(0.23)	-0.09(0.36)
	Ta^a	$Ta_2O_5{}^a$	0.10(0.08)	-0.00(0.34)	-0.03(0.24)	-0.78(0.42)
	^{181}W	$^{181}HfO_2$	-1.27(0.12)	-	-2.98(0.58)	-
	$^{181}WO_3$	$^{181}HfO_2$	-1.48(0.12)	-	-2.17(0.59)	-
	$Ta_2O_5{}^a$	$^{181}HfO_2$	-0.70(0.11)	-	-	-
	$^{181}HfO_2$	$^{181}HfO_2$	0.07(0.10)	-	-0.32(0.35)	-
Eu K X Rays	$^{153}Gd_2O_3$	$Eu_2O_3{}^b$	0.09(0.05)	0.11(0.06)	0.60(0.06)	0.89(0.10)
	$^{153}Gd_2O_3$	Eu^b	-0.63(0.03)		-0.86(0.30)	-0.14(0.50)
	$^{153}Gd_2O_3$	$^{153}Gd_2O_3$	0.03(0.02)	-	-	-
Lu K X Rays	$^{175}HfO_2$	$Lu_2O_3{}^a$	-0.43(0.10)	-0.39(0.17)	-0.20(0.29)	-0.67(0.53)
Tm K X Rays	$Tm_2O_3{}^c$	$Tm_2O_3{}^a$	0.05(0.11)	-	-	-
W K X Rays	W^a	$WO_3{}^a$	0.04(0.20)	-	-	-
	^{182}Ta	$^{182}Ta_2O_5$	0.03(0.08)	-	-	-
	W^a	^{182}Ta	-0.58(0.17)	-	-	-
	$WO_3{}^a$	$^{182}Ta_2O_5$	-0.31(0.08)	-	-	-

[a] Fluoresced by $^{153}Gd_2O_3$ source, (97.43 and 103.18 keV γ rays).

[b] Fluoresced by $^{169}Yb_2O_3$ source, (63.12 keV γ ray).

[c] Fluoresced by ^{241}Am source, (59.54 keV γ ray).

shifts of Ta K x rays. Our measured chemical shifts of Ta $K\alpha_1$ x rays, 0.07(0.06) eV from W-WO_3 and 0.10 (0.08) eV from Ta-Ta_2O_5 agree within the errors with the result of Sumbaev *et al.*(52), which is 0.11(0.03) eV.

Two runs with the IC x rays were taken, each involving a set of four sources. The first set contained ^{181}W, $^{181}WO_3$, Ta_2O_5(fℓ) and $^{181}HfO_2$ and the second set contained ^{181}W, $^{181}WO_3$, $^{181}HfO_2$, and $^{181}HfO_2$. The results of these two runs are listed in lines 5-8 of Table 10. As can be seen, there is a large energy shift in Ta K x rays between ^{181}WO and $^{181}HfO_2$. For Ta_2O_5(fℓ) - $^{181}HfO_2$ we observed a shift of the same magnitude and sign as for $^{181}WO_3$ - Ta_2O_5(fℓ). The result of $^{181}HfO_2$ - $^{181}HfO_2$ in line 8 provided a null test of the experiment.

7.2 Eu X Rays

We have examined the energies of the Eu K x rays emitted after EC in ^{153}Gd and compared them to the fluorescent K x rays. The fluorescence samples consisted of Eu metal (200 mg/cm^2) as well as Eu_2O_3(200 mg/cm^2) backed by a 3-Ci source of $^{169}Yb_2O_3$.

In the measurement of Eu K x-ray shifts we compared two samples at one time. The results are shown in Table 10. We can calculate the chemical shifts (Eu-Eu_2O_3) from the first two entries of the Eu results, and compare them with the results of Smirnov *et al.*(53) (Table 11). The measured shifts between $^{153}Gd_2O_3$ and Eu_2O_3(fℓ) will be discussed in Chapter 8. The third entry of the Eu results represents a null test.

TABLE 11. Chemical shift of the Eu K x rays $E_{Eu(metal)} - E_{Eu_2O_3}$ (in eV).

Lines	This work	Smirnov *et al*[a]
$K\alpha_1$	0.72(0.06)	0.644(0.011)
$K\alpha_2$	—	0.582(0.015)
$K\beta_1$	1.46(0.31)	1.450(0.040)
$K\beta_3$	1.03(0.51)	1.730(0.050)

[a] Ref. 53.

7.3 Lu X Rays

In a similar fashion we compared the Lu K x rays associated with electron capture of ^{175}Hf with the Lu fluorescent K x rays. Fluorescent x rays were produced in a Lu_2O_3 sample (300 mg/cm^2) with the help of the ^{153}Gd source. The results are shown in Table 10.

7.4 Tm X Rays

As a further test, the Tm $K\alpha_1$ x-ray energy shift was measured for two fluorescent Tm samples excited with γ rays of different energies. One sample was excited by the ^{241}Am γ ray (59.54 keV) and the other one by the ^{153}Gd γ rays (97 and 103 keV). The ^{241}Am γ ray is only 150 eV above the K edge of Tm. The ejected electron will still be in the immediate vicinity of the atom when the x ray is emitted since the half life of the K hole is about 10^{-17}sec. The results are given in Table 10. No difference in energy is seen between the two situations. Our results may be compared with the results of Ref. 54, which showed that the differences between the L_I and K internal conversion electron lines in ^{241}Am are constant within 5 eV for electron energies between 7 and 450 keV.

7.5 W X Rays

Two measurements have been carried out to compare the W $K\alpha_1$ x rays emitted from ^{182}Ta (metal), $^{182}Ta_2O_5$, W(fℓ) and WO_3(fℓ). The fluorescent W K x rays were emitted from a W foil (290 mg/cm^2) and four WO_3 targets (250 mg/cm^2 or 315 mg/cm^2) excited by $^{153}Gd_2O_3$. A summary of the results is presented in Table 10. The shifts of W-WO_3 and Ta-Ta_2O_5 agree with the chemical shift of W $K\alpha_1$, 0.11(0.03) eV, measured by Sumbaev *et al.*(52) The mean of the shifts W-Ta and WO_3-Ta_2O_5, -0.36(0.07) eV, should be compared with the results of Beer and Kern(45), -1.8(0.5) eV, and Borchert(46), 0.10(0.22) eV, as shown in Fig. 26.

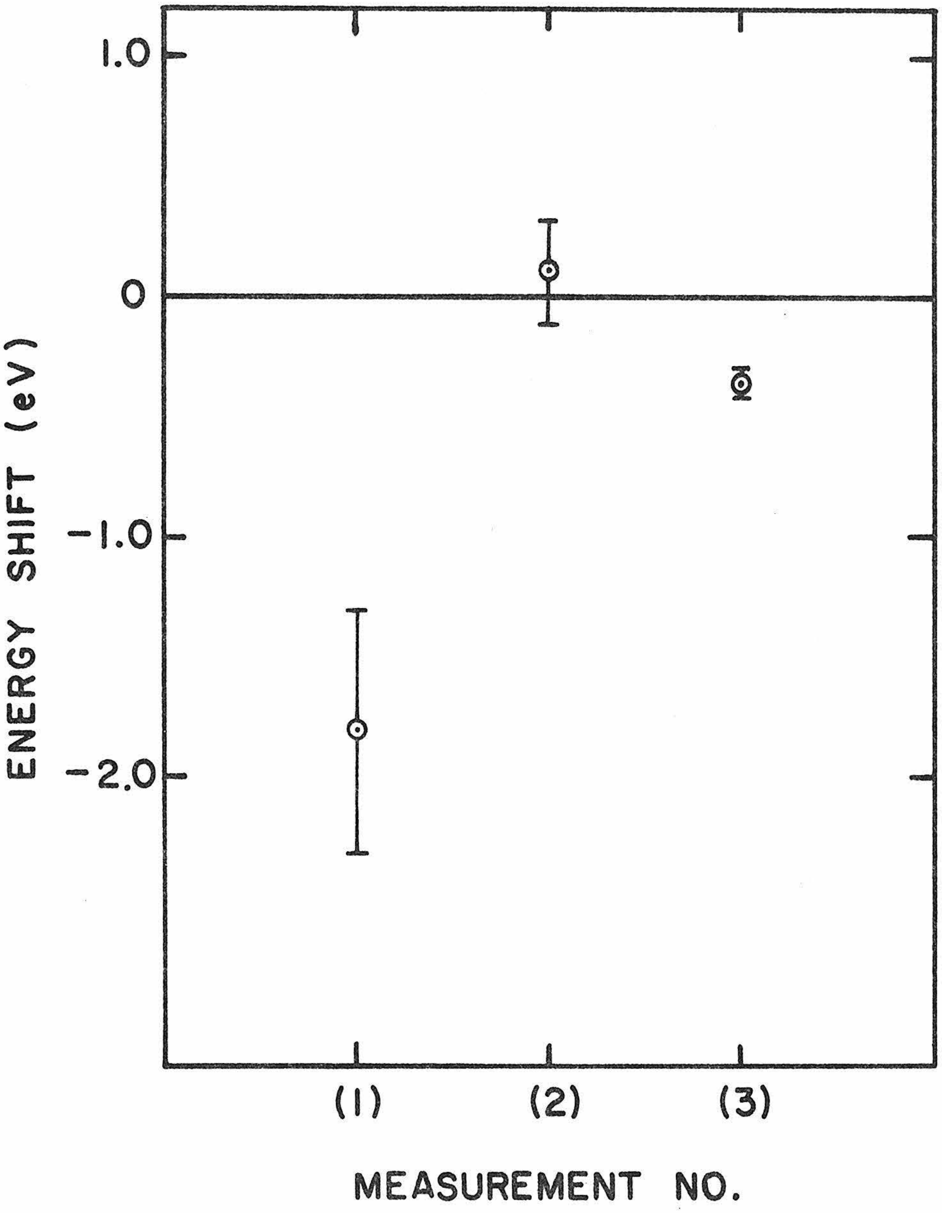

FIG. 26. Measured energy shifts of W Kα_1 x rays, $E_{f\ell}$-E_{IC}, by (1) Beer and Kern, (2) Borchert, and (3) present work.

CHAPTER 8

DISCUSSION

In this chapter we discuss the mechanisms which should be considered in an attempt to understand the observed energy differences. We then compare the measured shifts with the sum of the various non-negligible contributions. Further experimental work is also described.

8.1 Magnetic Hyperfine Interaction

Before a K x ray can be emitted, a 1s vacancy has to be created by fluorescence, internal conversion, or electron capture, etc. If the nucleus has a nonzero spin, the remaining 1s electron may be in one of the two hyperfine states, due to the coupling of its spin $\vec{S}_e (= \vec{\tfrac{1}{2}})$ with the spin of the nucleus $\vec{I}_f$. The energies of the two hyperfine states are shifted by

$$\Delta\varepsilon = A\,\vec{I}_f \cdot \vec{S}_e = \begin{cases} \frac{A}{2} I_f & \text{if } F = I_f + \frac{1}{2} \\ -\frac{A}{2}(I_f + 1) & \text{if } F = I_f - \frac{1}{2} \end{cases} \tag{8.1}$$

where $\vec{F} = \vec{I}_f + \vec{S}_e$, and A is the magnetic hyperfine interaction constant. For A we use the expression(55,56)

$$A = \frac{4}{3I_f}\frac{\mu}{\mu_B}\,\alpha\, m_e c^2 \frac{(Z\alpha)^3}{\Omega(2\Omega - 1)} \tag{8.2}$$

where μ is the nuclear magnetic moment, μ_B is the Bohr magneton, and $\Omega = \sqrt{1-(Z\alpha)^2}$. Let P(F) be the population of the hyperfine component with a total angular momentum F, then the energy of the observed K x-ray line is shifted by

$$\Delta E = \frac{A}{2}\,[I_f\,P(I_f + \tfrac{1}{2}) - (I_f + 1)\;P(I_f - \tfrac{1}{2})]. \tag{8.3}$$

For a nuclear transition of multipolarity $\vec{\lambda}$ (electron capture or internal conversion) from an initial nuclear state of spin $\vec{I}_i$ to a final nuclear state of spin $\vec{I}_f$, where the angular momentum of the ejected fermion (a neutrino for electron capture or an electron for internal conversion) is $\vec{S}$, one obtains

$$P(F) = (2\lambda + 1)\;(2F + 1)\begin{Bmatrix} S & I_i & F \\ I_f & \tfrac{1}{2} & \lambda \end{Bmatrix}^2 \tag{8.4}$$

by considering the coupling of the angular momenta and summing over all projections (see Appendix D). The energy shift ΔE and the population $P(F)$ for $\lambda = 0$ and 1, and $S = \frac{1}{2}$ are listed in Table 12. The nonstatistical population for $\lambda = 1$ (and $S = \frac{1}{2}$) causes a nonzero energy shift. In electron capture this is the case for the allowed Gamow-Teller transitions and for some first forbidden transitions, as recognized and experimentally verified by Borchert *et al.*(47) In internal conversion, an analogous x-ray shift is expected, and has been observed in the M1 case(57) by Egorov *et al.*(57)

The calculated magnetic hyperfine shifts δ_{MS} are listed in Table 13. One has to remember that these calculated δ_{MS}'s have

TABLE 12. Population P(F) and energy shift ΔE of K x rays for nuclear transitions with $\lambda = 0$ and 1, and $S = \frac{1}{2}$.

λ	$\Delta I \equiv I_f - I_i$	Populations P(F) $F = I_f + \frac{1}{2}$	 $F = I_f - \frac{1}{2}$	Energy Shift ΔE
0	0	$\frac{I_f + 1}{2I_f + 1}$	$\frac{I_f}{2I_f + 1}$	0
1	0	$\frac{I_f}{2I_f + 1}$	$\frac{I_f + 1}{2I_f + 1}$	$-\frac{1}{2}A$
1	1	0	1	$-\frac{1}{2}A(I_f + 1)$
1	-1	1	0	$\frac{1}{2}A I_f$

TABLE 13. Calculated magnetic hyperfine shifts[a].

Source	Transition Mode and %	I_i	I_f	Relative Yield	μ^j (nm)	ΔE (eV)	Total Magnetic Hyperfine Shift[b] δ_{MS} (eV)
^{181}W	EC 100%	$9/2^+$	$7/2^+$	0.65	2.36	0.84	0.40
		$9/2^+$	$9/2^-$	0.35	5.28[c]	-0.42[d]	
^{181}Hf	IC 100%	$3/2^+$	$5/2^+$	0.05x0.5	3.25[e]	-1.59	0.13
		$5/2^+$	$7/2^+$	0.07x0.02	2.36	-1.06	
		$9/2^+$	$7/2^+$	0.24x0.86	2.36	0.84	
^{153}Gd	EC 68%	$3/2^-$	$5/2^+$	0.24	1.53	-0.42	-0.40
		$3/2^-$	$5/2^-$	0.30	3.2[f,g]	-0.87	
		$3/2^-$	$3/2^+$	0.32	2.0[f]	-0.26[d]	
		$3/2^-$	$5/2^+$	0.12	2.0	-0.55	
	IC 32%	$5/2^+$	$3/2^+$	0.21x0.98	2.0[f]	0.38	
		$3/2^+$	$5/2^+$	0.62x0.98	1.53	-0.41	
^{175}Hf	EC 86%	$5/2^-$	$5/2^+$	0.86	3.2[h]	-0.40[d]	-0.48
		$5/2^-$	$7/2^+$	0.14	3.1[h]	-1.26	
	IC 14%	$7/2^+$	$5/2^+$	0.42x0.97	3.2[h]	0.99	
		$5/2^+$	$7/2^+$	0.53x1	3.1[h]	-1.24	
^{182}Ta	IC 100%	4^-	3^-	0.05x0.11	2.0[i]	0.74	0.36
		4^-	3^-	0.11x0.96	2.0[i]	0.74	
		3^-	2^-	0.48x0.92	1.7[i]	0.63	

[a] Refer to Figs. 18-22.

[b] $\delta_{MS} = \sum_i (\Delta E)_i \, (\%)_i$, summed over all transitions.

For example, in ^{175}Hf

$$\delta_{MS} = -0.48 \text{ eV} = (-0.40 \times 0.86 - 1.26 \times 0.14) \times 0.86 + (0.99 \times 0.42 \times 0.97 - 1.24 \times 0.53) \times 0.14.$$

[c] Nucl. Data Sheets 9, 347 (1973).

[d] Pure λ = 1 assumed

[e] Nucl. Data Sheets 9, 351 (1973).

[f] Ref. 59.

[g] Based on Nilsson state assignment $5/2^-$ [532].

[h] Based on Nilsson state assignment $5/2^+$ [402].

[i] Ref. 58.

[j] μ's are in units of nuclear magneton.

sometimes an inherent uncertainty caused by the unknown relative role of $\lambda = 1$ and $\lambda = 0$ parts in $\Delta I = 0$ first forbidden electron capture. For internal conversion we calculated only the contribution of M1 transitions under the assumption that the population of the ejected electron in its final states of angular momenta $S = \lambda + \frac{1}{2}$ and $\lambda - \frac{1}{2}$ is statistical for E1 and E2 transitions (see Appendix D).

8.2 Other Known Contributions to the X-Ray Shift

Besides the magnetic hyperfine interaction, the following effects may also contribute to x-ray shifts:

a. Isotope and isomer shifts. The variation of nuclear charge distribution in different isotopes and isomers affects the 1s electronic state, shifting all K x rays by the same amount.(41,60) In the cases of Ta and Lu, we compared the K x rays emitted by identical isotopes. In Eu and W, however, the fluorescence data were obtained with the natural mixture of Eu isotopes and W isotopes, while the electron capture source contained only ^{153}Eu and the β^- decay source contained only ^{182}W. There are 52.2% ^{153}Eu and 47.8% ^{151}Eu in natural Eu.(50) The measured isotope shift of Eu K x rays is $\Delta E_{151-153} = 0.186$ eV.(61) So the energies of the K x rays emitted from a $EU_2O_3(f\ell)$ sample are shifted upwards by 0.09 eV, compared to those from a ^{153}Gd EC source by the isotope shift effect. Natural W contains 26.4% ^{182}W, 14.4% ^{183}W, 30.6% ^{184}W, and 28.4% ^{186}W.(50) The known isotope shifts of W K x rays are $\Delta E_{182-183} = 0.043$, $\Delta E_{182-184} = 0.092$, and $\Delta E_{182-186} = 0.152$ eV.(62-64) So the isotope shift contributes 0.08 eV to the measured ^{182}Ta - W$(f\ell)$

shift of W K x rays.

The known isomer shifts in Ta, Eu, and W are considerably smaller than the isotope shifts(60) and thus are not included in Table 14 in Sec. 8.3.

b. Chemical shift. The K x-ray energy is known to depend on the configuration of the outer atomic electrons.(41) There is an energy shift between x rays emitted from an element in different chemical compounds. When comparing an electron capture (element Z + 1) source with a fluorescence source (element Z) one often encounters a similar effect, because a K x ray is emitted after each K capture before the outer electron shell rearrangement takes place.(34,49) Among the sources we studied, a noticeable effect of this type is expected only for Eu. We assume that the Gd_3O_2 has a valence electron configuration similar to the two-valent Eu (Eu metal). The electron-capture related Eu K x rays emitted from the $^{153}Gd_3O_2$ source are, therefore, shifted with respect to the K x ray of the three valent Eu in Eu_2O_3 by the "equivalent chemical shift". The Eu K x rays accompanying internal conversion, however, are emitted after the Eu atom has returned to its normal three-valent oxide state, and thus do not have the chemical shift. Since 68% of the K x rays emitted from $^{153}Gd_3O_2$ are immediately related to electron capture, one can use $0.68(E_{\mathrm{Eu\ metal}} - E_{Eu_2O_3})$ as the chemical shift correction for the $^{153}Gd_2O_3$ source. The experimentally measured Eu x-ray chemical shifts of Smirnov *et al.* (see Table 11) are used in Table 14.

c. Shake-off effect. As an electronic 1s vacancy is created the atomic potential changes suddenly, causing partial ionization of the atom. The degree of ionization of the individual electron shells was calculated by Carlson *et al.*(65) Generally one expects a larger shake-off effect when electron vacancies are produced by fluorescence or by internal conversion than by electron capture. The atom will remain partially ionized when K x rays are emitted (in $\sim 10^{-17}$ sec). The contribution of this effect is estimated to be less than 0.1 eV for the cases we studied.(48,49)

8.3 Conclusion

The obversed shifts and the theoretically expected shifts described above are listed in Table 14 for ten different measurements. The corrected shift E_{corr} is calculated by subtracting the listed contributions from the observed shift, and plotted in Fig. 27. It shows that the above-enumerated effects are able to explain most of the observed shift in Eu, Lu, and W. However, a surprisingly large shift remains in Ta. Recently, Borchert *et al.*(74) have confirmed experimentally this shift in Ta.

In conclusion, as a result of the present work and that of Refs. 47-49 and 57, several mechanisms of x-ray shifts have been identified. Therefore, in formulating new x-ray standards it is important to give due consideration to the mode of production. The large shift in Ta is not understood and further experimental and theoretical work is needed.

TABLE 14. Contributions to the measured shifts (in eV).

			Observed Shift	Magnetic Hyperfine Shift	Isotope Shift	Chemical Shift	Corrected Shift
No	Line	Sources	ΔE_{obs}	δ_{MS}	δ_{IS}	δ_{CS}	ΔE_{corr}[a]
(1)	Ta $K\alpha_1$	$^{181}WO_3$-Ta_2O_5	-0.77(0.05)	0.40	0	0	-1.17(0.05)
(2)		^{181}W - Ta	-0.81(0.08)	0.40	0	0	-1.21(0.08)
(3)		$^{181}HfO_2$-Ta_2O_5	0.70(0.11)	0.13	0	0	0.57(0.11)
(4)	Eu $K\alpha_1$	$^{153}Gd_2O_3$-Eu_2O_3	0.09(0.05)	-0.40	-0.09	0.44(0.01)	0.14(0.05)
(5)	$K\alpha_2$		0.11(0.06)	-0.40	-0.09	0.40(0.01)	0.20(0.06)
(6)	$K\beta_1$		0.60(0.06)	-0.40	-0.09	0.99(0.03)	0.10(0.07)
(7)	$K\beta_3$		0.89(0.10)	-0.40	-0.09	1.18(0.03)	0.20(0.11)
(8)	Lu $K\alpha_1$	$^{175}HfO_2$-Lu_2O_3	-0.43(0.10)	-0.48	0	0	0.05(0.10)
(9)	W $K\alpha_1$	$^{182}Ta_2O_5$-WO_3	0.31(0.08)	0.36	0.08		-0.13(0.08)
(10)		^{182}Ta-W	0.58(0.17)	0.36	0.08		0.14(0.17)

[a] $\Delta E_{corr} = \Delta E_{obs} - \delta_{MS} - \delta_{IS} - \delta_{CS}$. It contains the contributions of the shake-off effect, the isomer shift, and "other" effects.

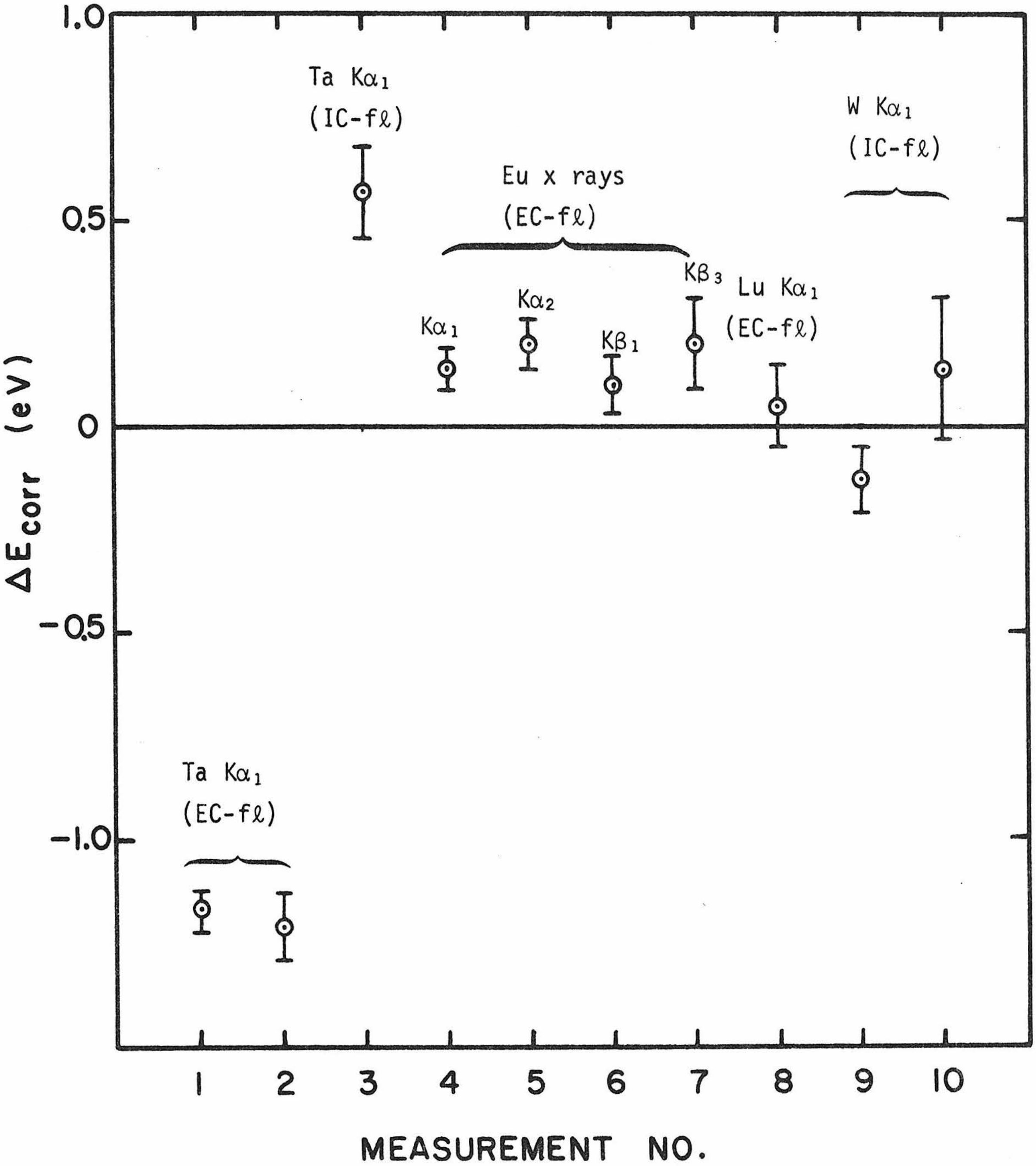

FIG. 27. Corrected shifts for different measurements (see Table 14).

8.4 Further Experimental Work

A possible origin of the unexpected Ta x-ray shift is the solid state effect. The Ta atom from ^{181}W EC (or ^{181}Hf β-decay) is in the W (or Hf) lattice, whereas the Ta atom in the fluorescence target is in the Ta lattice. The difference in solid state structure may cause an energy shift of x rays, as observed by Shaburov *et al.*(66,67) for Ce and Sm K x rays. In order to check this possibility we are measuring the energy shifts of Ta $K\alpha_1$ x rays between Ta metal, WTa and HfTa alloys containing small amounts of Ta. The dilute alloy should to a certain degree simulate the situation encountered in the EC or IC source, where the Ta atom emitting x rays is in the W or Hf lattice. Ta (2%) and W (98%) were arc-melted together and left in a liquid phase for about five minutes. The same process was repeated three times. The WTa alloy was then cooled down to the temperature of liquid nitrogen. The alloy became brittle at that temperature and was broken into powder. The HfTa alloy (with 2.5% Ta) was made by rf welding and ground into powder. The alloy targets were made of these powders. The Ta K x rays from four targets irradiated by a high-flux x-ray tube were compared. The four targets, 3.4 cm in diameter, are Ta foil (0.22 g/cm^2), Ta powder (0.29 g/cm^2), WTa alloy (0.32 g/cm^2), and HfTa alloy (0.20 g/cm^2). The preliminary results are shown in Fig. 28. The first measurement is a null test. The dotted points are the corresponding ΔE_{corr}'s, given in Table 14. It is unlikely that these results will fully explain the large shift in Ta. However, a non-zero shift between the WTa alloy and Ta metal has been observed. We plan to continue this

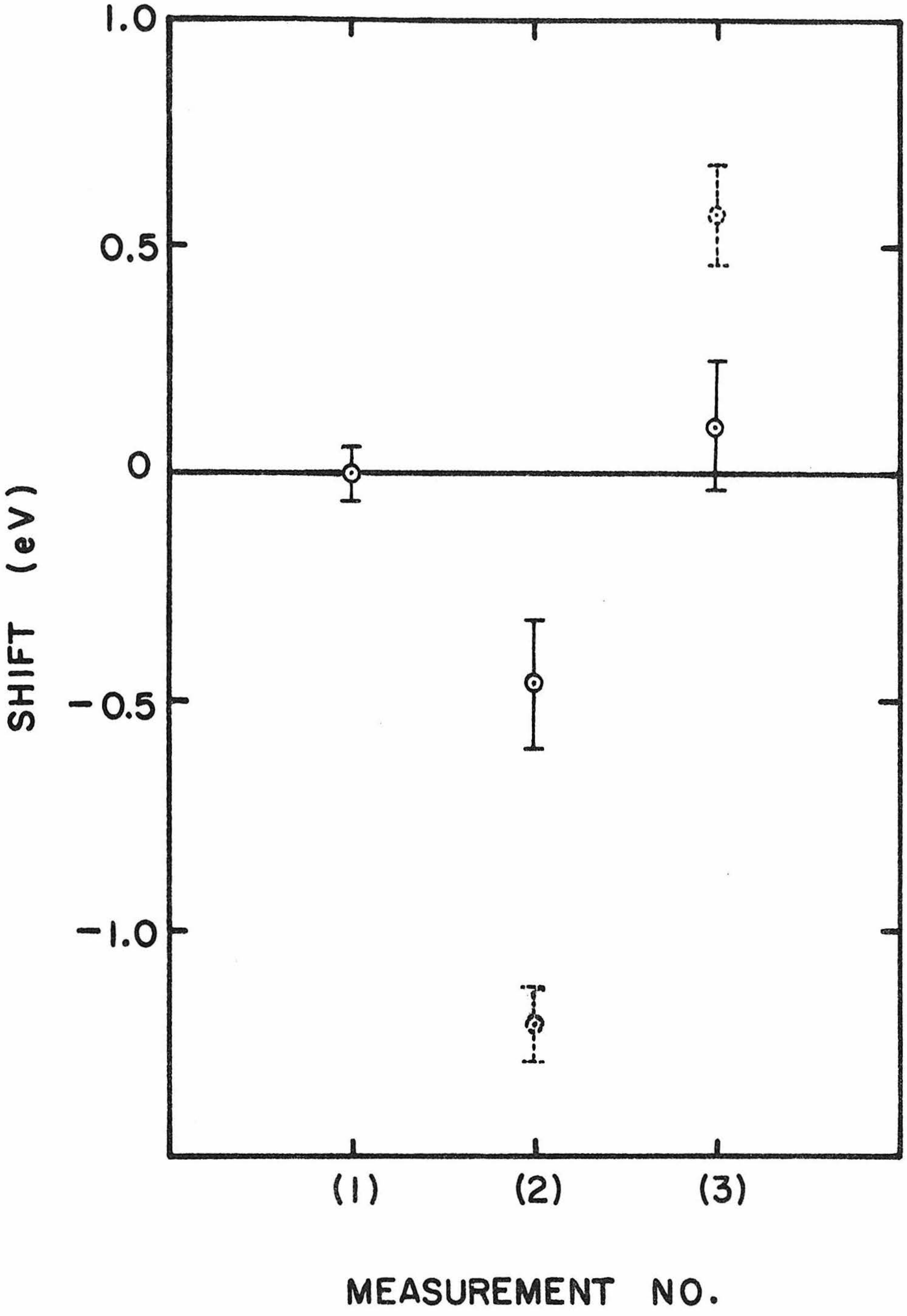

FIG. 28. Results of the alloy measurement: (1) ΔE(Ta foil -Ta powder) = 0.00(0.06) eV, (2) ΔE(WTa alloy-Ta powder) = -0.46 (0.14) eV, and (3) ΔE(HfTa alloy-Ta powder) = 0.11(0.14) eV. Dotted points indicate the corresponding ΔE_{corr}'s from Fig. 27.

experiment with alloys containing different concentrations of Ta, and hope that the new results will shed light on the origin of the so far unexplained shift in the Ta K x rays.

APPENDIX A

HARTMANN TEST OF THE CRYSTAL CURVATURE

The Hartmann test$^{(25)}$ is designed to test the curvature of the crystal. The centroids of γ-ray peaks diffracted by different portions of the crystal are measured. Owing to the imperfection of the bending of the crystal these centroids differ by small amounts. By illustrating this aberration in a Hartmann diagram, we can determine the best focal position and the width of the aberration pattern at that position.

In our test the 63 keV γ rays from a 1.5 Ci ^{169}Yb source were used. The circular source, 1 cm in diameter, was put at 46 cm behind the crystal. Distance between the crystal and the slit was 198.5 cm. The slit width was 0.10 mm. 10 portions in the crystal aperture were chosen, as indicated in the up-right corner of Fig. A.1. Each portion had a size 0.4 x 3 cm^2. The measured centroids of the 63 keV γ-ray peaks are listed in Table A.1, and so are the relative shifts. The results are illustrated in Fig. A.1. We found that the width of the aberration pattern at best focus was 0.12 mm, if we neglected the portion 5 which was apparently bad. The best focal position was found to be 1.9 cm from the slit position. Therefore, the optimum crystal to slit distance for the 63 keV γ rays is $198.5 + 1.9 = 200.4$ cm and the bending radius of the crystal is $\frac{200.4}{\cos\theta} = 201.1$ cm, where θ $(= 4.8^0)$ is the Bragg angle.

TABLE A.1 Centroids and their relative shifts in the Hartmann test.[a]

Crystal Portion	Centroid c_i (S.D.)	Centroid Shifts d_i[b] (S.D.)
1	195.28	0.28
2	195.06	0.06
3	195.00	0
4	194.88	-0.12
5	194.51	-0.49
6	195.38	0.30
7	195.25	0.17
8	195.08	0
9	194.88	-0.20
10	194.86	-0.22

[a] Errors of measured centroids were about 0.01 S.D.

S.D. represents Screw Division of the Sine Screw(30,31) of our spectrometer. 1 S.D. ≅ 1 mÅ in wavelength units.

[b] For $i = 1$ to 5, $d_i = c_i - c_3$.

For $i = 6$ to 10, $d_i = c_i - c_8$.

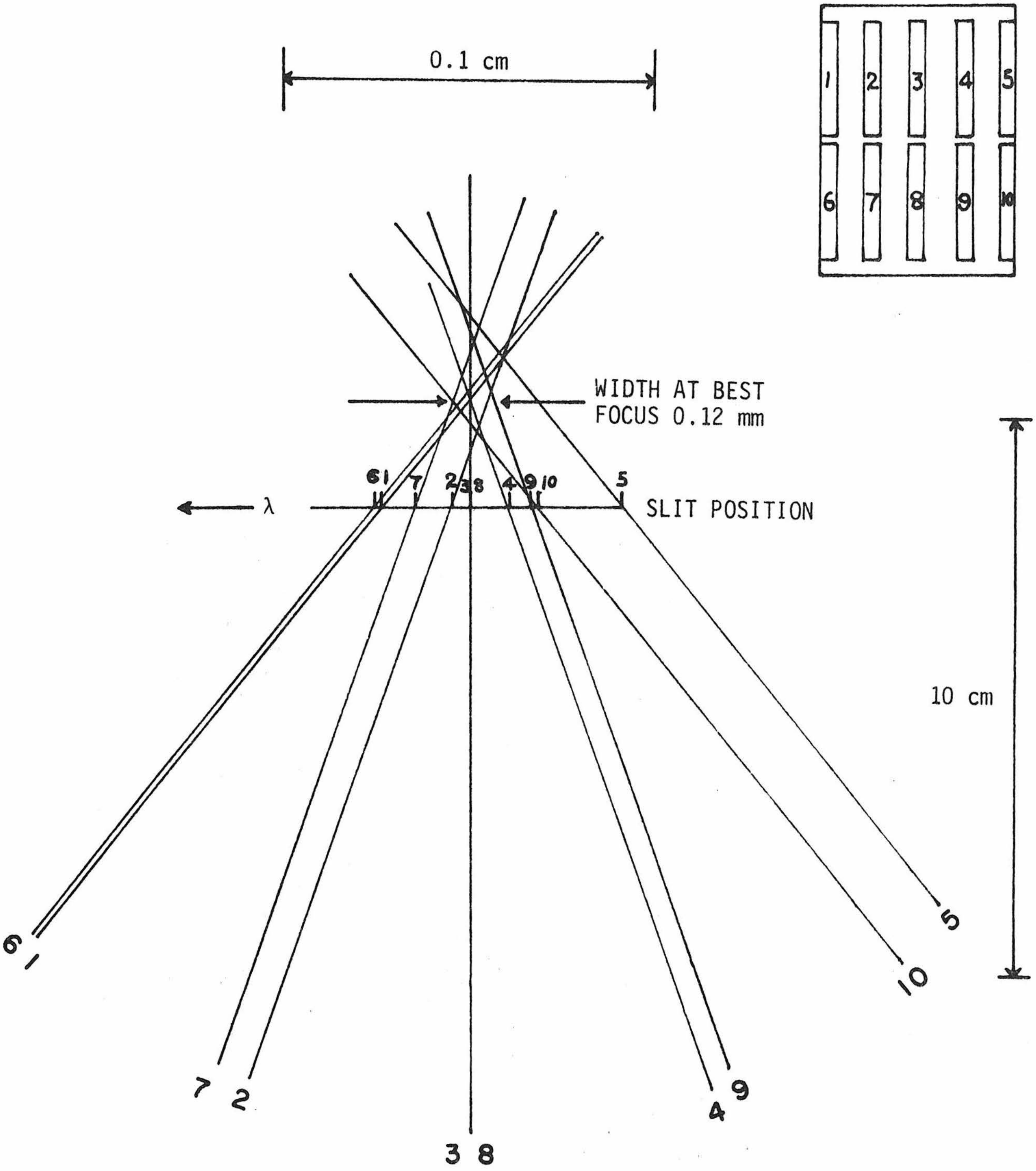

FIG. A.1. Hartmann test of the quartz(310) crystal. The horizontal scale of this diagram is 150 times the vertical scale. The ten numbered positions in the crystal aperture, looking to the slit, are indicated in the up-right corner.

APPENDIX B

CENTROID ERROR IN THE PRESENCE OF A LARGE BACKGROUND[†]

To determine the error in the centroid of a Gaussian for the specific case of a high background rate, computer generated random data were used to simulate a spectrum where N = total number of counts under the Gaussian excluding background was varied between 200 and 5000 and R = background to peak ratio was varied from 0 to 10. The centroid errors (σ_c) were then computed by a standard least-squares fitting program. The results of these fits are plotted in Fig. B.1 in a dimensionless representation. Γ is the full-width-half-maximum of the Gaussian. For a large R ($\gtrsim 0.5$), the working empirical formula is

$$\frac{\sigma_c}{\Gamma} = 0.7160 \sqrt{\frac{R+\frac{1}{2}}{N}} \; . \qquad \text{(B.1)}$$

For a small R the relation rapidly approaches the analytically determined R = 0 (no background) case

$$\frac{\sigma_c}{\Gamma} = 0.6006 \sqrt{\frac{1}{2N}} \; . \qquad \text{(B.2)}$$

Note that Eq. (B.1) overestimates σ_c by only 20% for $R \cong 0$.

[†] The present study was carried out by Stephen Kellogg.

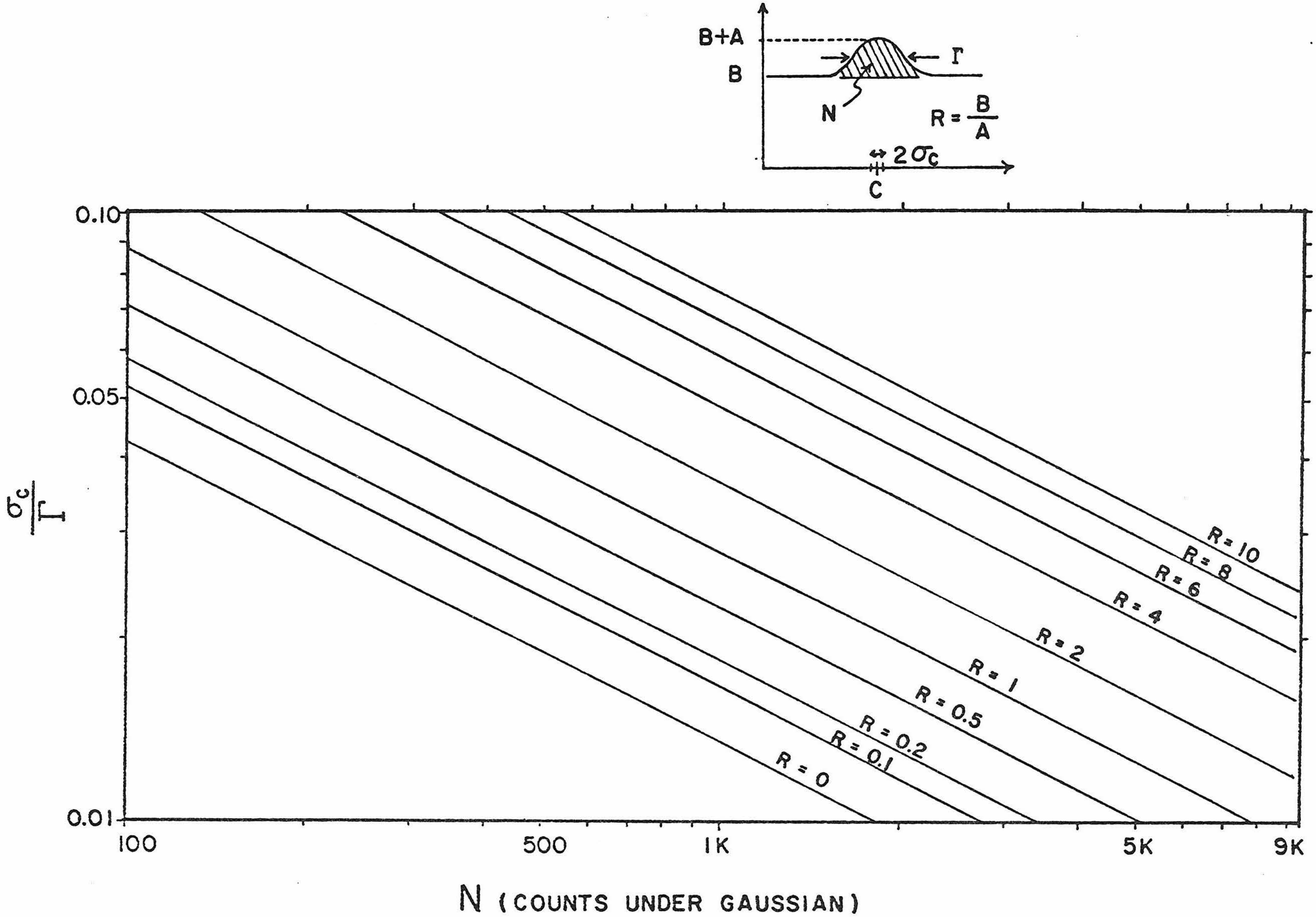

FIG. B.1. Empirically derived σ_c/Γ as a function of N for constant R.

APPENDIX C

DARWIN TERM OF THE KLEIN-GORDON EQUATION

In general, the Klein-Gordon (KG) equation for a boson in an electromagnetic potential $(\vec{A}, \phi)$

$$(i\frac{\partial}{\partial t} - e\phi)^2 \psi = (-i\vec{\nabla} - e\vec{A})^2 \psi + m^2 \psi \tag{C.1}$$

can be re-written in the two-component language$^{(68)}$ as

$$i\frac{\partial\Phi(x)}{\partial t} = \left[\eta(m + \frac{\vec{\pi}^2}{2m}) + \rho\,\frac{\vec{\pi}^2}{2m} + e\phi\right]\Phi(x) \tag{C.2}$$

$$= H\Phi \equiv \eta m + \varepsilon + \mathcal{O}$$

where $\eta = \begin{pmatrix}1 & 0\\ 0 & -1\end{pmatrix}$, $\rho = \begin{pmatrix}0 & 1\\ -1 & 0\end{pmatrix}$, $\vec{\pi} = -i\vec{\nabla} - e\vec{A}$,

$$\Phi = \frac{1}{2}\begin{pmatrix}\psi + \frac{i}{m}\dot{\psi}\\ \psi - \frac{i}{m}\dot{\psi}\end{pmatrix},\ \varepsilon = \eta\frac{\vec{\pi}^2}{2m} + e\phi\ ,\ \text{and}\ \mathcal{O} = \rho\frac{\vec{\pi}^2}{2m}\ .$$

ε is an even operator that does not couple the two components of Φ. $\mathcal{O}$ is an odd operator that couples the two components. By performing the Foldy-Wouthuysen transformation$^{(69)}$

$$\begin{aligned}\Phi' &= e^{iS}\,\Phi\\ H' &= e^{iS}\,H\,e^{-iS}\end{aligned} \tag{C.3}$$

with $s = -\frac{i}{2m}\eta\mathcal{O}$, the odd term $\mathcal{O}'$ in H' becomes smaller than $\mathcal{O}$ by order of $\frac{1}{m}$. Applying the Foldy-Wouthuysen transformation three times to Eq. (C.2) it turned out that, to order $(\frac{Z\alpha}{n})^6$, the Klein-Gordon equation (C.2) becomes

$$i\,\frac{\partial\Phi'''}{\partial t} = H'''\,\Phi'''$$

with

$$H''' = \eta\left(m + \frac{\vec{\pi}^{\,2}}{2m} - \frac{\vec{\pi}^{\,4}}{8m^3} + \frac{\vec{\pi}^{\,6}}{16m^5}\right) + e\phi + \frac{1}{32m^4}\left[\vec{\pi}^{\,2}, \left[\vec{\pi}^{\,2}, e\phi\right]\right] . \qquad \text{(C.4)}$$

The first term of Eq. (C.4) is the expansion of the Hamiltonian of the Relativistic Schrödinger (RS) equation. The double commutator term, called the Darwin term, accounts for the difference of the KG and RS equations.

For a spinless particle in a Coulomb field, we have $\vec{A} = 0$ and $\vec{\pi} = \vec{p}$. Therefore, to order $(\frac{Z\alpha}{n})^6$, the difference in energy level predicted by the two equations is

$$\begin{aligned}\Delta_{n\ell} &\equiv (E_{n\ell})_{KG} - (E_{n\ell})_{RS} \\ &= \left\langle \psi^0_{n\ell} \right| \frac{1}{32m^4}\left[\vec{P}^{\,2}, \left[\vec{P}^{\,2}, e\phi\right]\right] \left| \psi^0_{n\ell} \right\rangle , \qquad \text{(C.5)}\end{aligned}$$

where $\psi^0_{n\ell}$ is the eigenstate of non-relativistic Schrödinger equation (2.2).

Let us evaluate the expectation value in (C.5). For simplicity we will use $< O > \equiv < \psi^0_{n\ell} | O | \psi^0_{n\ell} >$ and $V \equiv e\phi = -\frac{Z\alpha}{r}$. From

$$\frac{\vec{p}^{\,2}}{2m} | \psi^0_{n\ell} > = (E^0_{n\ell} - V) | \psi^0_{n\ell} >$$

and its conjugate we can simplify Eq. (C.5) to

$$\Delta_{n\ell} = \frac{1}{16m^3} \left\{ \left\langle (E^0_{n\ell} - V) \left[\vec{P}^{\,2}, V \right] \right\rangle - \left\langle \left[\vec{P}, V \right] (E^0_{n\ell} - V) \right\rangle \right\}$$

$$= -\frac{1}{8m^3} \left\langle V \left[\vec{P}^2, V \right] \right\rangle$$

$$= \frac{(Z\alpha)^2}{8m^3} \left\langle \frac{1}{r} \left[\vec{\nabla}^2, \frac{1}{r} \right] \right\rangle . \qquad (C.6)$$

Since $\left[\vec{\nabla}^2, \frac{1}{r} \right] = -\frac{2}{r^2} \frac{\partial}{\partial r}$ (for $r \neq 0$), Eq. (C.6) becomes

$$\Delta_{n\ell} = -\frac{(Z\alpha)^2}{4m^3} \left\langle \frac{1}{r^3} \frac{\partial}{\partial r} \right\rangle . \qquad (C.7)$$

It can be shown that, for $\ell \neq 0$

$$\left\langle \frac{1}{r^3} \frac{\partial}{\partial r} \right\rangle = \frac{1}{2} \left\langle \frac{1}{r^4} \right\rangle , \qquad (C.8)$$

and(70)

$$\langle \frac{1}{r^4} \rangle = \frac{(mZ\alpha)^4 \, (3n^2 - \ell(\ell + 1))}{2n^5 \, (\ell + 3/2)(\ell + 1)(\ell + 1/2) \, \ell(\ell - 1/2)} \; . \qquad (C.9)$$

Therefore, by Eqs. (C.6)-(C.9)

$$\Delta_{n\ell} = - \frac{m}{16} \left(\frac{Z\alpha}{n}\right)^6 \frac{3n^3 - n\ell(\ell + 1)}{(\ell + 3/2)(\ell + 1)(\ell + 1/2)\,\ell\,(\ell - 1/2)} \qquad (C.10)$$

for $\ell \neq 0$.

APPENDIX D

POPULATION OF THE MAGNETIC HYPERFINE COMPONENTS

The nuclear transition (electron capture or internal conversion) under consideration has an initial state

$$|i> = |I_i\, m_i>\, |(1s)^2_0>$$

and a final state

$$|f> = |I_f\, m_f>\, |S_e\, m_e>\, |S\, m_s> ,$$

where $|I_i\, m_i>$, $|I_f\, m_f>$ are the nuclear states, $|(1s)^2_0>$ denotes the two-1s-electron system that has an angular momentum 0, $|S_e\, m_e>$ is the remaining 1s electron state with $S_e = \frac{1}{2}$, and $|S\, m_s>$ denotes the outgoing neutrino (electron capture case) or electron (internal conversion case) state. $|I_f\, m_f>$ and $|S_e\, m_e>$ are coupled to from the final state $|F\, m_F>$. We would like to find the probability that the hyperfine component with $F = I_f + \frac{1}{2}$ or $F = I_f - \frac{1}{2}$ is populated.

Let $T_{\lambda m_\lambda}$ be the nuclear transition operator having a multipolarity λ. By the conservation of angular momentum, we get the following relations:

$$\begin{aligned} \vec{I}_f &= \vec{I}_i + \vec{\lambda} \\ \vec{\lambda} &= -\vec{S}_e - \vec{S} \qquad\qquad (D.1) \\ \vec{I}_i &= \vec{F} + \vec{S} = \vec{I}_f + (-\vec{\lambda}). \end{aligned}$$

The symbolic representation of the coupling of the angular momenta is shown in Fig. D.1.

The amplitude of the transition $|I_i m_i (1s)^2_0\rangle \to |F m_F\rangle |S m_s\rangle$ is

$$A = \sum_{m_f m_e} \langle I_f m_f | T_{\lambda m_\lambda} | I_i m_i \rangle \cdot \langle S S_e m_s m_e | T^{*}_{\lambda m_\lambda} | (1s)^2_0 \rangle \langle I_f S_e m_f m_e | F m_F \rangle . \qquad (D.2)$$

By the Wigner-Eckart theorem(71) and the definition of the inner product of tensors(72) we get

$$A = \langle \| \, \| \rangle \sum_{m_\lambda m_f m_e} (-1)^{m_\lambda} \langle I_i \lambda m_i m_\lambda | I_f m_f \rangle \langle S \tfrac{1}{2} m_s m_e | \lambda - m_\lambda \rangle$$

$$\langle I_f \tfrac{1}{2} m_f m_e | F m_F \rangle , \qquad (D.3)$$

where $\langle \| \, \| \rangle$ denotes the reduced matrix term which is independent of F and the m's. Using the contraction of three Clebsch-Gordan coefficients(73) and the coupling of angular momenta given in (D.1), one can show that

$$A = \langle \| \, \| \rangle (-1)^{-1-\lambda+3S+2I_i+F-m_s-m_F} \frac{\sqrt{2I_f+1}}{\sqrt{2I_i+1}} \sqrt{2\lambda+1} \sqrt{2F+1}$$

$$\langle F S m_F m_s | I_i m_i \rangle \begin{Bmatrix} S & I_i & F \\ I_f & \tfrac{1}{2} & \lambda \end{Bmatrix} . \qquad (D.4)$$

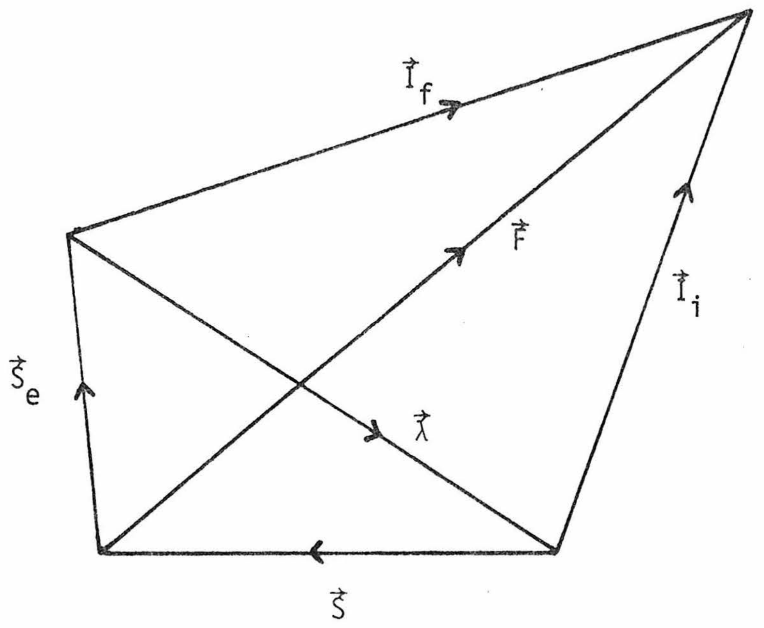

FIG. D.1. Symbolic representation of the coupling of the angular momenta.

Since the final states with different m_F (or m_s) are orthogonal to each other, we sum the squares of A over m_F (or m_s) to get the total transition rate. With the help of

$$\sum_{m_F \text{ (or } m_s)} |\langle F\, S\, m_F\, m_s\, | I_i\, m_i \rangle|^2 = 1$$

and the normalization of

$$\sum_F P(F) = 1,$$

one can get

$$P(F) = (2\lambda + 1)\,(2F + 1) \begin{Bmatrix} S & I_i & F \\ I_f & \frac{1}{2} & \lambda \end{Bmatrix}^2 . \qquad (D.5)$$

Furthermore, if the population of the outgoing fermion in its final state of angular momenta $S = \lambda + \frac{1}{2}$ and $\lambda - \frac{1}{2}$ is statistical, i.e. proportional to $2S+1$, then the shift given by Eq. (8.3) is

$$\Delta E = \frac{1}{2(\lambda+\frac{1}{2})+1+2(\lambda-\frac{1}{2})+1} \sum_S (2S+1)\,\frac{A}{2}\Bigg[I_f(2\lambda+1)\;(2I_f+2) \begin{Bmatrix} S & I_i & I_f+\frac{1}{2} \\ I_f & \frac{1}{2} & \lambda \end{Bmatrix}^2$$

$$- (I_f+1)\;(2\lambda+1)\;(2I_f) \begin{Bmatrix} S & I_i & I_f-\frac{1}{2} \\ I_f & \frac{1}{2} & \lambda \end{Bmatrix}^2 \Bigg]$$

$$= \frac{A}{4\lambda+2}(2\lambda+1)\, I_f(I_f+1) \sum_S (2S+1) \left[\begin{Bmatrix} S & I_i & I_f+\frac{1}{2} \\ I_f & \frac{1}{2} & \lambda \end{Bmatrix}^2 - \begin{Bmatrix} S & I_i & I_f-\frac{1}{2} \\ I_f & \frac{1}{2} & \lambda \end{Bmatrix}^2 \right]$$

$$= \frac{A}{4\lambda+2}(2\lambda+1)\; I_f\; (I_f+1) \left[\frac{1}{2I_f+1} - \frac{1}{2I_f+1} \right]$$

$$= 0.$$

Here we have used the relation

$$\sum_k (2k+1)\,(2h+1) \begin{Bmatrix} k & a & b \\ h & c & d \end{Bmatrix} \begin{Bmatrix} k & a & b \\ g & c & d \end{Bmatrix} = \delta_{hg} \, .$$

REFERENCES

1. R. S. Van Dyck, Jr., P. B. Schwinberg, and H. G. Dehmelt, Phys. Rev. Lett. 38, 310 (1977).
2. M. L. Goldberger and K. M. Watson, Collision Theory (John Wiley & Sons, New York, 1964), p. 24.
3. A. S. Davydov, Quantum Mechanics, 1st ed. (Pergamon, Oxford, 1965), pp. 208 ff.
4. R. M. Eisberg, Fundamentals of Modern Physics (John Wiley & Sons, New York, 1961), p. 354.
5. G. Backenstoss, Ann. Rev. Nucl. Sci. 20, 467 (1970).
6. J. Hüfner, Phys. Report 21C, (1975).
7. A. L. Carter, M. S. Dixit, M. K. Sundaresen, J. S. Wadden, F. J. S. Watson, C. K. Hargrove, E. P. Hincks, R. J. McKee, H. Mes, H. L. Anderson and A. Zehnder, Phys. Rev. Lett. 37, 1380 (1976).
8. H. E. Henrikson and F. Boehm, Nucl. Instr. Meth. 121, 269 (1974).
9. L. I. Schiff, Quantum Mechanics, 3rd. ed. (McGraw-Hill, New York, 1968), p. 92.
10. R. C. Barrett, S. I. Brodsky, G. W. Erickson, and M. H. Goldhaber, Phys. Rev. 166, 1589 (1968).
11. R. J. McKee, Phys. Rev. 180, 1139 (1969).
12. P. Vogel, At. Data and Nucl. Data Tables 14, 599 (1974).
13. M. Ericson and T. E. O. Ericson, Annals of Phys. 36, 323 (1966).
14. M. Krell and T. E. O. Ericson, Nucl. Phys. B11, 521 (1969).
15. D. K. Anderson, D. A. Jenkins, and R. J. Powers, Phys. Rev. 188, 9 (1969); Phys. Rev. Lett. 24, 71 (1970).
16. R. J. Powers, to be published.
17. B. Fricke, Nuovo Cimento Lett. 2, 859 (1969).
18. P. Vogel, Phys. Rev. A 7, 63 (1973).
19. D. Lu, L. Delker, G. Dugan, C. S. Wu, A. Caffrey, T. Cheng, and Y. K. Lee, Bull. Am. Phys. Soc. 23, 928 (1978).

20. P. Vogel, Caltech Internal Report CALT-63-320, (unpublished).

21. R. Seki, Phys. Lett. 58B, 49 (1975).

22. R. J. Powers, P. Martin, G. H. Miller, R. E. Welsh, and D. A. Jenkins, Nucl. Phys. A230, 413 (1974).

23. F. Boehm, R. J. Powers, J.-L. Vuilleumier, K.-C. Wang, A. R. Kunselman, P. Thompson, and J. Thomas, Progress Report to LAMPF, Exp. 173, CALT-63-294, 1977.

24. Made by the Superior Electric Co., Bristol, Connecticut.

25. J. W. M. DuMond, Special Technical Report No. 8, Atomic Energy Commission, Contract No. AT (04-3)-8, March 1954, pp. 35 ff.

26. J. D. H. Donnay, H. M. Ondik, Crystal Data Determinative Tables, 3rd. ed., Vol. 2, published by U.S. Department of Commerce, National Bureau of Standards, and Joint Committee on Powder Diffraction Standards, 1972, p. H-121.

27. O. I. Sumbaev, Sov. Phys. JETP 27, 724 (1968).

28. Hyccups-M User Mannual, revised ed. (1974), Tennecomp Systems Inc., Oak Ridge, Tennessee.

29. A. Zehnder, Caltech Internal Report, CALT-63-237 and CALT-63-237a, (unpublished).

30. J. W. M. DuMond, Rev. Sci. Instr. 9, 329 (1938)

31. E. J. Seppi, H. Henrikson, F. Boehm, and J. W. M. DuMond, Nucl. Instr. Meth. 16, 17 (1962).

32. J. A. Bearden, Rev. Mod. Phys. 39, 78 (1967); E. R. Cohen, At. Data Nucl. Data Tables 18, 587 (1976).

33. P. L. Lee, Nucl. Instr. Meth. 144, 363 (1977).

34. K.-C. Wang, A. A. Hahn, and F. Boehm, Phys. Rev. A 17, 1735 (1978).

35. S. Kellogg, Appendix to Progress Report to LAMPF Exp. 173, CALT-63-294, 1977.

36. Particle Data Group LBL, Phys. Lett. 75B, 17 (1978).

37. W. E. Lamb, Jr., and R. C. Retherford, Phys. Rev. 72, 241 (1957).

38. K. E. Kiryanov, V. I. Maruskenko, A. F. Mezentsev, A. A. Petrunin, S. G. Skornyakov, and A. I. Smirnov, Sov. J. Nucl. Phys. 26(6), 685 (1977).

39. C. J. Batty, S. F. Biagi, E. Friedman, S. D. Hoath, J. D. Davies, G. J. Pyle, and G. T. A. Squier, Phys. Rev. Lett. 40, 931 (1978).

40. R. J. Powers, A. A. Hahn, K.-C. Wang, M. V. Hoelm, E. B. Shera, H. D. Wohlfahrt, Y. Yamazaki, and A. R. Kunselman, contributed paper, 1979 Annual Meeting APS, New York, Bull. Am. Phys. Soc. 24, 32 (1979).

41. F. Boehm, in Atomic Inner Shell Processes, edited by B. Crasemann (Academic, New York, 1975), pp. 411-441.

42. A. A. Hahn, K.-C. Wang, F. Boehm, H. E. Henrikson, and P. Vogel, Phys. Rev. Lett. 37, 1741 (1976).

43. A. A. Hahn, K.-C. Wang, F. Boehm, H. E. Henrikson, and P. Vogel, Phys. Rev. A 16, 1317 (1977).

44. K.-C. Wang, A. A. Hahn, F. Boehm, and P. Vogel, Phys. Rev. A 18, 2580 (1978).

45. W. Beer and J. Kern, Phys. Lett. 47B, 345 (1973).

46. G. L. Borchert, Contribution to the International Conference on Atomic Physics, Heidelberg, 1974 (unpublished).

47. G. L. Borchert, P. G. Hansen, B. Jonson, H. L. Ravn, O. W. B. Schult, and P. Tideman-Petersson and the ISOLDE Collaboration, Phys. Lett. A 63, 15 (1977).

48. G. L. Borchert, P. G. Hansen, J. Jonson, I. Lindgren, H. L. Ravn, O. W. B. Schult, and P. Tideman-Petersson, and the ISOLDE Collaboration, Phys. Lett. A 65, 297 (1978).

49. G. L. Borchert, P. G. Hansen, B. Jonson, I. Lindgren, H. L. Ravn, O. W. B. Schult, and P. Tideman-Petersson, and the ISOLDE Collaboration, Phys. Lett. A 66, 374 (1978).

50. C. M. Lederer, J. M. Hollander, and I. Perlman, Tables of Isotopes, 6th ed. (John Wiley & Sons, New York, 1967).

51. P. Boyer, P. Chedin, and J. Oms, Nucl. Phys. A 99, 213 (1967)

52. O. I. Sumbaev, E. V. Petrovich, Y. P. Smirnov, A. I. Egorov, V. S. Zykov, and A. I. Grushko, Sov. Phys. JETP 26, 891 (1968).

53. Y. P. Smirnov, O. I. Sumbaev, E. V. Petrovich, V. S. Zykov, A. I. Egorov, A. I. Grushko, Sov. Phys. JETP 30, 622 (1970).

54. M. S. Freedman and F. T. Porter, Phys. Rev. A 6, 659 (1972).

55. G. Breit, Phys. Rev. 35, 1447 (1930).

56. A. S. Rylnikov, A. I. Egorov, G. A. Ivanov, V. I. Marushenko, A. F. Mezentsev, A. I. Smirnov, O. I. Sumbaev, and V. V. Fedorov, Sov. Phys. JETP 36, 27 (1973).

57. A. I. Egorov, A. A. Rodionov, A. S. Rylnikov, A. E. Sovestnoe, O. I. Sumbaev, and V. A. Shaburov, JETP Lett. 27(9), 483 (1978).

58. T. See and T. Hayashi, Proceedings of International Conference on Nuclear Moments and Nuclear Structure, Osaka, Japan, September 4-8, 1972, edited by H. Horie and K. Sugimoto, p. 432.

59. G. H. Fuller, Office of Standard Reference Data, and V. W. Cohen, Nucl. Data Tables 5, 433 (1969).

60. G. M. Kalvins and G. K. Shenoy, At. Data Nucl. Data Tables, 14, 639 (1974).

61. A. S. Rylnikov, A. I. Egorov, G. A. Ivanov, V. I. Marushenko, A. F. Mezentsev, A. I. Smirnov, O. I. Sumbaev, and V. V. Fyodorov, Sov. Phys. JETP 36, 27 (1973).

62. F. Boehm and P. L. Lee, At. Data Nucl. Data Tables 14, 605 (1974).

63. K. Heilig and A. Steudel, At. Data Nucl. Data Tables 14, 613 (1974).

64. R. B. Chesler and F. Boehm, Phys. Rev. 166, 1202 (1968).

65. T. A. Carlson, C. W. Nestor, Jr., T. C. Tucker, and F. B. Malik, Phys. Rev. 169, 27 (1968).

66. V. A. Shaburov, I. M. Band, A. I. Grushko, T. B. Mezentseva, E. V. Petrovich, Yu. P. Smirnov, A. E. Sovestnov, O. I. Sumbaev, M. B. Trzhaskovskaya, and I. A. Markova, Sov. Phys. JETP 38, 573 (1974).

67. V. A. Shaburov, A. I. Egorov, G. A. Krutov, A. S. Rylnikov, A. I. Sovestnov, and O. I. Sumbaev, Sov. Phys. JETP 41, 158 (1975).

68. J. D. Bjorken and S. D. Drell, Relativistic Quantum Mechanics (McGraw-Hill, New York, 1964), pp. 202 ff.

69. L. L. Foldy and S. A. Wouthuysen, Phys. Rev. 78, 29 (1950).

70. H. A. Bethe and E. E. Salpeter, Quantum Mechanics of One and Two Electron Atoms (Academic, New York, 1957), p. 33.

71. C. Eckart, Rev. Mod. Phys. *2*, 305 (1930); E. P. Wigner, *Group Theory* (Academic, New York, 1959), p. 245.

72. D. M. Brink and G. R. Satchler, *Angular Momentum*, 2nd. ed. (Clarendon, Oxford, 1968), p. 52.

73. Ibid., p. 42.

74. G. L. Borchert, private communication.